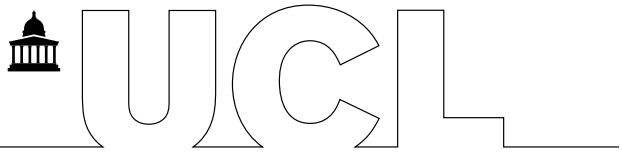

Coherent Effects in Dispersive Quantum Dynamics

Sai-Yun Ye

A thesis submitted to

University College London

for the degree of

Doctor of Philosophy

Department of Physics and Astronomy

University College London

May 2, 2012

Declaration

I, Sai-Yun Ye confirm that the work presented in this thesis is my own. Where information has been derived from other sources, I confirm that this has been indicated in the thesis.

Abstract

This doctoral dissertation is concerned with the study of quantum dynamics where finite dimensional systems (typically two-level 'qubits') interact with or through a set of bosonic modes, in various different configurations. Our main focus is on identifying and investigating signatures of quantum coherence emerging between the qubits in such dynamical situations.

We first present a toy model where two qubits are encoded in the single-excitation subspace of the global system and study the average fidelity of a controlled-Z (CZ) quantum gate mediated by the bosonic modes.

Next, we turn to analytically intractable spin-boson like models, by adopting the Multi-configurational Ehrenfest (MCE) method. We apply MCE to the study of the Choi fidelity of a CZ gate between two distant qubits, mediated by sets of bosonic modes (including sets which represent discretization of bath's continua) under different coupling Hamiltonians. The testing of the MCE method is then pushed further by a comparative analysis with full variational approaches and adiabatic path integral techniques in a case of super-Ohmic spin-boson model. Finally, we determine a general error bound applicable to most approximated treatments of unitary quantum evolutions, and suitable to compare MCE with other numerical techniques for the study of spin-boson dynamics.

Acknowledgments

Foremost, I am very grateful to my supervisor, Dr Alessio Serafini, the very person evoking my initial desire to study at UCL. While working with him, his thorough and critical attitude highlighted many of my weaknesses, which I was blind to realize by myself, and hence made me grow as a student and as a researcher. Without his inspiration, mathematical expertise, and great devotion, the thesis would have never been completed. I owe him my deepest appreciation for having been extremely patient and supportive with me.

I wish to thank my collaborator Dmitrii Shalashilin for clarifying the tricky places in Multi-configurational Ehrenfest numerics, despite my poorly written, massive and repeated emails. I would also like to thank Zhen-Biao Yang and my former Msc. supervisor Prof. Shi-Biao Zheng (whom I am indebted to for being consistently supportive and thoughtful) for fruitful collaboration.

I would like to thank Abolfazl Bayat, Rui Zhang and Lian-Heng Tong for the help they gave me with the programming. Special thanks go to Hannu Wichterich, for his extraordinary patience and kindness in helping me to sort out any technical problem I would encounter.

Let me also thank all the members of the AMOPP group at UCL, particularly Matty Hoban (who devoted huge time to explain to me small things), Hussain Anwar, James Miller, Ilhan Candan, Pete Burns, Janet Anders and Daniel Browne.

I am indebted to my sister, parents and grandmother, who gave me the most ultimate and unconditional love without thinking about themselves. Without

their love, encouragement and faith in me, I would not, definitely, been able to get this far.

Contents

Chapter 1

Introduction and motivations

1.1 Quantum systems interacting with an environment

1.1.1 The fundamental role of decoherence

Quantum coherence is the original resource and essence behind the emergence of the intriguing features and promising applications of quantum theory in the areas of computation [MAN00, LJL+10], communication, key distribution [GRTZ02], sensing, biometrics, metrology [ECR+07, LCF07] and technology in general. To implement quantum tasks, it is crucial to maintain coherence for sufficiently long times. But the quantum system, which we are interested in, is almost impossible to isolate from the uncontrollable environment. The interaction between the quantum system and the environmental degrees of freedom plays a general and fundamental role in physics, where it is the established mechanism to describe decoherence (whereby the bath 'drains' quantum coherence out of the system) [CL81], and even the transition to classicality in macroscopic systems [Zur91].

More specifically, interactions between controllable systems with small Hilbert spaces and large environments comprising many bosonic degrees of freedom

('modes') must be accounted for in a huge range of applications, in, *e.g.* solid state quantum computing [FI07, SMSS06], quantum impurities [BCP08], quantum chemistry and molecular dynamics, and the rising field of quantum biology [MRLAG08, PH08, CDC$^+$10, CCD$^+$09].

Therefore, it is crucial to appreciate and correctly describe the role of the ubiquitous environmental degrees of freedom [HPB02, Hor09]. Recent developments in experimental technologies and interferometric techniques, enabling one to track the behavior of quantum coherence by observable quantities in more and more diverse systems (see, *e.g.*, [CWW$^+$10]), pushes further the need for effective ways of modelling and understanding the effects of the (large) environment upon the (small) quantum system.

1.1.2 Environment: bad or good?

It is commonly recognized that the effect of the environment is basically washing out quantum coherence from the system. In the classic view "à la Zurek", the environment induces a super-selection rule, by performing a kind of indirect measurement of the system. Although the joint evolution of system and environment is a unitary transformation, such measurements are represented by a sum of projectors which can not be represented by unitary operators. This induces the decay of the phase relations between different quantum states of the system.

Hence, a vast amount of effort has been devoted to engineer solutions to suppress or eliminate the decoherent impact of the environment employing, for example, decoherence free subspaces [LCW98, ZR97], the quantum Zeno effect [MFZ$^+$08], or dynamical decoupling [GK06, FN07].

On the other hand, recent fascinating experiments [ECR$^+$07, LCF07], in which long-lived quantum coherence was observed, reveal that the environment may play a constructive role to sustain certain coherent features and could even be responsible for the optimised energy transfer in some photosynthetic systems.

This evokes considerable interest to treat and understand the system-environment interaction more carefully and accurately.

Moreover, the last ten years saw the birth and development of a substantial strand within quantum information and solid state physics where the environmental degrees of freedom, which are ordinarily responsible of *'dispersive'* dynamics – where the quantum information of the system usually 'disperses' in the environment, are instead seen as a *medium* through which coherent quantum effects can arise [BDD$^+$02, PH02, CVDC03, BFP03, STP06, CPA08, MNBF09]. The present thesis is an investigation along these lines: we will develop and apply techniques to study the dispersive dynamics of quantum systems interacting with bosonic environments, and identify relevant quantities to analyse the coherent signatures of such dynamics.

1.2 Quantum environments

Understanding the interplay between a quantum system and its environment is not straightforward, since the uncontrollable environment consists of a large number of degrees of freedom and how to model them well is a challenging question. Due to the typical lack of knowledge of the detailed microscopic description of the environment in most relevant situations, it is difficult to derive models capable of reproducing the observed environmental influence.

The environment is often comprised of bosonic modes in condensed matter settings like, for example, Bose-Einstein condensates coupled to atomic quantum dots or, less exotically, phononic baths for lattice vibrations, ion traps (where the vibrational normal modes in the ion traps constitute a phononic bath), optical lattices (in several configurations, for example bosonic atoms can be seen as a bosonic bath for ferminoc atoms in a Bose-Fermi mixture), quantum optics (where any atom interacts dissipatively with bosonic light modes). In these cases the environment, also termed the "bath", is treated as a huge reservoir of many

of harmonic oscillators (modes).

Furthermore, since the coupling of the system of interest with an individual mode is inversely proportional to the mode volume, it is reasonably considered as a linear coupling in the bosonic coordinate (a fact which had already been noted by Lord Rayleigh upon studying the perturbative dynamics of material harmonic oscillators). Though it is fairly weak for one individual mode, the collective effects of a large number of modes upon the quantum system is not necessarily weak and could be very strong [Eck09]. The linear coupling assumption is based on the "dipole approximation" in Lamb-Dicke regime, and therefore it may break down when the typical size of the system's wave-function gets comparable to the wavelength of the environmental field modes [Hor09]. For a critical view on the role of linear couplings in system-bath interactions, see [Ali02].

The other typical option for a bath is a spin environment. For instance, in nuclear magnetic resonance experiments, localized electronic spin dephasing is dominated by the interaction with a bath of lattice nuclear spins at low temperatures [WDS06], which causes local spectral diffusion (where the electron spin resonance frequency diffuses in frequency space) in the quantum system. We shall not deal with spin baths in this dissertation, and will only refer to bosonic baths in the following.

1.2.1 Spin-boson bath model

Let us consider a basic spin-bath interaction model where the bath is a set of bosonic modes and the localised quantum system ('spin') is just a two-level system [LCD$^+$87, LCD$^+$95].

The reason for considering a two-level spin system is mainly due to the fact that it is obviously the simplest quantum system one can study. Besides, a great number of interesting quantum systems can be restricted to a two-dimensional Hilbert space and thus considered as effective two-state systems ('qubits', in the language

of quantum information), and that qubits, quantum analogous of classical 'bits' are of great interest for quantum computation.

The whole spin-boson Hamiltonian $\hat{H}$ is typically comprised of three parts: the bare spin Hamiltonian $\hat{H}_S$, the bath Hamiltonian $\hat{H}_B$, and interaction $\hat{H}_{int}$ between them (hereafter $\hbar = 1$):

$$\hat{H} = \hat{H}_S + \hat{H}_B + \hat{H}_{int} \ , \tag{1.1}$$

$$\hat{H_S} = \frac{1}{2}(\varepsilon\hat{\sigma}_z - \Delta\hat{\sigma}_x) \ , \tag{1.2}$$

$$\hat{H_B} = \sum_{j=1}^{N} \frac{1}{2}(\frac{\hat{p}_j^2}{m_j} + m_j\omega_j^2\hat{x}_j^2) \ , \tag{1.3}$$

$$\hat{H}_{int} = \sum_{j=1}^{N} C_j\hat{\sigma}_z\hat{x}_j \ , \tag{1.4}$$

where ε is the bare tunneling bias, Δ determines the tunneling between the two levels at zero bias, $\hat{\sigma}_x$ and $\hat{\sigma}_z$ are Pauli matrices, such that $[\hat{\sigma}_x, \hat{\sigma}_y] = i\hat{\sigma}_z/2$, $\hat{p}_j$, $\hat{x}_j$, m_j, ω_j are, respectively, the momentum operator, position operator, mass and frequency of the jth bath's bosonic mode, such that $[\hat{x}, \hat{p}] = i$. The coupling with $\hat{\sigma}_x$ and $\hat{\sigma}_y$ may induce substantial physical effects. However, these effects can be included in the model above by renormalizing the tunneling matrix element Δ and the bias σ_x. Therefore, in this respect, considering a coupling to $\hat{\sigma}_z$ only is not a restriction. Note also that, by a proper local canonical transformation of the field modes [CL84], the linear coupling can be made to depend on positions alone. It should be noted that, in most applications, the coupling in the oscillator coordinates and/or momenta is linear only under the condition that the coupling to any one environmental degree of freedom is sufficiently weak [LCD$^+$87, LCD$^+$95, CL83].

For a bath at thermal equilibrium and represented by N modes, all the influence of the environment of harmonic oscillators is fully encapsulated by a spectral density function $J(\omega)$ given by [HPB02]

$$J(\omega) = \frac{\pi}{2}\sum_{j=1}^{N}\frac{C_j^2}{m_j\omega_j}\delta(\omega_j - \omega) \ , \tag{1.5}$$

which represents essentially the energy per unit of frequency of the bath and from which we can get all the information on the distribution of frequencies and couplings between the spin and environmental degrees of freedom.

For a continuum of modes, the $J(\omega)$ can usually be written as

$$J(\omega) = 2\pi\alpha\omega_c^{1-s}\omega^s\Theta(\omega_c,\omega)\,, \tag{1.6}$$

where ω_c is the so called 'cut-off frequency' of the bath, and $\Theta(\omega_c,\omega)$ is a function depending on ω_c and ω. These spectral densities are classified into three different categories: $s > 1$, $s = 1$, and $s < 1$, referring to the super-Ohmic, Ohmic and sub-Ohmic bath respectively. The parameter α is a dimensionless quantity capturing the strength of the system-bath interaction. Spectral functions corresponding to different values of s lead to various physical behavior (including different Quantum Phase Transitions) when associated to the spin-boson model. For example, $s = 3$ is known to feature dephasing due to the coupling to acoustic phonons [MN11, Ẅ98]. It has also been shown by numerical and analytical approaches that, depending on the value of s, the spin-boson model presents examples of quantum phase transitions between a delocalized and a localized phase, where the system freezes in one of the two accessible states [Eck09, CPHP11].

1.2.2 Interest of the spin-boson model

The spin-boson model is thus a good prototype to describe quantum tunneling between quantum states linearly coupled with a bath of harmonic oscillators and is capable of justifying a variety of dynamical effects [LCD$^+$87, LCD$^+$95, Wei08].

When the spectral density takes the form of a power law with an exponential cutoff, the model is commonly applied to study dissipative dynamics in atomic physics, condensed matter quantum information processing, and electron transfer in biological molecules [GOA85, ME03, ME04].

From the theoretical viewpoint, it represents a rich paradigm to investigate the crucial roles played by the environment: quantum phase transition between local-

ized and delocalized phases, dissipation, and the quantum-to-classical transition. Some examples of applications in experiments and experimental proposals involve quantum impurity systems [LHDBH07], arrays of trapped ions [PMvDC08], atomic dots coupled to a Bose-Einstein condensate bath [RFZ+05], mesoscopic metal rings [TV06], and cold atoms [OSLH08].

Although intensive efforts have been devoted to the study of the model, there are still interesting unexplored regimes like, for example, super-Ohmic regions where the memory effects of slow baths could be prominent. The spin-boson model thus provides one with width and wealth of applications, many of which are yet to be investigated.

1.3 How to study the model

Even if one can describe the model reasonably well, only very few cases can be studied analytically. The simplest of them, which however gives rise to a rather uninteresting dynamics, is the one where the tunnelling parameter Δ is set to zero, such that $\hat{\sigma}_z$ is a constant of motion and only the phases between the two quantum states are affected by the environment.

In most cases, the model is impossible to solve analytically, and thus requires either stringent approximations to be tackled, or efficient numerical approaches.

1.3.1 Approaches within the Born-Markov approximation

Several approaches at the model, like those based on the F$\acute{}$orster resonance energy transfer (FRET) theory [JNS04, JNS07] or Redfield equation [HMK05, SKS06, WKvD04], work within the standard Born-Markov approximation.

The assumptions of this regime are twofold [HPB02]. First, the Born approximation is valid when the coupling between the system and the environment are intrinsically weak and the influences of the system upon the environment is small,

such that perturbation theory can be applied. Therefore, the time evolution of the density matrix can be expanded to second order and the total system density matrix can be considered as a tensor product of two parts up to terms of the first order in the coupling Hamiltonian. Second, the Markov approximation implies that the correlation time scale of the bath is much shorter than the relevant relaxation time of the quantum dynamics of the system of interest and thus the environmental memory effects can be neglected, so that one typically ends up with a master equation depending only on a first order time derivative of the system's density matrix.

Frequently, and especially at high frequencies, like in quantum optics, the rotating wave approximation is also applied, whereby the counter-rotating terms of the interaction Hamiltonian, which would not conserve the number of excitations, are neglected. This guarantees a master equation in 'Lindblad form'.

In many realistic situations, these assumptions may break down: for example, in photosynthetic systems, the scale of the phonon characteristic relaxation time seems to be quite long compared to the dynamics of interaction between chromophores; and the perturbative treatment of the electron-phonon coupling is not justified. In this situation, the Lindblad equation [OCLOJ08, YDS05] obtained through a secular approximation does not include some relevant terms, resulting in an unfair treatment of the chromophores and bath [HC10]. As well known, the Markov approximation is only strictly satisfied if the environment is infinitely large with a continuum of frequencies.

1.3.2 Beyond Born-Markov

As we see, non-perturbative and non-Markovian treatments of the system-environment interaction are in much demand, and of significant challenge. This stimulates and pushes numerical developments in the spin-boson arena, based on quantum Monte Carlo techniques [EW92], real-time renormalization group [KS01], numerical renormalisation group [ABV07, TBAN08], quasi-adiabatic

path integrals [TGH01, MM95a, MM95b], numerical path integrals [TER$^+$09, BM82, NET10], and numerical hierarchy techniques [IF09b, TT10, IF09a], time-adaptive density matrix renormalisation group treatments (t-DMRG) [DKSV04, PCHP10], Iterative Linearized density matrix (ILDM) [HC10]. Analytic and semi-analytic methods based on the 'polaron transform' have also been very successful [Naz09, CPHP11].

Each approach possesses its own advantages and disadvantages. Quantum Monte-Carlo, employing random sampling to solve the exponential increase of the dimension of the Hilbert space with the number of degrees of freedom, faces the difficulties of negative transition probabilities at low temperatures [ZKAHD07, BLTV05], as well as problems in extracting the dynamical information on the real frequency axis [EM94, V̈98].

Numerical renormalisation group (NRG), numerical path integral, numerical hierarchy techniques are all restricted to certain spectral densities of the bath, and become less efficient when decreasing temperatures and facing complex internal environmental dynamics. Quasi-adiabatic path integral (QUAPI) techniques are particularly interesting, as they allow for the analytic integration of the field and, by identifying an adiabatic propagator and non-adiabatic corrections to it, are likely to perform particularly well at relatively long times.

The time-dependent density matrix renormalization group approach is applied to the spin-boson model in two steps: first, by adopting a suitable description in terms of special polynomials, the system is mapped onto linear chain (of bosons and two-level systems). Then, the standard t-DMRG techniques are applied, where the whole chain is divided into subsystems across links, and an adaptive time-varying truncated basis is inferred from the Schmidt decomposition of the density matrix [CHP11]. The basis states form a good representation of the wave-function and keep them at low dimensionality.

The Polaron transformation (representation) [Naz09, JCRE08, Jan09] works by displacing the bath oscillators depending on the system state, and allows one to

analyse in terms of master equations a much broader range of parameters' space comparing to the original representation. It establishes a bridge from weak to strong coupling regimes, although it is still subject to certain conditions on the driving strength [MN10] (For instance, Coulombic energy transfer strength for a donor-acceptor pair must not become the largest energy scale in the system [MN11]).

It would be convenient to develop and test a numerical method capable of handling various spin-boson like dynamics in a wide range of spectral densities and other dynamical and thermodynamical parameters. With their extreme in-built flexibility, variational approaches like the multi-configurational time-dependent Hartree (MCTDH) method (see Chapter 3), along with the as of yet less tested t-DMRG adaptation presented above, hold promise to become such an ultimate tool for the study of spin-boson dynamics. In this thesis we will explore and test another, in a sense 'modified', variational approach to the solution of the spin-boson Schrödinger equation, that goes under the name of multi-configurational Ehrenfest (MCE) [Sha09]. Our strategy will have the advantage of sharing many of the typical advantages of the other variational approaches, while being at the same time particularly light in terms of computational resources and relatively easy to program.

1.4 Overview of the thesis

The structure of the thesis is as follows.

In Chapter 2, we conduct a preliminary study where we address a case of distributed quantum information processing: by adopting a particular qubit encoding configuration to restrict the whole system in the single-excitation Hilbert space, we show that highly reliable Controlled-Z gates between the qubits could be mediated by a discrete set of bosonic modes. In this case we will be able to treat a somewhat 'dispersive' dynamics (in the sense that the quantum infor-

mation could in principle be kept in the bosonic degrees of freedom, out of the qubits' reach) analytically.

In order to explore more generic and complex quantum systems, we then turn to the 'Multi-Configurational Ehrenfest' (MCE) method, essentially based on the adoption of time-dependent coherent states as a discrete 'basis grid' to represent the degrees of freedom of the bath. The spirit and working equations of MCE are laid out in Chapter 3. We then proceed to apply this method to distributed quantum information processing (Chapter 4), but under much more general conditions than in Chapter 2: we will study the Choi fidelity of an entangling quantum gate between two two-level systems interacting through a set of bosonic modes (including a discretized bath). Numerically converged signatures of quantum coherence will thus be analysed in regimes beyond perturbation theory.

In the following chapter (5), a specific case of super-Ohmic single spin spin-boson dynamics, in which the bath memory effects become important, is investigated by MCE. Our intention is benchmarking the MCE results against two well-established numerical methods: multi-configurational time-dependent Hartree (MCTDH) and Quasi-adiabatic path integrals (QUAPI). The agreement between MCE and MCTDH/QUAPI is very convincing, and shows that MCE is capable to cope well in certain challenging dynamical regimes.

Chapter 6 is dedicated to the mathematical analysis of the geometric error bound on the 2-norm distance between the "true" state of the system and the state we obtain by MCE. This part of our investigation is very general and does actually apply to most numerical approaches based on the direct solution of the Schrödingier equation on states stored in finite 'hard-disks': in fact, and perhaps most relevantly, it provides one with a heuristic recipe to compare the accuracy of different numerical methods.

Finally, conclusions and future perspectives are given in Chapter 7.

Chapter 2

Coherent effects through the single-excitation sector

2.1 Motivation

As explained in Chapter 1, coherence plays a vital role for both fundamental quantum theory and quantum applications. Thus, it is of great relevance to identify physical systems and operating regimes where coherent quantum effects are susceptible to emerge. A current paradigm for quantum information processing is provided by two subsystems (qubits), where the information usually is stored, mediated by a bosonic field [CZ95, CZKM97, vEKCZ99, Pel97, PHBK99, RNO$^+$99, ZG00, LDM$^+$03, CPGP03, Zhe04, ZZG05, SMB06, BP06, YL07, YZZ08, YZ08, Kim08, YYSZ10]. This is a building block for applications in cavity QED [Pel97, SMB06], ion traps [CZ95], for the explanation of energy transfer in biological system [FNOC10], and in several other settings.

We shall refer to the space where the mediating bosonic modes reside as a "fiber". Usually, only one of the bosonic fiber modes, or a selected few, is investigated. This assumption is reasonable if the frequency spacing in the fiber is very large and the experimental control is rigorous. However, in practice, more than one

mediating mode exists, if the fiber is too long or redundant environmental bosonic modes enter the dynamics. Therefore, the effects of this sort of modes should be taken into account as well. This Chapter launches our investigation into the conditions allowing for coherent quantum effects to take place between two qubits interacting through a set of bosonic field modes [YYZS10]. Note that, in practice, our qubits could be two-level impurities interacting with the same band of a photonic crystal [YYX$^+$11, JJWM08, LFvDN$^+$04], the internal levels of two ions interacting through the vibrational modes of an array of ions in a linear trap [PMvDC08, DP12] , or even superconducting or solid-state qubits interacting through microwave radiation.

As a signature of coherence, the fidelity of a quantum controlled-z (CZ) gate between the two qubits is employed. The reason for choosing a CZ gate is that it is capable of generating maximal entanglement, and would allow for a universal set of quantum gate operations if supplemented with single-qubit operations [BDD$^+$02]. This is central to the long-term objective of realising "distributed quantum computation" [CZ95, CEHM99], and could also be a way to realize multipartite entangled states for one-way quantum computing [RB01]. More generally, distributed computation is appealing because it would let us address individual particles (qubits) more flexibly and avoid, or at least control, unwanted interactions due to their proximity.

2.2 The prototype

As shown in Fig. 2.1a, the prototype we will address comprises two distant qubits trapped in two remote optical microcavities, linked by an optical fiber. This might represent two atoms or ions trapped in microfabricated optical cavities coupling to a common integrated optical fiber [TGD$^+$07, KSP$^+$11]. It should be emphasized that, however, by transforming to normal modes of the cavities and fiber, the prototype could be applied to more generic systems (where two qubits

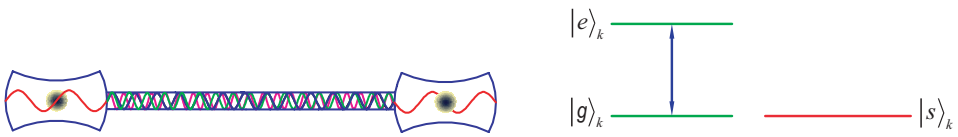

(a) Prototype (b) Level configuration

Figure 2.1: (a)The prototype: two remote nodes, wherein atoms are trapped, are linked by a medium containing many bosonic modes at different frequencies; (b)The level configuration of the two qubits ($k = 1, 2$). Notice that level $|s\rangle_1$ does not play any role in our scheme. Level $|e\rangle_2$, instead, enters the dynamics but is not used to encode any quantum information.

are directly mediated by a set of bosonic modes without two interfacing cavity fields).

In our study, we have to face two main difficulties. On the one hand, we have to deal with the customary computational difficulty of describing a many-body quantum system. On the other hand, we want to identify a situation where a controlled entangling quantum gate can be mediated by several degrees of freedom, so that we have to find a way to reduce the effects of dispersion through such a medium.

Both these issues will be solved by encoding the two qubits asymmetrically – *i.e.*, differently in the two sites – in one excited state and two kinds of ground states, following a strategy introduced in Ref. [YWSZ09] and shown in Fig. 2.1b. In the first cavity, labelled by 1, the qubit is encoded in the ground state $|g\rangle_1$ and in the excited state $|e\rangle_1$, which are coupled to each other via the cavity mode, by a rotating-wave Hamiltonian. In the second cavity, labelled by 2, the ground state $|g\rangle_2$ is also coupled to the excited state $|e\rangle_2$, but the qubit is encoded in the ground states $|g\rangle_2$ and $|s\rangle_2$, and the latter is not coupled to any state and does not evolve at all in the dynamics we consider. This configuration allows us to study the realisation of the CZ gate by restricting to the single excitation subspace, thus both reducing the computational effort required – if N is the number of

mediating modes, the size of the relevant Hilbert subspace only scales like N – and limiting the dispersive effect of the modes. Note that such a simple level structure can in principle be reproduced in non-atomic qubits as well.

We shall assume the cavity fields a_1 and a_2 to be at resonance with the atomic transitions, so that the rotating-wave approximation holds, and shall have them interacting with N modes of the "fibre" at different frequencies. In the frame rotating at the cavity frequency, the total Hamiltonian of the system is then

$$\hat{H} = \sum_{j=1}^{N} \Delta w_j b_j^\dagger b_j + \left(\sum_{k=1}^{2} g_k a_k \mid e\rangle_k\langle g \mid_k + h.c. \right) + \left(\sum_{k=1,j=1}^{k=2,j=N} v_k b_j a_k^\dagger + h.c. \right), \quad (2.1)$$

where Δw_j is the frequency difference between the kth mediating mode and the cavity mode, $a_k^\dagger$ (a_k) and $b_j^\dagger (b_j)$ are the creation (annihilation) operators for the cavity modes and the fibre modes, respectively, v_k denotes the coupling strength between the mode of cavity k and the mediating modes (possibly including a phase), and g_k represents the coupling strength between atom and field in cavity k. Note that the fibre-cavities couplings depend on the cavity but are assumed to be the same for all the fibre modes. The emphasis in our analysis is rather on the effect of the detunings Δw_j of the fibre modes.

Also, we will consider both losses of the cavities and fibre and spontaneous emission from the atoms (by far the main sources of decoherence at optical frequencies), so that our dynamics is governed by the master equation

$$\dot{\rho} = -i[\hat{H}, \rho] + \kappa \sum_{k=1}^{2} L[a_k]\rho + \gamma \sum_{k=1}^{2} L[\sigma^-]\rho + \Gamma \sum_{j=1}^{N} L[b_k]\rho \,, \quad (2.2)$$

where $L[\hat{o}] = 2\hat{o}\rho\hat{o}^\dagger - \hat{o}^\dagger\hat{o}\rho - \rho\hat{o}^\dagger\hat{o}$ is for operator $\hat{o}$, and γ, κ and Γ are the atomic spontaneous emission rate and the loss rates of the cavities – assumed, for simplicity, to be identical – and of the fibre, respectively.

2.2.1 Haar measure average

In order to check the reliability of the controlled phase gate, we want to identify a figure of merit which is independent from the specific initial state, and thus

represents a property of the dynamics itself.

This can be done by averaging the quantum fidelity between the evolved qubit density matrix and the desired CZ output, over all possible initial state. Such a process of average requires one to define a measure over the space of two qubit states. For such tasks, it is very natural to assume the *Haar measure* which, although lacking a clear operational meaning, is invariant under the unitary operations. We will hence consider the generic input state of two qubits

$$\mid \Psi\rangle_{in} = \alpha \mid e\rangle_1 \mid g\rangle_2 + \beta \mid e\rangle_1 \mid s\rangle_2 + \gamma \mid g\rangle_1 \mid g\rangle_2 + \delta \mid g\rangle_1 \mid s\rangle_2 \ , \tag{2.3}$$

where α, β, γ and δ are distributed according to the Haar measure of $U(4)$ (that is, as resulting from the application of a random Haar-distributed unitary on any fixed normalised state). The Haar measure is defined as the measure which is invariant under both left and right multiplication by any unitary transformation. A distribution borrowed from the Haar measure is a natural choice for pure quantum states if one does not want to privilege any specific direction in the Hilbert space, and hence for testing the average fidelity of a given quantum operation, as is the case here. The desired, ideal output state $|\Psi\rangle_{out}$ of the CZ gate, corresponding to the input state $|\Psi\rangle_{in}$, is

$$\mid \Psi\rangle_{out} = \alpha \mid e\rangle_1 \mid g\rangle_2 - \beta \mid e\rangle_1 \mid s\rangle_2 + \gamma \mid g\rangle_1 \mid g\rangle_2 + \delta \mid g\rangle_1 \mid s\rangle_2 \ , \tag{2.4}$$

where the phase flips only for the state $\mid e\rangle_1 \mid s\rangle_2$. Clearly, of the four superposed states defining $|\Psi\rangle_{in}$, only $|e\rangle_1|g\rangle_2$ and $|e\rangle_1|s\rangle_2$ evolve, which further simplifies our task (besides the fact that only the single excitation subspace is involved).

It is therefore straightforward to integrate Eq. (2.2) obtaining the final state $\varrho(t)$ of the system given the initial state $|\Psi\rangle_{in}|0\rangle_f$, and to evaluate the Haar average of the fidelity:

$$\bar{F} = \int_{Haar} \langle\Psi\,|_{out}\, \mathrm{Tr}_f\left[\varrho(t)\right] |\Psi\rangle_{out}\, \mathrm{d}|\Psi\rangle_{in} \ , \tag{2.5}$$

where the notation $\int_{Haar} \mathrm{d}|\Psi\rangle_{in}$ loosely refers to the fact that integration is carried over Haar-distributed input states, and Tr_f stands for the trace over the

field's degrees of freedom. In practice, this integral has been carried out by sampling the input states according to the Haar distribution and by averaging the resulting fidelity [CS06], with respect to the Haar measure on unitary group. Samples of 200 points turned out to give reliable estimates, in that the average fidelity at the first two significant figures would not change by increasing the sample's size. Henceforth, we will always report fidelities at two decimal figures. For some finer comparisons, we improved our sensitivity by increasing the integration samples. In these cases as well we will limit ourselves to two decimal digits, and will just qualitatively point out the configurations providing higher fidelities.

2.3 Results: Controlled coherent evolutions

We will study now the approximate realization of the CZ gate as detailed in the previous section, in several different situations, mainly varying the number N of fibre modes and their detuning with respect to the cavity modes. All the results obtained are summarized at the end of the section.

Hereafter, we refer to the fibre mode resonant with the atomic transition between $|e\rangle_k$ and $|g\rangle_k$ as the 'central resonant mode'. In order to find regimes with high average gate fidelity, we set $g_1 = v_1 = g$, while changing g_2, v_2 and the interaction time t. To make comparisons more clear, we define two dimensional parameters $\delta g = (g_2 - g)/g$ and $\delta v = (v_2 - g)/g$.

2.3.1 Two mediating modes: the minimum gap

Initially, all the field modes including the cavity and mediating modes are assumed to be in the vacuum state $|0\rangle_f$. To study coherent effects resulting from the competition of multiple mediating modes, we start from the case of having only two mediating modes, with the same absolute detuning Δ with respect to the frequency of the central resonant mode. Fig. 2.2 shows the average gate fidelities $\bar{F}$ for different detunings at a time where the first peak in fidelity is achieved.

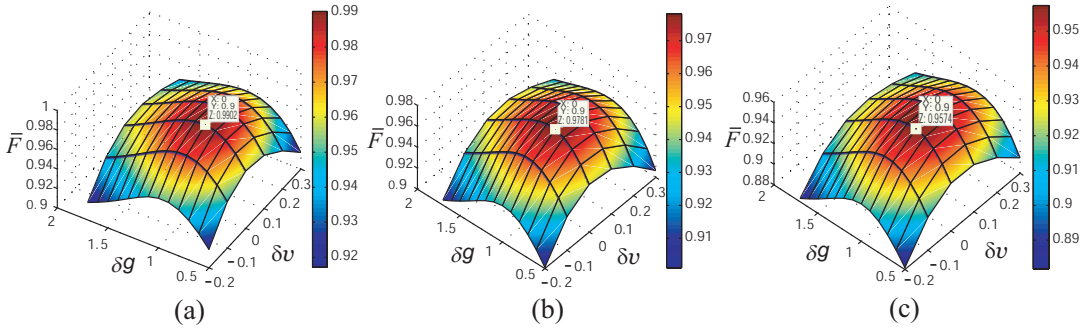

Figure 2.2: The average gate fidelity $\overline{F}$ for two detuned modes versus δg and δv, not taking losses into account, for (a): $\Delta = 0.1g$ and $gt = 4.6$, (b) $\Delta = 0.2g$ and $gt = 4.56$, (c) $\Delta = 0.3g$ and $gt = 4.54$.

Clearly, $\bar{F}$ decreases as the detuning Δ increases, since the two fibre modes become more and more off-resonant. For instance, at the peaks, $\bar{F}$ is 0.99, 0.98 and 0.96 for $\Delta/g = 0.1, 0.2, 0.3$, respectively. To put these fidelities into some context, let us mention that, depending on the noise and on the affordable computational overhead, error thresholds between 10^{-4} and 10^{-2} are believed to be required to achieve fault-tolerant quantum computation [Ste03, Kni05, RH07, Rei09].

Typically, when Δ reaches $0.45g$, and the gap between the two modes becomes comparable to the interaction strength g, the average gate fidelity $\bar{F}$ drops to 0.90. As a reference, we will say that $0.9g$ is the "minimum gap", within which "high fidelity" (90%) can still be recovered with two mediating off-resonant modes. In a cavity QED implementation with $g \simeq 1$ GHz, this gap would correspond to a fibre length l of around one meter, since the spacing of two neighbouring mediating modes is approximately $c\pi/l \simeq 10^9\,\mathrm{Hz\,m}/l$.

As shown in Fig. 2.3, $\bar{F}$ decreases by around 4%, when losses are included for $\gamma = \kappa = \Gamma = 10^{-2}g$. Further numerical analysis showed that for $\gamma = \kappa = \Gamma = 10^{-3}g$, the optimal fidelities decrease by around 0.5%. These findings are in agreement with previous studies [SMB06] arguing that, for nearly resonant couplings like the present one, average fidelities are virtually unaffected for loss to coupling strengths ratios around 10^{-4}, are only slightly affected for ratios around 10^{-3}, and start

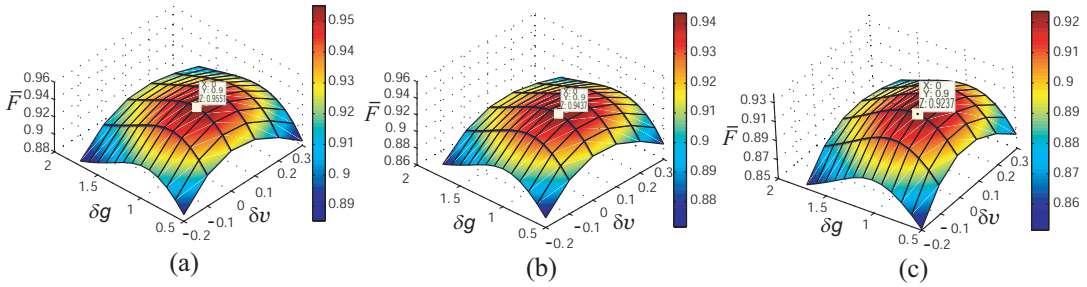

Figure 2.3: The average gate fidelity $\overline{F}$ for two detuned modes versus δg and δv for loss rates $\gamma = \kappa = \Gamma = 10^{-2}g$, and for $\Delta = 0.1g$ and $gt = 4.6$ (a), $\Delta = 0.2g$ and $gt = 4.56$ (b), and $\Delta = 0.3g$ and $gt = 4.54$ (c).

to affect the fidelity significantly – between 1 and 10% – when such ratios reach 10^{-2}. Of course, observing nearly ideal levels of coherence requires a high degree of isolation. However, notice that a quantum CZ gate implemented with a fidelity of 85% would still be a remarkable signature of quantum coherence, implying the creation of substantial entanglement and of coherent off-diagonal elements in the density matrix of the two qubits.

A note about the degree of stability of the gates obtained is also in order here: a variation of the order of 0.1 in the parameters δg and δv, corresponding to a variation of about 10% in the coupling strengths, leads to a decrease in the gate fidelity of around 1%. The same degree of sensitivity occurs with respect to fluctuations in the interaction times. Notice that, while achieving a lower peak in fidelity, the performance of more off-resonant modes ($\Delta = 0.3g$ in the figures) is slightly less sensitive to imperfections, as evident from Fig. 2.2.

2.3.2 Increasing number of mediating modes

Let us now consider the case of a larger number of mediating modes. Fig. 2.4 (a) shows the case of 31 mediating modes, with frequencies equally and symmetrically spaced around the central resonant mode and filling the minimum gap. At the peak, a remarkable average fidelity $\bar{F} = 0.99$ can still be achieved: the

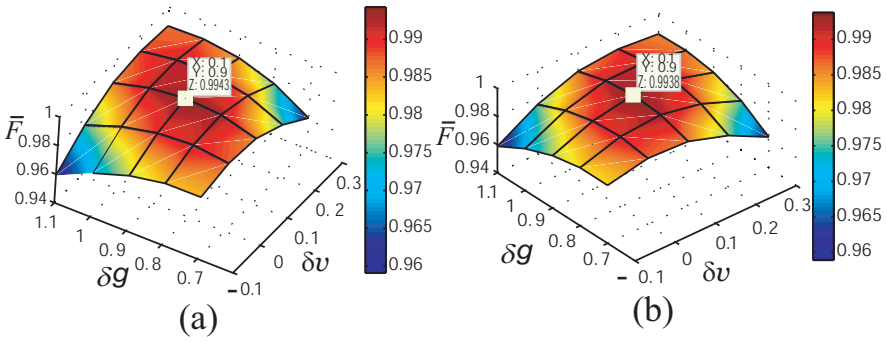

Figure 2.4: The average gate fidelity $\bar{F}$ for a set of equally spaced mediating modes within the minimum gap $\Delta = 0.45g$ versus δg and δv at the time $4.3g^{-1}$, without considering losses. In (a) 31 modes are considered; in (b) the central resonant mode has been removed.

competition between the distinct modes, which could favour the 'dispersion' of the coherence, is clearly canceled out at optimal times for such a configurations of closely packed, nearly resonant modes. In the cavity QED model, for $g \simeq 1\,\mathrm{GHz}$, the spacing considered here ($0.03g$) would correspond to a fibre of approximately 30 m: in principle, very long resonators can still mediate quantum evolutions coherently. In Fig. 2.4 (b) the same case without the central resonant mode is depicted: at the peak, the average fidelity drops very slightly but is still well above 0.99, which proves that the coherent evolution mediated by these 31 modes is not an effect due to the presence of the central resonant mode. Nor is this high fidelity a consequence of the symmetric distribution of the modes around the central resonant frequency: this has been directly tested by shifting all the frequencies of the mediating modes and does not produce any significant alteration in the maximal average fidelity, as apparent from Fig. 2.8.

To evaluate the influence of the modes very close to resonance with the cavity frequencies, we now turn to cases where the set of mediating modes are all outside the 'minimum gap'. In Fig.2.5 (b), 32 equally spaced modes are considered: half of them spans the range between $0.45g$ and $0.9g$, while the other half spans the

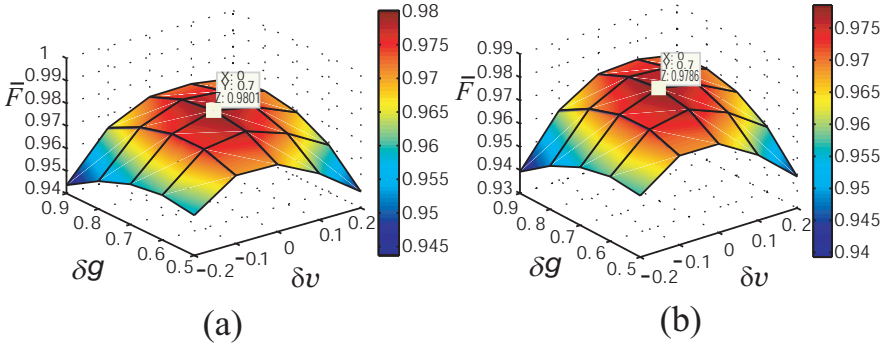

Figure 2.5: The average gate fidelity $\bar{F}$ for equally spaced modes outside the minimum gap, with detuning ranging from $0.45g$ to $0.9g$, and from $-0.45g$ to $-0.9g$ versus δg, at the time $4.48g^{-1}$, without considering losses. In (b), 32 modes are considered; in (a), a 33^{rd} mode has been added, at the central resonant frequency.

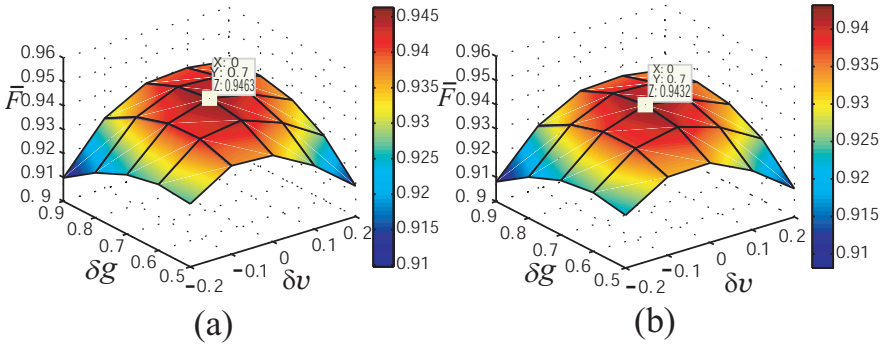

Figure 2.6: Average gate fidelity $\overline{F}$ for equally spaced modes outside the minimum gap, with detuning raging from $0.45g$ to $0.9g$, and from $-0.45g$ to $-0.9g$, at the time $4.48g^{-1}$, considering loss rates $\gamma = \kappa = \Gamma = 10^{-2}g$. (a) A 33rd mode has been added, at the central resonant frequency; (b) 32 modes are considered.

range between $-0.45g$ and $-0.9g$. Even in such an off-resonant configuration, a maximum average fidelity of 0.98 can be achieved. This is a non-trivial finding, mostly if compared to the – much lower – fidelity achievable with only two modes with frequencies *at the* minimum gap (which is about 0.9). In this case, more modes, and farther off from resonance, allow one to achieve a better performance in terms of mediated quantum coherence. This is therefore a remarkable instance

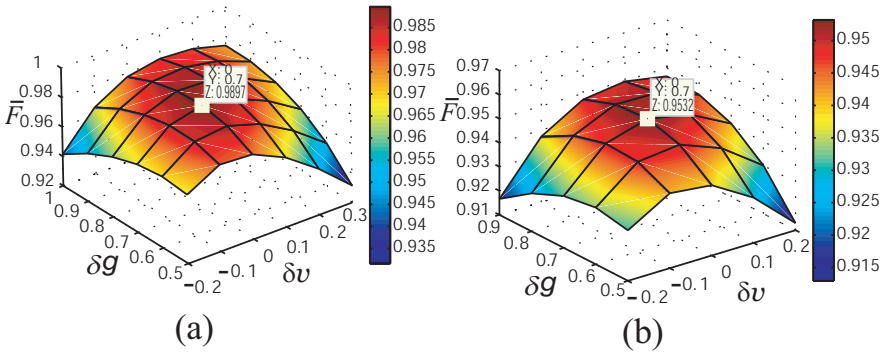

Figure 2.7: Average gate fidelity $\overline{F}$ for 16 equally spaced mediating modes outside the minimum gap, with detuning ranging from 0.45g to 0.9g at the time 4.48 g^{-1}. No losses are considered in (a), while loss rates $\gamma = \kappa = \Gamma = 10^{-2}$g are introduced in (b).

where the cooperation between the mediating modes prevails over their competition, and their effect could hence be harnessed to implement distributed coherent quantum evolutions. Fig. 2.5 (a) confirms that the addition of the central resonant mode has only a relatively modest impact on the maximal fidelity (which raises slightly but is still essentially 0.98).

Fig. 2.6 displays the effect of losses on the optimal average fidelity: for decay rates $\gamma = \kappa = \Gamma = 10^{-2}g$, the average gate fidelity $\bar{F}$ drops from around 0.98 to around 0.94. Concerning decoherence, the resilience of many modes seems to be comparable to that of few mediating modes.

Finally, in Fig. 2.7, the case of 16 modes with detuning ranging from $0.45g$ to $0.9g$ is considered. The results are very similar to the cases of 32 and 33 symmetrically detuned modes (including center resonant mode), in the same regime and interaction time. At the peak, the average gate fidelity is 0.99. Such a fidelity is reduced to 0.95 when losses with $\gamma = \kappa = \Gamma = 10^{-2}g$ are taken into account [see Fig. 2.7 (b)].

The situations addressed above, where finite regions of frequencies are not populated, although of clear theoretical interest in the context of our study, might seem rather artificial in practice. However, even for bosonic fields, such situations

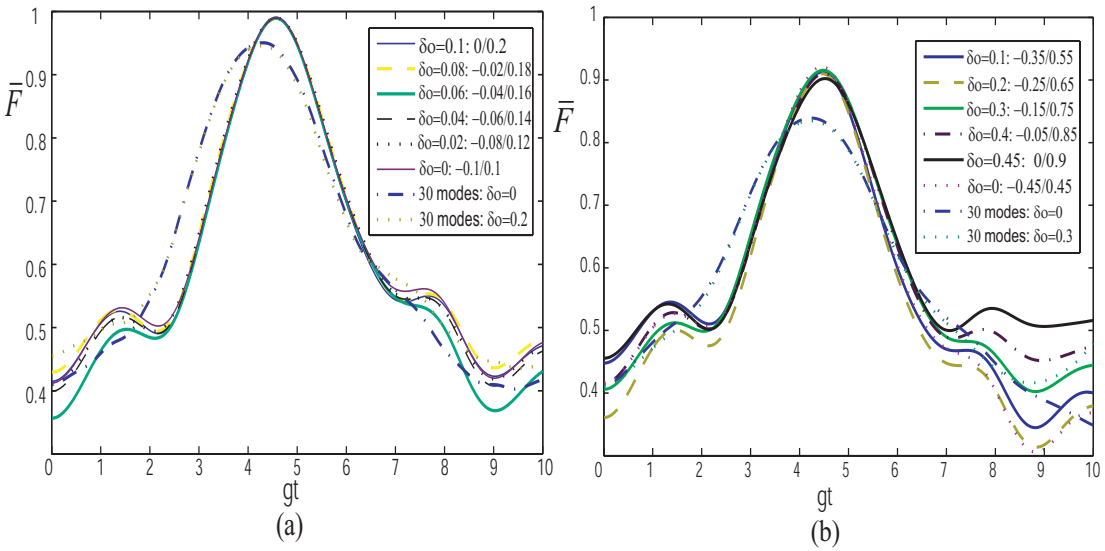

Figure 2.8: Average gate fidelity $\overline{F}$ versus time for $\delta g = 0.9$ and $\delta v = 0$, when the frequency spacing is kept constant but the centre of the set of frequencies is shifted. (a) The frequency difference between neighbouring modes is $0.2g$ and the central frequency is shifted from 0 to $0.1g$; the curves at the highest peak refer to two mediating modes, while the two curves at the lowest peak refer to 30 mediating modes. (b) The frequency difference between neighbouring modes is $0.9g$ and the central frequency is shifted from 0 to $0.45g$; the curves at the highest peak refer to two modes, while the two curves at the lowest peak refer to 30 modes. Notice that, mostly around the peaks, the curves are essentially indistinguishable from each other.

could be of relevance in systems like photonic crystals, where photonic bandgaps arise for properly modulated refractive indexes [JJWM08].

2.3.3 'Many' mediating modes

Raising the number of mediating modes to 100, one can see from Fig.2.9 (a) that very high fidelities can be obtained, still above 0.99, if all the modes are taken within the minimum gap, which is promptly explained by the presence of a large number of modes very close to resonance. More interestingly, in Fig. 2.9 (b) we

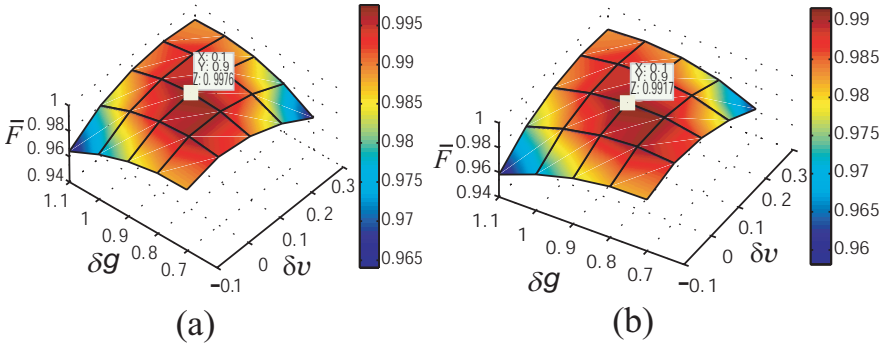

Figure 2.9: Average gate fidelity $\overline{F}$ for a set of 100 equally spaced mediating modes versus δg and δv at the time $4.3g^{-1}$, without considering losses. (a) Modes are within the minimum gap, with detuning Δ from $-0.45g$ to $0.45g$. (b) Modes have detuning Δ ranging from $-1.5g$ to $1.5g$; this plot depicts the same case of Fig. 2.4(b) but with the additional 70 modes outside the minimum gap.

have reconsidered the situation of Fig. 2.4 (b), by adding to it 35 modes in each direction with respect to the central resonant frequency. These additional modes would of course be present in the realistic modelling of a 300 m long fibre, and could approximately account for the whole field resonating in the fibre (as the effect of more and more off-resonant modes can be considered to be very small). In this case as well, the optimal average fidelity has been found to be well above 99%.

As for the stability of the quantum operations in the face of imperfections, a comparative analysis of the plots shows that a larger number of modes grant flatter and flatter fidelity peaks [compare, in particular, the two peaks of Fig. 2.8(a-b)]. So, while the fidelity obtained is slightly lower, the stability allowed by many mediating modes is higher than that of two, or even one [SMB06], mediating modes (it can be inferred from Fig. 2.9 that, for 100 modes, a 10% variation in the coupling strengths leaves the fidelity practically unchanged at two decimal figures).

2.4 Summary of results and conclusions

Summing up, in this study we have shown that:

- for only two mediating fibre modes, the optimal average fidelity $\bar{F}$ of a CZ decreases relatively rapidly with increasing gap between the modes, plummeting to 0.9 for a gap equal to $0.9g$ (where g is a reference value for the atom-cavity and cavity-fibre couplings);
- increasing the number N of mediating modes, one can still achieve highly reliable gates. For $N \simeq 100$, $\bar{F} \simeq 0.99$. This is the case regardless of the symmetry of the frequency spacing of the mediating modes with respect to the central resonant mode, and of the presence of a mode at resonance with the cavities;
- nearly perfect gates ($\bar{F} \simeq 0.98$ for $N \simeq 30$) can even be obtained for off-resonant interacting modes. In this case, a large number of modes actually outperforms fewer modes;
- loss rates around $10^{-3}g$ are necessary to operate such gates in perfect conditions (to all practical purposes); however, even rates around $10^{-2}g$ allow for coherent effects to emerge (and entanglement to be generated);
- for two mediating modes, imperfections of the order of 10% in the coupling strengths or interaction times affect the resulting fidelity by approximately one percent; this stability improves for increasing number of modes, and the fidelity is virtually unchanged for imperfections around 10% and 100 mediating modes.

Hence, we gathered evidence that coherent evolutions can be mediated by a relatively large number of bosonic modes, if appropriate qubit encoding are utilized and decay rates kept at bay. In practice, this indicates that distributed quantum information processing could be potentially achieved even if the fibers are “very

long".[1] The collective effects of multiple mediating modes populating particular frequency configurations are remarkable, and sometimes even challenge the notion that fewer modes lead to less dispersion.

Furthermore, the present model could be extended to multiple qubits: initially, all the qubits could be prepared in ground states and the interaction between the qubits and cavity modes could be frozen by keeping the transition between the excited state $|e\rangle$ and ground state $|g\rangle$ highly detuned from the cavity mode. Next, addressable controlled-z gates could be implemented by first exciting the control qubit to $|e\rangle$, and then setting the transitions of the two qubits involved at resonance with the cavity mode by applying a Stark shift through a non-resonant strong classical laser.

Clearly, though, what we studied in this chapter is essentially a toy model, based on a rather artificial encoding, which is arguably not directly relevant to fundamental studies. Also, finite temperatures were not considered, thus restricting our scope basically to quantum optics. To treat more general situations, we need more powerful techniques: in the next chapter, a versatile and powerful numerical method to the study of general spin-boson like dynamics will be presented. The case of distributed computation will hence be resumed, under much more general dynamical settings, in Chapter 4.

[1] Of course, in our discussion we are neglecting the existence of very efficient, and "long", single-mode wave-guides. We would not propose many mediating modes as a pragmatic recipe to achieve distributed quantum computation. We are rather intrigued by the general implications, both applied and theoretical, that coherent effects mediated by many degrees of freedom might have.

Chapter 3

The Multi-Configurational Ehrenfest approach

In this chapter, we will present the Multi-Configurational Ehrenfest (MCE) method, lay out its working equations and discuss its advantages and disadvantages.

3.1 Introduction

3.1.1 Quantum dynamics with time-independent basis sets

Conventionally, to solve the Schrödinger equation, a wavefunction is written as a combination of static basis states, leaving only the amplitudes (coefficients) changing with the evolution time. For instance, a wavefunction $|\Psi(t)\rangle$, can be expanded as a linear superposition of basis states:

$$|\Psi(t)\rangle = \sum_k C_k(t)|\psi_k\rangle \ , \tag{3.1}$$

where $|\psi_k\rangle$ is the kth basis state.

An obvious choice of basis for a time-independent hamiltonian $\hat{H}$ ($\hbar = 1$)is the one provided by the eigenstates of $\hat{H}$. Then:

$$\begin{aligned} |\Psi(t)\rangle &= e^{-i\hat{H}t} \sum_j C'_j |\varphi_j\rangle \\ &= \sum_j C'_j e^{-i\hat{H}t} |\varphi_j\rangle \\ &= \sum_j C'_j e^{-iE_j t} |\varphi_j\rangle \ , \end{aligned} \tag{3.2}$$

where $|\varphi_j\rangle$ is the corresponding eigenstate for the eigenvalue E_j: $\hat{H}|\varphi_j\rangle = E_j|\varphi_j\rangle$, and $C'_j = \langle\varphi_j|\Psi(t=0)\rangle$ is the initial coefficient for the basis state $|\varphi_j\rangle$. Hence, clearly, solving the quantum dynamics boils down to finding the eigenvalues of $\hat{H}$, which becomes difficult for a large number of degrees of freedoms. Suppose the total number of degree of freedom is K and the Hilbert space of each degree of freedom has dimension M, then the total Hilbert space has dimension M^K: this exponential scaling makes the exact solution of quantum dynamics of large systems intractable.

Any other approach to the solution of Schrödinger equation, like those based on the Dirac-Frenkel variational principles [Fre34] (which we will see later for time-dependent bases), ultimately has the same problem of exponential scaling.

A detailed discussion regarding the memory and computing requirements to solve the Schrödinger equation may be found, for instance, in [MW03]. Regardless of details, it is however clear that time-independent bases are not adequate to solve the dynamics of large quantum systems.

3.1.2 Time-dependent basis set

Since the early work by Heller [Hel75], adopting dynamical Gaussian wavefunctions, time-dependent approaches opened a new way to solve the Schrödinger equation. To treat several degrees of freedom, the single-configuration time-dependent self-consistent field (TDSCF) technique [GBR82, GRB82] based on time-dependent Hartree formalism was developed (where “single-configuration”

refers to the fact that the field is represented by a single direction in the Hilbert space at any time). To treat system-bath dynamics more accurately, the multi-configurational approach was later introduced [MM87, Kos88]. To escape the shortcomings of the multi-configurational self-consistent field approaches [MM87, Kos88], which depended on the prior choice of specific projection operators, alternative multi-configurational time dependent Hartree (MCTDH) [MMC90, MMC92, BJWM00, MW03] methods without introducing projection operators have been developed.

Since the idea of the multi-configurational time dependent Hartree (MCTDH) approach is very relevant to our multi-configurational Eherenfest coupled coherent states (MCE) approach, here we introduce the basic idea behind it. The MCTDH approach employs a time-dependent basis set (also termed as 'configuration')

$$|\Psi(t)\rangle = \sum_k C_k(t)|\psi_k(t)\rangle \ . \tag{3.3}$$

In general, the basis state $|\psi_k\rangle$ will be a tensor product of basis vectors of all the degrees of freedoms:

$$|\psi_k(t)\rangle = \bigotimes_{j=1}^{M} |\Phi_{k,j}\rangle \ , \tag{3.4}$$

where M is the total number of degree of freedoms. The $|\Phi_{k,j}\rangle$ is a basis vector for the jth degree of freedom.

In contrast with the traditional basis set approach where only the expansion coefficients $C_k(t)$ are time-dependent, here each basis state (also termed 'configuration' or 'basis function') $|\psi_k(t)\rangle$ is changing with time as well.[1] This gives a certain freedom to adjust the configuration during the variational procedure and

[1] While, as theoretical physicists, we would prefer the term basis 'state', or basis 'vector', we will maintain the use of 'configuration' as well throughout this dissertation, given its extensive usage in the relevant literature. To be rigorous, it should also be noted that, for infinite dimensional Hilbert spaces, these sets of vectors are obviously not 'bases' at all. In the case of our MCE based on a set of coherent states, we will sometimes refer to them as 'grids', or 'phase-space grids'.

thus a small set of configuration functions can be adequately used instead of taking all possible configurations into consideration. The reason is that, compared to static (time-independent) configurations, a relatively small number of combinations of the 'time-dependent' configurations is of significance to the quantum dynamics.

The Hartree product configuration simply consists in writing a multidimensional wavefunction as the product of one-dimensional functions:

$$|\psi_k\rangle = \prod_{j=1}^{M} |\Phi_{k,j}(t)\rangle. \tag{3.5}$$

Here, the 'secondary basis' $|\Phi_{k,j}(t)\rangle$ is time dependent and in turn described by an underlying time-independent 'primary' basis set:

$$|\Phi_{k,j}(t)\rangle = \sum_i c_{k,j,i}(t)|\varphi_{k,j,i}\rangle \ . \tag{3.6}$$

We do not intend to explain the specifics of the MCTDH method here. A detailed derivation can be found in [BJWM00]. We just wish to highlight the idea of the MCTDH approach, which is quite relevant to the Multi-configurational-Eherenfest coupled coherent states (MCE) approach we use.

Typical primary bases in modern MCTDH codes are made of tens or even hundreds functions per degree of freedom. The size of the secondary bases is, however, relatively small, even around 2 or 3 functions per degree of freedom, depending on the dynamics. It is still, of course, an exponential scaling with the number of degrees of freedom, but with a much more reduced basis (*e.g.*, 2^n instead of 100^n!).

Usually, in MCTDH programs, the degrees of freedom are grouped together so that each secondary basis function spans several degrees of freedom at the same time (a strategy that will be replicated in our MCE approach on a basis of coupled coherent states). And finally, in 'multilayer' MCTDH, each secondary basis function is in turn an MCTDH function as well (see further on). Some approaches are even based on several layers of MCTDH functions, which can be very effective but also extremely difficult to program.

Clearly, MCTDH methods scale much more favourably than the time-independent approach with the number of degrees of freedom, basically because the number of physically important single particle functions $|\Phi_{k,j}(t)\rangle$ is always much smaller than the number of basis states in the time-independent conventional approach. Thus, one is capable to approach a numerically converged result, as long as sufficiently important 'single particle' (or, better, 'single degree of freedom') functions are captured. In some cases, the method can also be combined with mean-field techniques [BJWM00] to save further computational cost.

However, MCTDH methods also have important disadvantages: in general, they are efficient only if the interaction Hamiltonians between different degrees of freedom are in simple product form, and only if the time dependent wave-packet can be expressed in a small and optimised product basis set at each time step. Often, such methods may require a very large number of variational parameters (for example, the number of basis functions) to get converged results. For large systems (like baths with complex structured spectral distribution of the modes), more variational parameters may be required.

Aiming to explore larger systems consisting of more degrees of freedom, Wang and coworkers [WT03, WT08] have extended the MCTDH approach into the multi-layer, multi-configurational time-dependent Hartree (ML-MCTDH):

$$|\Phi_{k,j}(t)\rangle = \sum_i c_{k,j,i}(t)|\varphi_{k,j,i}(t)\rangle \ , \tag{3.7}$$

where even the single particle function $|\Phi_{k,j}(t)\rangle$ is further expanded as a linear combination of time-dependent multi-configurational functions $|\varphi_{k,j,i}(t)\rangle$:

$$|\varphi_{k,j,i}(t)\rangle = \prod_{q=1}^{Q} |\phi_{k,j,i,q}(t)\rangle \ . \tag{3.8}$$

Compared to the original one-layer MCTDH, the ML-MCTDH builds more layers to allow more flexibility on the variational functions based on the Dirac-Frenkel variational principle. This essentially enables the ML-MCTDH approach to investigate more degrees of freedoms.

Holding to the same aim of investigating more degrees of freedom, the Gaussian-based multiconfiguration time-dependent Hartree method (G-MCTDH) [BMC99, BGW08] has been developed to deal with bosonic systems by using a frozen Gaussian basis set. Here, the degrees of freedom ('modes') are classified into 'primary modes' and 'secondary modes'. The 'primary modes' are treated the same as before in a rigorous way, while the 'secondary modes' are approximated collectively by parameterized basis functions. For instance, the wavefunction is written in the form [BMC99]

$$|\Psi(t)\rangle = \sum_{j_1=1}^{n_1} \cdots \sum_{j_f=1}^{n_f} C_{j_1 \cdots j_{f-1} j_f}(t) (\prod_{k=1}^{f-1} |\phi_{j_k}^k(t)\rangle) |g_j^f\rangle \,, \tag{3.9}$$

where $|g_j^f\rangle$ contains a certain number of degrees of freedom, while the remaining $f-1$ degrees of freedom are the same as single particle (one-dimensional) functions as before. Here, n_f is the total number of basis functions to represent the kth degree of freedom, and $C_{j_1 \cdots j_{f-1} j_f}$ are the time-dependent expansion coefficients.

3.2 Multi-Configurational Ehrenfest Coupled Coherent States (MCE)

3.2.1 Variational principle acting on a time-dependent basis set

Quite similarly to MCTDH and the related ML-MCTDH and G-MCTDH, for the Multi-configurational Ehrenfest Coupled Coherent States (MCE) method [Sha09], time-dependent basis states are employed, but their full variational dynamics is replaced by their "Eherenfest" dynamics (which will be explained later in this chapter). Assume we have a wavefunction $|\Psi(t)\rangle$, which is written in a Hilbert space spanned by the time-dependent basis $|V_l(t)\rangle$

$$|\Psi(t)\rangle = \sum_{l}^{N} C_l(t) |V_l(t) > \,. \tag{3.10}$$

This equation is quite similar to Eq. (3.3). However, different $|V_l(t) >$ are non-orthogonal to each other in the MCE approach such that, more generally:

$$\langle V_J | V_K \rangle = \Omega_{J,K} \tag{3.11}$$

for some time-dependent overlap matrix Ω. In essence, the MCE approach is based on the variational principle

$$\delta S = 0 \tag{3.12}$$

acting on the quantum Lagrangian

$$\mathcal{L} = \langle \Psi | i\partial_t - \hat{H} | \Psi \rangle \ , \tag{3.13}$$

whose action is defined as

$$S = \int \mathcal{L} dt \ . \tag{3.14}$$

In Eq. (3.13), we understand the time-derivative operator to act on the right. This is not really relevant: the same evolution equations would be obtained by letting it act on the left.

From Eq. (3.12), one can obtain the Euler-Lagrange equations of motion for the amplitudes (expansion coefficients) *and* for the basis states, given their parametrization.

The motion of the amplitudes is given by:

$$\frac{\partial \mathcal{L}}{\partial C_J^*} = \frac{d}{dt} \frac{\partial \mathcal{L}}{\partial \dot{C}_J^*} \ . \tag{3.15}$$

Actually, Eq. (3.15) is equivalent to the Schrödinger equation:

$$\begin{aligned}\mathcal{L} &= \langle\Psi|i\hat{\partial}_t - \hat{H}|\Psi\rangle \\ &= \frac{i}{2}\sum_{J=1,K=1}^{J=N,K=N} C_J^*\dot{C}_k\Omega_{J,K} - \frac{i}{2}\sum_{J=1,K=1}^{J=N,K=N}\dot{C}_J^* C_K\Omega_{J,K} \\ &+ \frac{i}{2}\sum_{J=1,K=1}^{J=N,K=N} C_J^* C_K\langle V_J|\partial_{V_K}|V_k\rangle\dot{V}_K \\ &- \frac{i}{2}\sum_{J=1,K=1}^{J=N,K=N} C_J^* C_K(\langle V_J|\partial_{V_J}\rangle)|V_K\rangle\dot{V}_J \\ &- \sum_{J=1,K=1,K'=1}^{J=N,K=N,J'=N} {C_J}^*\Omega_{J,K'}H_{K'K}C_K \ ,\end{aligned} \tag{3.16}$$

where $\Omega_{J,K} = \langle V_J|V_K\rangle$ and $\hat{H}|V_{K'}(t)\rangle = \sum_{K'=1}^{N} H_{K'K}|V_K(t)\rangle$. One has then

$$\begin{aligned}\frac{\partial\mathcal{L}}{\partial C_J^*} &= \frac{i}{2}\sum_{K=1}^{N}\dot{C}_k\Omega_{J,K} \\ &+ \frac{i}{2}\sum_{K=1}^{N} C_K\langle V_J|\partial_{V_K}|V_k\rangle\dot{V}_K \\ &- \frac{i}{2}\sum_{K=1}^{N} C_K(\langle V_J|\partial_{V_J}\rangle)|V_K\rangle\dot{V}_J \\ &- \sum_{K=1,K'=1}^{K=N,K'=N}\Omega_{J,K'}H_{K'K}C_K \ ,\end{aligned} \tag{3.17}$$

and

$$\begin{aligned}\frac{d}{dt}\frac{\partial\mathcal{L}}{\partial\dot{C}_J^*} &= \frac{d}{dt}(-\frac{i}{2}\sum_{K=1}^{N} C_K\Omega_{J,K}) \\ &= -\frac{i}{2}\sum_{K=1}^{N}\Omega_{J,K}\dot{C}_K - \frac{i}{2}\sum_{K=1}^{N} C_K\dot{\Omega}_{J,K} \ ,\end{aligned} \tag{3.18}$$

where $\dot{\Omega}_{J,K} = \dot{V}_J(\langle V_J|\partial_{V_J}\rangle)|V_K\rangle + \dot{V}_K\langle V_J|(\partial_{V_K}|V_K\rangle)$. Since the $|V_J\rangle$'s form a basis (and are hence linearly independent), the inverse of the overlap matrix $\Omega_{J,K}^{-1}$ exists. Applying the variational principle

$$\frac{\partial\mathcal{L}}{\partial C_J^*} - \frac{d}{dt}\frac{\partial\mathcal{L}}{\partial\dot{C}_J^*} = 0 \tag{3.19}$$

to Eq. (3.17) and Eq. (3.18), one arrives at

$$i\sum_{K=1}^{N}\dot{C}_k\Omega_{J,K}+i\sum_{K=1}^{N}C_K\langle V_J|\partial_{V_K}|V_k\rangle\dot{V}_K=\sum_{K=1,K'=1}^{K=N,K'=N}\Omega_{J,K'}H_{K'K}C_K\ . \tag{3.20}$$

Multiplying through by $\sum_J \Omega^{-1}_{l,J}$ the equation above gives

$$i\dot{C}_l+i\sum_{J,K}^{J=N,K=N}\Omega^{-1}_{l,J}C_K\langle V_J|\partial_{V_K}|V_K\rangle\dot{V}_K=\sum_{K=1}^{K=N}H_{l,K}C_K. \tag{3.21}$$

On the other hand, from the time-dependent Schrödinger equation

$$i\partial_t|\Psi(t)\rangle=\hat{H}|\Psi\rangle, \tag{3.22}$$

one obtains

$$i\sum_{l=1}^{N}\dot{C}_l|V_l\rangle+i\sum_{K=1}^{N}C_K\dot{V}_K\partial_{V_K}|V_K\rangle=\sum_{K=1,l=1}^{K=N,l=N}H_{l,K}C_K|V_l\rangle\ . \tag{3.23}$$

Inserting the identity operator $\mathbb{I}=\sum_{l,J}|V_l\rangle\langle V_J|\Omega^{-1}_{l,J}$ into the second term on the LHS, we get that

$$i\sum_{l}\dot{C}_l|V_l\rangle+i\sum_{l,J,K}\Omega^{-1}_{l,J}\langle V_J|\partial_{V_K}|V_K\rangle\dot{V}_KC_K|V_l\rangle=\sum_{K,l}H_{l,K}C_K|V_l\rangle\ . \tag{3.24}$$

Comparing Eqs. (3.21) and (3.24), we can see that the variational principle which we shall adopt is dynamically equivalent to the Schrödinger equation, as one should expect.

3.2.2 MCE working equations

The Multi-Configurational Ehrenfest Coupled Coherent States (MCE) method is an extension of the "coupled coherent states method" [SC00, SC01a, SC01b, SC04, SSC06], which adopts coherent states (right eigenvectors of the annihilation operator) as a basis set for bosonic degrees of freedom and, at the same time, incorporates the spirit of the MCTDH based approaches.

Why choose coherent states as basis states?

Coherent states have a series of attractive properties: they are eigenstates of the annihilation operator:

$$a|Z\rangle = Z|Z\rangle, \tag{3.25}$$

and thus

$$\langle Z|a^\dagger = \langle Z|Z^* \ . \tag{3.26}$$

Therefore, if one writes the Hamiltonian operator $\hat{H}$ in the 'normal-ordered' form H_{ord} (with all the creation operators to the left of all the annihilation operators), the matrix elements of the Hamiltonian can be written out in a very simple way:

$$\langle Z_l|\hat{H}|Z_j\rangle = \langle Z_l|Z_j\rangle H_{ord}(Z_l^*, Z_j) \ . \tag{3.27}$$

The price to pay for such simplicity in expressing the Hamiltonian is that different coherent states are not orthogonal:

$$\langle Z_l|Z_j\rangle = e^{Z_l^* Z_j - \frac{|Z_l|^2}{2} - \frac{|Z_j|^2}{2}} = \Omega_{lj} \ . \tag{3.28}$$

Of course, the whole (infinite) set of coherent states constitutes an over-complete set on the bosonic Hilbert Space, such that any vector can in principle be expressed as a linear combination of coherent states.

For our numerics, we will instead have to restrict to the finite subspace spanned by a finite number of coherent states. On such a subspace, the identity operator can be expressed as

$$\mathbb{I} = \sum_{l,j} |Z_l\rangle \Omega^{-1}_{l,j} \langle Z_j|. \tag{3.29}$$

Here, $\Omega^{-1}_{l,j}$ is the inverse of the $\langle Z_l|Z_j\rangle$ matrix.

How does the MCE method work?

Multi-configurational wavefunction. The MCE method uses a standard orthogonal basis for finite-dimensional degrees of freedom and Gaussian wave packets to describe the bosonic modes. Let us consider a system comprised of

spins interacting with a bath. For the bosonic modes, multi-dimensional coherent states are used as basis states while, for spins, a regular basis is maintained. The wavefunction of the whole system can be written as a linear superposition of N-configurations (Single-configuration wavefunction equations are described in Appendix A, as an introduction to the full multi-configurational method):

$$|\Psi(t)\rangle = \sum_{l=1}^{d} \sum_{j=1}^{N} a_{l,j}(t)|\phi_l\rangle \bigotimes_{m=1}^{M} |z_j^m(t)\rangle \,, \tag{3.30}$$

where M is the total number of bath modes considered, d is the complete (entire) dimension for the finite system (for instance, spins), $a_{l,j}(t)$ are the expansion coefficients and, for each j, $|z_j^m(t)\rangle$ stands for the coherent state of mode m with eigenvalue z_j^m: $a_m|z_j^m(t)\rangle = z_j^m|z_j^m(t)\rangle$ if a_m is the annihilation operator of mode m.

For example, in the case of two spins, $|l\rangle$ could denote the four ($d = 4$) two-spin states $|\uparrow_1\uparrow_2\rangle$,$|\uparrow_1\downarrow_2\rangle$,$|\downarrow_1\uparrow_2\rangle$ and $|\downarrow_1\downarrow_2\rangle$. Each jth state of the basis 'grid' would be a tensor product of M single-mode coherent states describing the individual degree of freedoms.

A key aspect of the spirit of the MCE method is that, in each 'configuration', coherent basis states belonging to different degrees of freedoms overlap with each other ("couple" with each other, in the terminology of chemical physics), such that coherent phases between distinct degrees of freedom of the bath can be accounted for. Also, clearly, coherent basis states resident in different configurations can couple to each other too. Hence, the name "coupled coherent states" assigned to these basis grids.

Working equations. From Eq. (3.30), one obtains the quantum Lagrangian

$$\begin{aligned}\mathcal{L} &= \langle\Psi|i\frac{\partial}{\partial t} - \hat{H}|\Psi\rangle \\ &= i\sum_{l=1}^{d}\sum_{i,j=1}^{N} a_{l,i}^{*}\dot{a}_{l,j}\Omega_{ij} + i\sum_{l=1}^{d}\sum_{i,j=1}^{N} a_{l,i}^{*}a_{l,j}(\mathbf{Z}_i^{*}\dot{\mathbf{Z}}_j - \frac{\mathbf{Z}_j^{*}\dot{\mathbf{Z}}_j + \mathbf{Z}_j\dot{\mathbf{Z}}_j^{*}}{2})\Omega_{ij} \\ &- \sum_{l,n=1}^{d}\sum_{i,j=1}^{N} a_{l,i}^{*}a_{n,j}\langle\mathbf{Z}_i,\phi_l|\hat{H}|\phi_n,\mathbf{Z}_j\rangle\,,\end{aligned} \tag{3.31}$$

where $\mathbf{Z}_j = \bigotimes_{m=1}^{M}|z_j^m(t)\rangle$ and $\Omega_{ij} = \langle\mathbf{Z}_i|\mathbf{Z}_j\rangle \neq 1$.

Equations for the coherent amplitudes. Applying the variation of $a_{l,i}^{*}$:

$$\frac{\partial\mathcal{L}}{\partial a_{l,i}^{*}} - \frac{d}{dt}\frac{\partial\mathcal{L}}{\partial\dot{a}_{l,i}^{*}} = 0 \tag{3.32}$$

to Eq. (3.31), one arrives at

$$\sum_{j=1}^{N}[i\dot{a}_{l,j}\Omega_{ij} + ia_{l,j}(\mathbf{Z}_i^{*}\dot{\mathbf{Z}}_j - \frac{\mathbf{Z}_j^{*}\dot{\mathbf{Z}}_j + \mathbf{Z}_j\dot{\mathbf{Z}}_j^{*}}{2})\Omega_{ij} \; - \sum_{n=1}^{d} a_{n,j}\langle\mathbf{Z}_i,\phi_l|\hat{H}|\phi_n,\mathbf{Z}_j\rangle] = 0\,. \tag{3.33}$$

In order to increase the accessible time step for numerical integral, classical ation is introduced:

$$S_{l,j} = \int[i\frac{\dot{\mathbf{Z}}_j\mathbf{Z}_j^{*} - \mathbf{Z}_j\dot{\mathbf{Z}}_j^{*}}{2} - \langle\mathbf{Z}_j,\phi_l|\hat{H}|\mathbf{Z}_j,\phi_l\rangle]dt. \tag{3.34}$$

By rewriting the coherent amplitudes $a_{l,j}$ into a pre-exponential smooth formalism [Sha09]:

$$a_{l,j} = d_{l,j}e^{iS_{l,j}}, \tag{3.35}$$

the working equations for the expansion coefficients can become

$$\begin{aligned}i\sum_{j=1}^{N}\dot{d}_{l,j}e^{iS_{l,j}}\Omega_{ij} = \sum_{j=1}^{N}[&\delta^2 H_{l,l}(\mathbf{Z}_i^{*},\mathbf{Z}_j)d_{l,j}e^{iS_{l,j}} \\ &+ \sum_{n=1}^{d}\langle\mathbf{Z}_i,\phi_l|\hat{H}|\phi_{n\neq l},\mathbf{Z}_j\rangle d_{n\neq l,j}e^{iS_{n\neq l,j}}]\,,\end{aligned} \tag{3.36}$$

where

$$\delta^2 H_{l,l}(\mathbf{Z}_i^{*},\mathbf{Z}_j) = \langle\mathbf{Z}_i,\phi_l|\hat{H}|\phi_l,\mathbf{Z}_j\rangle - \langle\mathbf{Z}_j,\phi_l|\hat{H}|\phi_l,\mathbf{Z}_j\rangle - i\Omega_{ij}(\mathbf{Z}_i^{*} - \mathbf{Z}_j^{*})\dot{\mathbf{Z}}_j\,. \tag{3.37}$$

The empirically tested classical action $S_{l,j}$ of Eq. (3.34) plays the role of smoothing the phases of the effective expansion coefficients $d_{l,j}$, and thus allows one to enlarge the time-step of numerical simulations.

Equations for the phase space grid's trajectories. The derivation of the full variational principle applied on the z_j^m complex parameters of the Coherent basis states is reported in Appendix A, where the path from the full variational equations to the Ehrenfest dynamics is explained clearly and in detail. Alternatively, we provide here a simpler derivation of the Ehrenfest dynamics: first, let us assume that the overlap between two different coherent basis states, the entry of the matrix Ω_{ij} for $i \neq j$, to be very small and thus negligible. Under this assumption, the coherent basis states belonging to different j's do not couple to each other and the problem is, actually, reduced to the single-configuration case treated in Appendix A.

Let us then define a 'simplified' wave-function for the j-th trajectory:

$$|\tilde{\Psi}_j\rangle = \sum_{l=1}^{d} |l\rangle|\mathbf{Z}_j\rangle \ , \tag{3.38}$$

and the corresponding single-configuration Lagrangian $\tilde{\mathcal{L}}_j$ as

$$\tilde{\mathcal{L}}_j = -\sum_{l,n=1}^{d} a_{l,j}^* a_{n,j} \langle \mathbf{Z}_j, l|\hat{H}|n, \mathbf{Z}_j\rangle + i\sum_{l=1}^{d} a_{l,j}^* \dot{a}_{l,j} + i\sum_{l=1}^{d} |a_{l,j}|^2 (\frac{\mathbf{Z}_j^* \dot{\mathbf{Z}}_j - \mathbf{Z}_j \dot{\mathbf{Z}}_j^*}{2}). \tag{3.39}$$

By writing the Euler-Lagrange equation for $\mathbf{Z}_j^*$ and assuming $\frac{d}{dt}(\sum_{l=1}^{d} |a_{l,j}|^2) = 0$, one obtains the working equation for each trajectory $\mathbf{Z}_j$:

$$\dot{\mathbf{Z}}_j = \frac{\sum_{l,n=1}^{d} a_{l,j}^* a_{n,j} \frac{\partial \langle \mathbf{Z}_j, \phi_l|\hat{H}|\phi_n, \mathbf{Z}_j\rangle}{\partial \mathbf{Z}_i^*}}{\sum_{l=1}^{d} |a_{l,j}|^2} \ , \tag{3.40}$$

which is exactly the same as Eq. (A.7), derived from the full variation of all the parameters.

In essence, the MCE approach is based on solving the system of linear Eqs. (3.36) and (3.40), which determine the parameters $a_{l,j}$ and $\mathbf{Z}_j$, and hence the quantum state of the global system. Notice that, in the Ehrenfest approximation, the

differential equations for the parameters $\mathbf{Z}_j$ are decoupled from those for the $\dot{a}_{l,j}$, such that the whole system can be solved with much less computational effort and the code is definitely easier to program. This is where the essential technical advantage of the method lies with respect to competing variational approaches (*e.g.*, MCTDH).

As shown in Appendix A, the dynamics we impose for the parameter $\mathbf{Z}_j$ is equivalent to adopting the Hamiltonian

$$H_j = \frac{\langle\tilde{\Psi}_j|\hat{H}|\tilde{\Psi}_j\rangle}{\langle\tilde{\Psi}_j|\tilde{\Psi}_j\rangle} \tag{3.41}$$

that is, in essence, a Hamiltonian where some quantum operators are replaced with their expectation values. Hence, the name "Ehrenfest dynamics", in deference to the classic theorem by Ehrenfest relating the time-derivative of expectation values to their corresponding classical equation of motions [Ehr27].

Further technical details concerning programming as well as the choice of the phase space basis grid are contained in Appendix A.

3.3 Temperature of the initial state of the field

Our method, being based on a grid of coherent states, has the added advantage of allowing for a straightforward treatment of an initial thermal state of the field's degrees of freedom.

If the latter are at zero temperature ($T = 0$), then we will just take each mode to start in the vacuum state $|0\rangle\langle 0|$ (which is easily represented since it is a coherent state itself).

More generally, assume that the bosonic field (the 'bath', comprising M modes) is initially in the canonical state ϱ_β, at thermal equilibrium at temperature $T = 1/(\beta k_B)$ with respect to its free Hamiltonian $\sum_{m=1}^{M} \omega_m b_m^\dagger b_m$ (we will set the Boltzmann constant $k_B = 1$ from now on). We can easily represent ϱ_β as a probabilistic mixture of coherent states by its Glauber-Sudarshan P-representation P_β,

defined as

$$P_\beta(\mathbf{Z}) = \frac{1}{\pi^{2M}} \int_{\mathbb{C}^M} \mathrm{e}^{|\mathbf{Y}|^2} \mathrm{e}^{\mathbf{Z}\mathbf{Y}^* - \mathbf{Z}^*\mathbf{Y}} \mathrm{Tr}\left[D_{\mathbf{Y}}\, \varrho_\beta\right] \mathrm{d}^{2M}\mathbf{Y}\,, \tag{3.42}$$

where $\mathbf{Y}$ and $\mathbf{Z}$ are complex vectors of dimension M (with entries Y_m and Z_m), and $D_{\mathbf{Y}}$ is the tensor product of displacement operators:

$$D_{\mathbf{Y}} = \bigotimes_{m=1}^{M} \mathrm{e}^{Y_m b_m^\dagger - Y_m^* b_m}\,. \tag{3.43}$$

The P-representation P_β completely determines ϱ_β, according to

$$\varrho_\beta = \int_{\mathbb{C}^M} P_\beta(\mathbf{Z}) |\mathbf{Z}\rangle\langle\mathbf{Z}| d^{2M}\mathbf{Z}, \tag{3.44}$$

and is given by the product of single-mode P-representations [SMB97]:

$$P_\beta(\mathbf{Z}) = \prod_{m=1}^{M} \left(\frac{e^{\beta\omega_m} - 1}{\pi} \exp\left(-(e^{\beta\omega_m - 1})|Z_m|^2\right)\right)\,. \tag{3.45}$$

Here, the state $|\mathbf{Z}\rangle = \bigotimes_{m=1}^{M} |Z_m\rangle$ is a tensor product of coherent states (one for each bosonic mode), so that $b_k|\mathbf{Z}\rangle = Z_k|\mathbf{Z}\rangle$.

We can hence simulate a set of bosonic modes at finite temperature $T = 1/\beta$ by sampling the Gaussian distribution of initial coherent states given by Eq. (3.45). Clearly, the quality and convergence rate of our treatment of temperature will degrade with increasing temperature: a quantitative analysis of this issue in some specific cases is reported in Appendix B.

Notice that no truncation in number basis is needed in our approach, at finite temperature. The dimension of the Hilbert space where the numerics take place is always dN.

3.4 Summary

The main advantages of the MCE method are the following:

- Like in most other similar approaches, the exponential scaling of the Hilbert space's dimension is avoided by letting all basis states describe all the degrees of freedom, at the expense of precision.

- The amplitudes and coherent basis are both originally derived from a variational principle, which is the same as G-MCTDH [BMC99]. However, MCE is smart, in the sense that the coherent state set is guided by the Ehrenfest dynamics, which simplifies the full variational dynamics. Though it is not based on the full variational principle, the Ehrenfest trajectories are not far away from it, and save a substantial computational costs.

It should be noted that the only true approximation imposed in our treatment is the use a finite number N of coherent basis states to describe bosonic modes. The fact that the coherent basis states $|\mathbf{Z}_j\rangle$ are driven by the Ehrenfest dynamics, instead of the full variational principle like the amplitudes $a_{l,j}(t)$, is not an approximation by itself. It just corresponds to a different choice of time-dependent basis. Employing the full varational principle for the amplitudes of the coherent sates would make this method identical to G-MCTDH [BMC99], demanding a much heavier computational effort. Arguably, using the full variational method for the coherent amplitudes too would give slightly better results, as the numerics would better approximate the variational method on the whole Hilbert space (we will see in a future chapter an approach to quantify and compare the precision of different methods). However, since the basis coherent states' overlaps are typically very small, and that difference between MCE and the full variational principle is proportional to such overlaps, Ehrenfest guided trajectories are usually very reliable, as we shall see.

Chapter 4

Control-Z gate through a dispersive bosonic medium

In Chapter 2, the reasons why we are interested in studying a control-Z gate between two remote nodes mediated by bosonic field modes have been clarified. On the one hand, this physical situation is a general prototype for many diverse systems (like trapped ions or impurities in photonics band gap media). On the other hand, the realisation of a control-Z gate operation allows, with supplementary single-spin unitaries, for universal gate based quantum computation. The possibility of obtaining this gate is therefore the ultimate signature of coherent quantum evolution for the two qubits system.

To avoid the exponential scaling of the Hilbert space's dimension with the number of degrees of freedom, we previously dealt with this problem by restricting the evolution to the one-excitation subspace. In order to solve more general cases, of interest for most Hamiltonians where no control of the couplings is possible and for non-zero temperatures, we employ here the multi-configurational Ehrenfest (MCE) method on a basis of coupled coherent states to deal with a relatively large number of bosonic modes (10-100).

Our aim is then to demonstrate that converged results for a sophisticated quanti-

fier like the fidelity of a specific, relevant non-local gate can be obtained, showing that Ehrenfest guided trajectories allow one to capture detailed features of coherent quantum dynamics.

To quantify the fidelity with which the control-Z gate (CZ) is realised, we will not perform the Haar measure average as in Chapter 2, which would require a large computational overhead in this case. Instead, we will map the channel resulting from the non-unitary evolution of the two qubits into a mixed quantum state, via the Choi isomorphism, and then evaluate the overlap between such a state and the pure state corresponding to the CZ gate. We will then work directly in the space of quantum operations, so that our results will be independent on any specific input state and will therefore reflect the dynamics purely. Thus, we will not have to average the fidelity over a vast number of different input states.

4.1 The model

We will consider a system of two spins one-half interacting through a bus of bosonic modes initially in a thermal state at temperature T. The full Hamiltonian of the system reads

$$\hat{H} = \sum_{k=1}^{M} \omega_k b_k^\dagger b_k + \sum_{j=1}^{2} (\epsilon_j \hat{\sigma}_{z,j} + \Delta_j \hat{\sigma}_{x,j}) + \sum_{j=1,k=1}^{j=2,k=M} g_{j,k} \hat{\sigma}_{x,j} (b_k + b_k^\dagger) \,, \tag{4.1}$$

where $\hat{\sigma}_{z,j}$ and $\hat{\sigma}_{x,j}$ are Pauli operators of the j-th spin (such that $[\hat{\sigma}_{x,j}, \hat{\sigma}_{y,k}] = i\delta_{jk}\hat{\sigma}_{z,j}/2$), $b_k(b_k^\dagger)$ is the annihilation (creation) operator corresponding to the k-th bath mode with angular frequency ω_k, ϵ_j represents the energy splitting of the two levels for the j-th spin, Δ_j accounts for the tunnelling dynamics of the j-th spin, $g_{j,k}$ is the coupling strength of the j-th atom with the k-th bath mode.

We will also consider the corresponding rotating wave Hamiltonian H_{rw}:

$$\hat{H} = \sum_{k=1}^{M} \omega_k b_k^\dagger b_k + \sum_{j=1}^{2} (\epsilon_j \hat{\sigma}_{z,j} + \Delta_j \hat{\sigma}_{x,j}) + \sum_{j=1,k=1}^{j=2,k=M} g_{j,k} (S_j^+ b_k + S_j^- b_k^\dagger) \,, \tag{4.2}$$

where S_j^- (S_j^+) is the lowering (rising) atomic operator of the j-th spin: $S_j^- =$

$S_j^{+\dagger} = \hat{\sigma}_{x,j} - i\hat{\sigma}_{y,j}$. For $\Delta_j = 0$, the Hamiltonian H_{rw} gives a good description of the dynamics when $|\epsilon_j - \omega_k| \ll |\epsilon_j + \omega_k|$, as is the case for near-resonant optical transitions. We shall however also extend our treatment to the rotating wave Hamiltonian with $\Delta_j \neq 0$, which cannot be easily diagonalised since it does not conserve the total number of excitations.

As already remarked in Chapter 2, our Hamiltonian might represent two impurities interacting via one band of modes of a photonic bandgap medium (photonic crystal) or, perhaps more easily with current technology, two specific ions in a linear array whose internal levels have been coupled to the longitudinal vibrational modes through laser light [PMvDC08, DP12, Toa09, Hu10].

In the following, we will treat finite initial temperatures of the bosonic modes by sampling the initial coherent states of the modes according to the probability distribution given in Eq. (3.45), as described in the previous chapter.

4.2 The figure of merit

4.2.1 The Choi-Jamiolkowski map

In order to evaluate a gate fidelity F independently from the initial state of the spin-field system, we employ the Choi channel-state duality to map linear quantum operations on a Hilbert space $\mathcal{H}$ into quantum states on a Hilbert $\mathcal{H} \bigotimes \mathcal{H}$ (more commonly refereed to as the "Choi-Jamiolkowski" map).

The Choi map between a generic completely positive (CP) linear operation Ω on the Hilbert space $\mathcal{H}$ and a quantum state ρ_Ω on the Hilbert space $\mathcal{H} \otimes \mathcal{H}$ can be defined as

$$\rho_\Omega = (\Omega \otimes \mathbb{1})|\Psi\rangle\langle\Psi| \tag{4.3}$$

where $|\Psi\rangle$ is a maximally entangled state on the double space $\mathcal{H} \times \mathcal{H}$.

The map is bijective and retains all the information about the quantum operation. As will be shown in the following, it will serve our purposes very well.

4.2.2 Choi fidelity of the CZ gate

For convenience, we first re-label the four states of the computational basis for the two spins:

$$|1\rangle = |\uparrow\downarrow\rangle \,, \tag{4.4}$$

$$|2\rangle = |\uparrow\downarrow\rangle \,, \tag{4.5}$$

$$|3\rangle = |\downarrow\downarrow\rangle \,, \tag{4.6}$$

$$|4\rangle = |\uparrow\uparrow\rangle \,. \tag{4.7}$$

In our case, the maximally entangled state given by

$$|\Psi\rangle = \frac{1}{2}\sum_{J=1}^{4} |J\rangle \otimes |J\rangle = \frac{1}{2}(|1\rangle \otimes |1\rangle + |2\rangle \otimes |2\rangle + |3\rangle \otimes |3\rangle + |4\rangle \otimes |4\rangle) \,, \tag{4.8}$$

in the two-spins basis defined in (4.4-4.7).

The control-Z gate is represented by a unitary operation U_{CZ}:

$$U_{CZ}|J\rangle = f(J)|J\rangle \,, \tag{4.9}$$

where $f(J) = 1$ for $J = 1, 2, 3$ and $f(J) = -1$ for $J = 4$. It means there is a phase change only for the basis state $|4\rangle$ (that is, the state of the first qubit controls the phase flip of the second one). Also, the quantum operation Γ_t acting at time t on the state of the two spins ρ is defined as

$$\Gamma_t(\rho) = Tr_B[e^{-i\hat{H}t}(\rho \otimes \rho_B)e^{i\hat{H}t}] \,, \tag{4.10}$$

where Tr_B stands for the partial trace over the bosonic field modes, and ρ_B is their state at time $t = 0$. Good CZ gate operation means that $\Gamma_t(\rho)$ is "close" to the unitary CZ gate operation.

The quantum state ρ_{CZ} corresponding to the gate unitary operation can be de-

termined as follows

$$\begin{aligned}\rho_{CZ} &= (U_{CZ}\otimes\mathbb{1})(\frac{1}{2}\sum_{J=1}^{4}|JJ\rangle)(\frac{1}{2}\sum_{K=1}^{4}\langle KK|)\\ &= (U_{CZ}\otimes\mathbb{1})(\frac{1}{4}\sum_{J,K=1}^{4}|J\rangle\langle K|\otimes|J\rangle\langle K|)\\ &= \frac{1}{4}\sum_{J,K=1}^{4}U_{CZ}(|J\rangle\langle K|)\otimes(|J\rangle\langle K|)\\ &= |\psi_{cz}\rangle\langle\psi_{cz}|\ ,\end{aligned}$$

where

$$|\psi_{cz}\rangle = \sum_{J=1}^{4}\frac{f(J)}{2}|JJ\rangle. \tag{4.11}$$

Similarly, for the quantum state corresponding to the quantum operation $\Gamma_t(\rho)$, we have

$$\rho_{\Gamma_t} = \frac{1}{4}\sum_{l,m=1}^{4}\Gamma_t(|l\rangle\langle m|)\otimes(|l\rangle\langle m|)\ . \tag{4.12}$$

Finally, the 'Choi' gate fidelity F can be defined as the overlap between $|\psi_{CZ}\rangle$ and ρ_{Γ_t}:

$$\begin{aligned}F &= \langle\psi_{cz}|\rho_{\Gamma_t}|\psi_{cz}\rangle\\ &= \sum_{j,k,l,m=1}^{4}\frac{f(j)f(k)}{16}\langle jj|[\Gamma_t(|l\rangle\langle m|)\otimes(|l\rangle\langle m|)]|kk\rangle\\ &= \sum_{j,k=1}^{4}\frac{f(j)f(k)}{16}\langle j|\Gamma_t(|j\rangle\langle k|)|k\rangle\ .\end{aligned} \tag{4.13}$$

So, considering hermiticity, 10 different $\Gamma_t(|j\rangle\langle k|)$ need to be calculated at each time. Because our numerical method is better suited at approximating the dynamics of physical states (in that physical states offer a variety of possible checks, like norm conservation, during the evolution), we have obtained the operators $\Gamma_t(|j\rangle\langle k|)$ from the dynamics of physical states. For example, $\Gamma_t(|1\rangle\langle 2|)$ is calculated as follows:

$$\begin{aligned}\Gamma_t\left(|1\rangle\langle 2|\right) = \Gamma_t\left(\frac{|1\rangle+|2\rangle}{\sqrt{2}}\frac{\langle 1|+\langle 2|}{\sqrt{2}}\right) - i\Gamma_t\left(\frac{i|1\rangle+|2\rangle}{\sqrt{2}}\frac{-i\langle 1|+\langle 2|}{\sqrt{2}}\right)\\ -\frac{1-i}{2}\left[\Gamma_t\left(|1\rangle\langle 1|\right)+\Gamma_t\left(|2\rangle\langle 2|\right)\right]\ .\end{aligned} \tag{4.14}$$

The figure of merit F is therefore a property of the open dynamics of the spins alone, and not of their initial state. Of course, we could have chosen other quantifiers, such as the fidelity of another, possibly entangling, unitary quantum gate or, more geometrically, we could have estimated the coherence of the dynamics by the largest eigenvalue of the state ρ_{Γ_t} (which quantifies how close the dynamics is to any unitary gate). However, we deemed the CZ gate fidelity to be a good signature to describe the coherence – or lack thereof – of the quantum dynamics.

The study of the quantity F requires one to follow the evolution of 16 initial states at any given time. Obtaining converged result for such a quantity is hence in general computationally demanding. It is in cases like this that, within the parameters' region where Ehrenfest trajectories are reliable, the MCE method we use stands out over competing, heavier approaches.

Note also that the relationship between F and 'quantum coherence' can be made more formal by noting that if $F \geq 1/4$ then the off-diagonal elements of the spins' density matrix ρ must be different from zero. In fact, if the latter were the case, one would have

$$F = \sum_{j,k=1}^{4} \frac{d(j)d(k)}{16} \langle j|\Gamma_t(|j\rangle\langle k|)|k\rangle = \sum_{j=1}^{4} \frac{1}{16} \langle j|\Gamma_t(|j\rangle\langle j|)|j\rangle \leq \sum_{j=1}^{4} \frac{1}{16} = \frac{1}{4}\,. \tag{4.15}$$

The results that follow have been reconstructed from all the terms $\langle j|\Gamma_t(|j\rangle\langle k|)|k\rangle$ obtained by converging the MCE method and tracing out all of the field modes. The derivation of the relevant MCE equations is included in Chapter 3 and Appendix A.

4.3 Choi fidelity results

4.3.1 Rotating wave, excitation conserving case

Let us start with the relatively simple case of $\epsilon_1 = \epsilon_2 = 0$, $\Delta = 0$ and $T = 0$ with the rotating wave approximated Hamiltonian H_{rw}. Also, for simplicity we

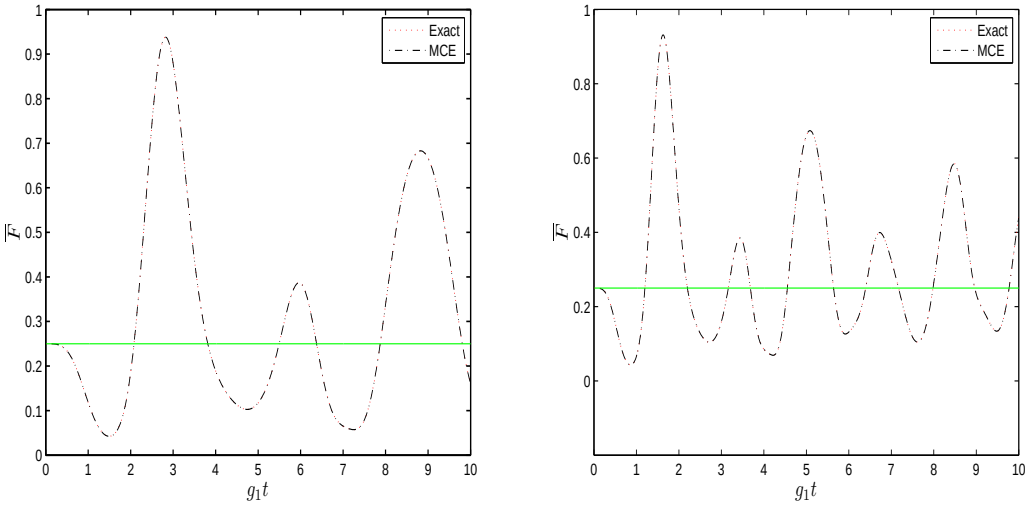

(a) one-mode (b) three-mode

Figure 4.1: Choi fidelity F versus rescaled time, for $\hat{H}_{rw}$ with $\varepsilon = \Delta = 0$, $g_1 = 1$, $g_2 = 1.9$, obtained at zero temperature by MCE method (dot-dashed) and exact analytic integration (dotted) for $M = 1$ and $\omega_1 = 0.1$ (a), and $M = 3$ and $\omega_m = 0.1m$ for $1 \leq m \leq 3$ (b). The lines $F = 0.25$ are reported for reference.

will assume $g_{j,k} = g_j$ for all j and k (the coupling of the same spin to different modes is the same). Of course this is not a crucial assumption for us, and we could assume varying couplings if needed.

Comparison with analytical results

At zero temperature and small number of modes, we have solved this model analytically by using the conservation of the number of particles. We could hence obtain a reliable benchmark to compare to our numerics.

In Fig. 4.1a, only one mode with $\omega(1) = 0.1$ is considered; while in Fig. 4.1b, three modes with $\omega(1) = 0.1$, $\omega(2) = 0.2$, $\omega(3) = 0.3$ are considered. In both cases, the MCE method shows excellent agreement (in the order of 10^{-4}) with analytical results. Also, we can see in both cases the emergence of a first, pronounced CZ fidelity peak which is around 0.9. This peak will be the main target of our

investigation.

We can already see that increasing the number of modes reduces the period accordingly: the period of 3 modes seems around $\frac{1}{\sqrt{3}}$ of that of 1 mode. This 'cooperative effect' will be confirmed on larger numbers of modes and can be easily explained by the fact that, for equal couplings, the interaction term between each spin and the field can be re-written as:

$$g_j \left(S_j^+ \sum_{k=1}^{M} b_k + \text{h.c.} \right) = \sqrt{M} g_j \left(S_j^+ d + \text{h.c.} \right) \ , \tag{4.16}$$

where the bosonic mode d is defined as $d = \left(\sum_{k=1}^{M} b_k \right) / \sqrt{M}$. The period of the coherent oscillations is hence rescaled by the factor $\sqrt{M}$. Of course, this does not mean that only one mode participates in the dynamics, since the other $M-1$ modes will couple strongly to this mediating one. In a sense, the remaining modes constitute a limited 'environment' for the mediating mode.

Another comment is in order here: the reasons why we choose such off-resonant values for the frequencies (starting from 0.1 in units of bias ϵ) is twofold. Firstly, for theoretical reasons, we are interested in regions of frequencies for the modes where the dynamics will not be dominated by a resonant or near-resonant bus mode, thus making our study fall back into a long strand of schemes where essentially a single mode mediates the quantum information transfer or entanglement generation between the distant subsystems. This way, when we introduce more modes, actual *dispersion* of the quantum coherence among the bosonic modes will take place. Secondly, after scanning a vast range of frequencies and dynamical parameters, we found this region to be a good one to host a full study, with interesting and comparable results (that is, except for the full non-rotating wave Hamiltonian, as we will see later on).

Ten modes at different temperatures

In Fig. 4.2, larger number of bath modes, $M = 10$, at different temperatures T are considered. The fidelity degrades as the temperature increases from $T = 0$,

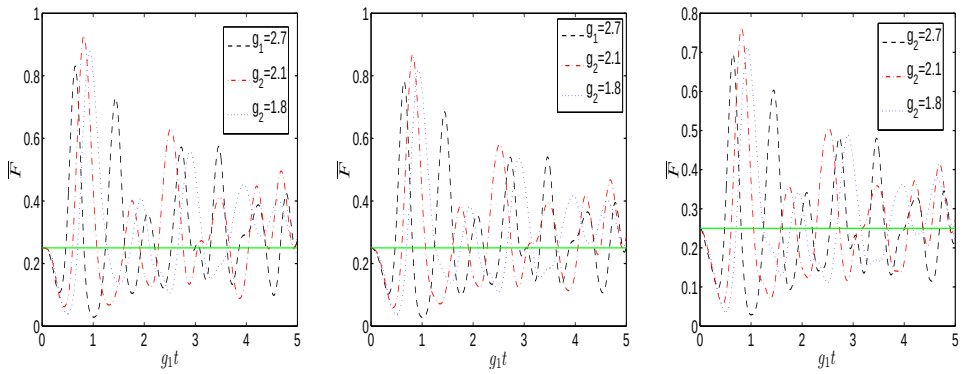

(a) $T = 0$ (b) $\beta = 1/T = 10$ (c) $\beta = 1/T = 5$

Figure 4.2: MCE results for the Choi fidelity F versus rescaled time, for $\hat{H}_{rw}$ with $\varepsilon = \Delta = 0$, $g_1 = 1$, $M = 10$, $\omega_m = 0.1m$ for $1 \leq m \leq 10$, under different values of g_2 and temperatures: (a) $T = 0$; (b) $\beta = 10$; (c) $\beta = 5$. The line $F = 0.25$ is reported for reference.

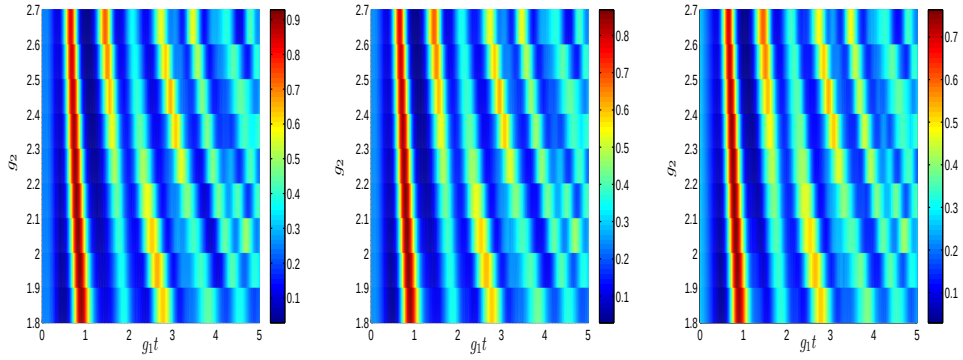

(a) $T = 0$ (b) $\beta = 1/T = 10$ (c) $\beta = 1/T = 5$

Figure 4.3: MCE results for the Choi fidelity F versus rescaled time, for $\hat{H}_{rw}$ with $\varepsilon = \Delta = 0$, $g_1 = 1$, $M = 10$, $\omega_m = 0.1m$ for $1 \leq m \leq 10$, under different values of g_2 and temperatures: (a) $T = 0$; (b) $\beta = 10$; (c) $\beta = 5$. (red stands for higher values, blue for lower values.)

$\beta = 1/T = 10$ to $\beta = 1/T = 5$. In the case of $g_2 = 2.1$, the maximum fidelity decreases from around 0.92, 0.86 to 0.76. Clearly, the coherence of the spins are better preserved at lower temperatures. Note that the range of frequencies and

temperatures we address extends to $\beta\omega\hbar \simeq 1$, implying the involvement of around 4 states in the low frequency modes, resulting in a rather large treated portion of the Hilbert space (even if under a number-excitation conserving dynamics).

In Fig. 4.3, we set $g_1 = 1$ while changing g_2 from 2.7 to 1.8. The values of fidelity are displayed in colors (Red stands for higher values, blue for lower values.). Clearly, a stronger coupling strength g_2 achieves the first peak more quickly. More importantly, we were able to scan a large range of coupling parameters and to identify the optimal value $g_2 \simeq 2.1$, where the fidelity F of the CZ gate is maximum. A similar analysis could of course be directly applied to a specific system, if coupling need to be optimised to some particular task.

4.3.2 More general cases

If the tunnelling rates $\Delta_j \neq 0$, the number of excitation number is no longer conserved and analytic or semi-analytic solutions for both H and H_{rw} are only possible in very special cases. Our intention here is then to check whether the MCE approach is stable and works well in such more general cases as well.

Rotating wave Hamiltonian

Fig. 4.4 shows parameters similar to those in Fig. 4.2, but with $\epsilon = \Delta = 1$. It can be seen that the non-diagonal elements in the spin Hamiltonian make the fidelity drop with respect to the case where the transitions between the energy levels are only mediated by the field. Of course, higher temperatures induce a lower gate fidelity. The qualitative behavior of the oscillations are roughly the same at the two different temperatures $T = 0$ and $T = 0.1$. The fidelity reduces to 0 at $\Delta t \approxeq 2.5$ and then revives as time increases. The speed with which the gate is approximated is still roughly proportional to the coupling strengths g_1 and g_2. Fig. 4.5 shares similar characteristics as Fig. 4.3.

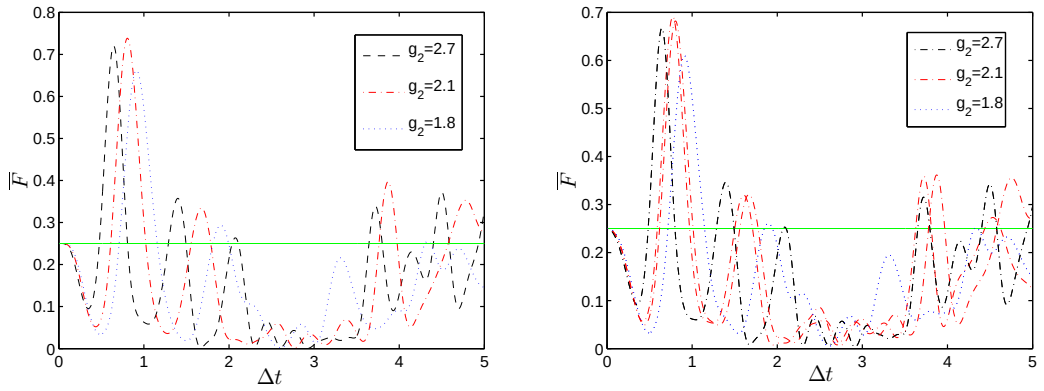

(a) $T = 0$ (b) $\beta = 1/T = 10$

Figure 4.4: MCE results for the Choi fidelity F versus rescaled time, for $\hat{H}_{rw}$ with $\varepsilon = \Delta = 1$, $g_1 = 1$, $M = 10$, $\omega_m = 0.1m$ for $1 \leq m \leq 10$ under different values of g_2 and temperatures: (a) $T = 0$; (b) $\beta = 1/T = 10$. The line $F = 0.25$ is reported for reference.

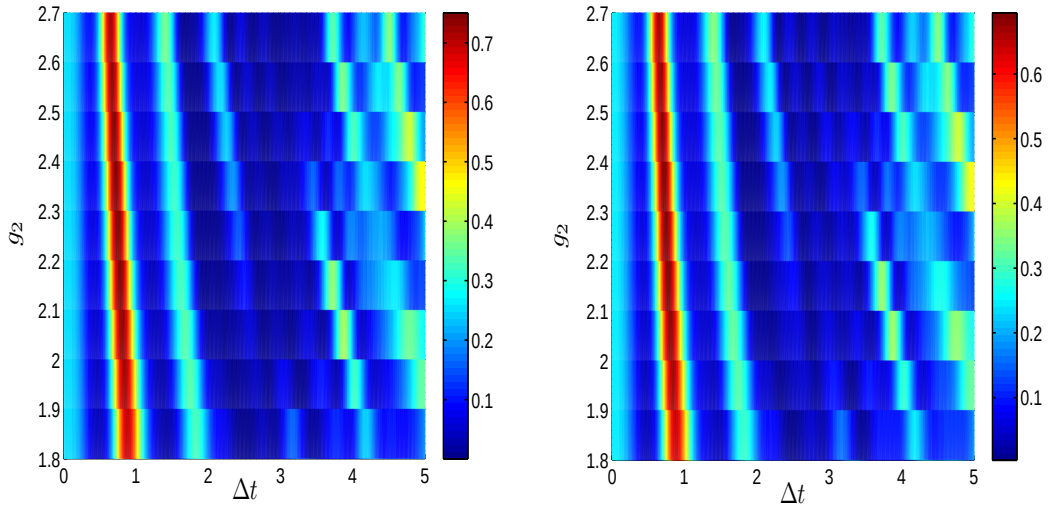

(a) $T = 0$ (b) $\beta = 1/T = 10$

Figure 4.5: MCE results for the Choi fidelity F versus rescaled time, for $\hat{H}_{rw}$ with $\varepsilon = \Delta = 1$, $g_1 = 1$, $M = 10$, $\omega_m = 0.1m$ for $1 \leq m \leq 10$ under different values of g_2 and temperatures: (a) $T = 0$; (b) $\beta = 10$. (red stands for higher values, blue for lower values.)

Non-rotating wave Hamiltonian

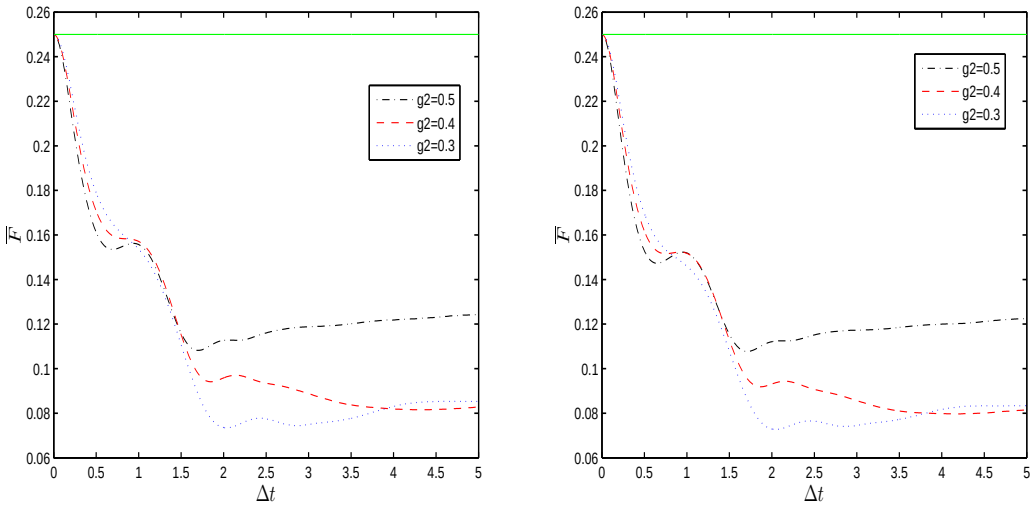

(a) $T = 0$ (b) $\beta = 1/T = 10$

Figure 4.6: MCE results for the Choi fidelity F versus rescaled time, for $\hat{H}$ with $\varepsilon = \Delta = 1$, $g_1 = 0.5$, $M = 10$, $\omega_m = 0.1m$ for $1 \leq m \leq 10$ under different values of g_2 and temperatures: (a) $T = 0$; (b) $\beta = 10$. The line $F = 0.25$ is reported for reference.

In Fig. 4.6, we report the CZ gate fidelity F for the full Hamiltonian H, including the counter-rotating terms in the spin-field coupling.

In the Ehrenfest guided approach, this coupling induces a larger time-derivative $\dot{\tilde{\mathbf{Z}}}_j(t)$ for the basis coherent states, such that the coherent states' grid propagates more rapidly. Therefore, it becomes difficult to keep the system evolution in the important dynamical regime and we could only truly track the dynamics on a short time regime. For more details on such issues, see the Appdendix C. To compensate for this problem, we have reduced the coupling strengths g_1 and g_2 accordingly to around 0.5, in order to obtain more easily converged results.

Unfortunately, and perhaps interestingly, besides these technical difficulties, we also could not find *any* region of parameters where the gate fidelity increases above 0.25, not even at zero temperature. The counter-rotating terms, rather

than just swapping excitations around the system, and so allowing for times at which the spins are relatively decoupled from the field, heat up the spins very rapidly with couplings comparable to 1, thus seriously suppressing all possibility of coherent evolutions.

4.3.3 Doubling ten modes

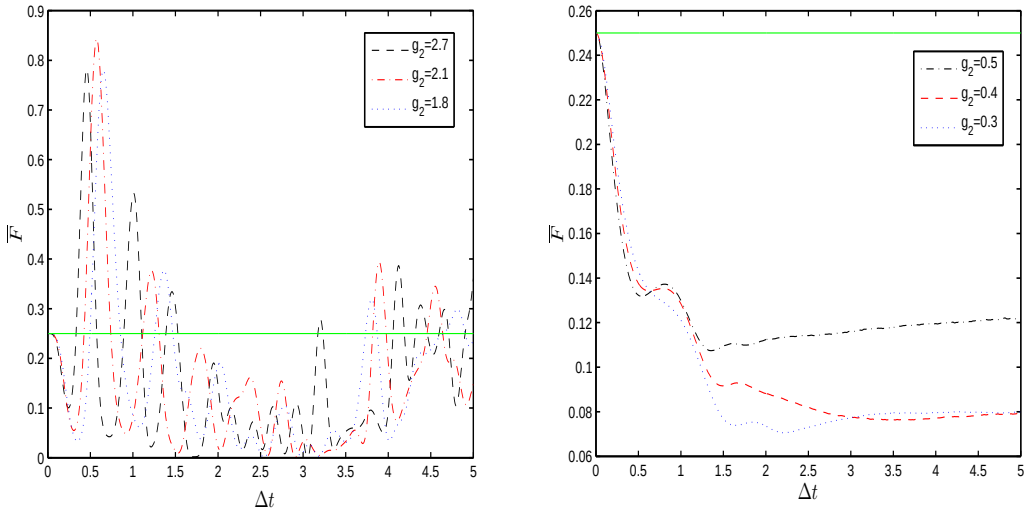

(a) H_{rw} (b) H

Figure 4.7: MCE results for the Choi fidelity F versus rescaled time at zero temperature, with $\varepsilon = \Delta = 1$, $M = 20$, $\omega_m = 0.1m$ for $1 \leq m \leq 10$, $\omega_m = 0.1(m-10)$ for $11 \leq m \leq 20$ under different values of g_2 and Hamiltonian: (a) H_{rw} with $g_1 = 1$; (b) $\hat{H}$ with $g_1 = 0.5$. The line $F = 0.25$ is reported for reference.

In Fig. 4.7 we double the number of modes in the field (from 10 to 20), to account for modes propagating in the two spatial directions, as would be the case in a 1-dimensional photonic band.

As we see, the general behavior is quite similar to corresponding cases of $M = 10$ for both H_{rw} in Fig. 4.4a and H in Fig. 4.6a. In Fig. 4.7a, the period is, as expected, around $\frac{1}{\sqrt{2}}$ as that of Fig. 4.4. Moreover, the maximum fidelity increases slightly to around 0.84 at temperature $T = 0$, which is about 10% higher than the

corresponding case of $M = 10$ displayed in Fig. 4.4a. In this case, the doubled modes conspire to mediate the interaction between the qubits. However, in the H model, the fidelity still stay below 0.25 in the regime $g_1 = 0.5$ and $g_2 = 0.5 \sim 0.1$ at temperature $T = 0$, even when the number of modes doubles from $M = 10$ to $M = 20$.

Our treatment could cope very well with this increase in the number of degrees of freedom resulting, especially at larger temperatures, in a quite large effective Hilbert space.

4.3.4 Zero Temperature Ohmic spin-boson bath

As mentioned in Chapter 1, the notion of entangling separated systems and of distributing quantum coherence by mediating the interaction with a common heat bath or other incoherent means is well established in the quantum information and condensed matter communities [LDM+02, PH02, CVDC03, BFP03, VB03, STP06, CPA08, MNBF09, BFM09]. However, the problem of studying the non-perturbative interaction of two qubits with a common bath is still, in general, a difficult one unless symmetries, like conservation of excitation number, simplify the problem.

Thus, in Fig. 4.8 we also consider the gate fidelity F mediated by a bath with Ohimc spectral density, defined by

$$J(\omega) = \frac{2}{\pi}\alpha\omega e^{-\frac{\omega}{\omega_c}} ,$$

with Kondo parameter $\alpha = 0.09$ (see Chapter 1). For the MCE approach, the way to discretize the bath mode is with coupling strengths proportional to the square root of the frequencies (discretization "w1" defined in Chapter 5), since this kind of discretization works well for the Ohmic spin-bath model [Sha09]. In particular, the frequencies and coupling strengths were chosen as follows:

$$\omega(m) = -\omega_c \ln[1 - \frac{m(1 - \exp\frac{-\omega_{max}}{\omega_c})}{M}] , \tag{4.17}$$

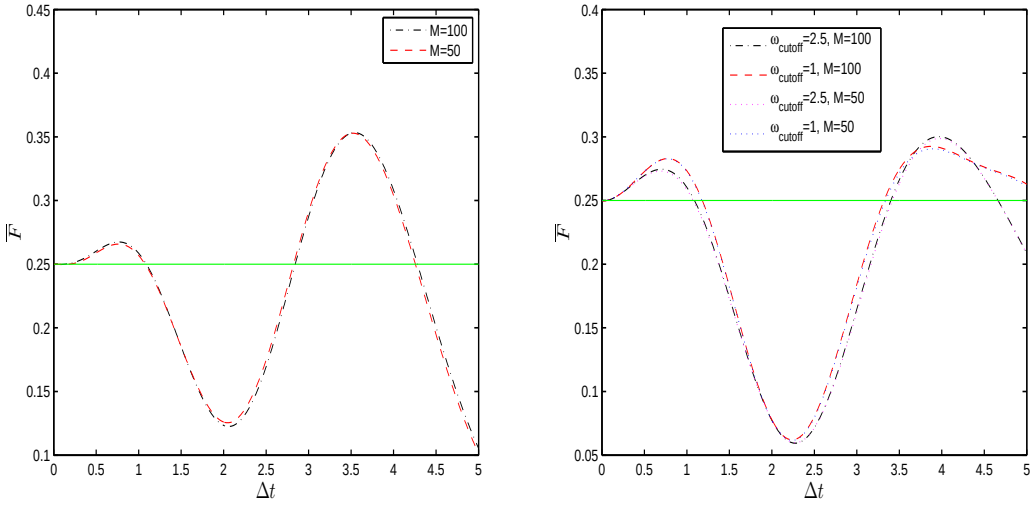

(a) H for $\omega_{cutoff} = 2.5$, $T = 0$

(b) H_{rw}: different ω_{cutoff}, $T = 0$

Figure 4.8: MCE results for the Choi fidelity F versus rescaled time at zero temperature, under $\varepsilon = \Delta = 1$ and a common Ohmic bath with $\alpha = 0.09$, and different number of bath modes for different Hamiltonians: (a) $\hat{H}$ with $\omega_c = 2.5$; (b) H_{rw} for $\omega_c = 2.5$ and $\omega_c = 1$. The line $F = 0.25$ is reported for reference.

$$g(m) = \sqrt{\frac{\omega(m)\alpha\omega_c(1 - \exp\frac{-\omega_{max}}{\omega_c})}{2M}}\,, \tag{4.18}$$

where $g(m) = g_1(m) = g_2(m)$. For $\omega_c = 2.5$, we set the $\frac{\omega_{max}}{\omega_c} = 5$ while, for $\omega_c = 1$, $\frac{\omega_{max}}{\omega_c} = 6$. For a detailed derivation of this discretization, see Appendix C. The Hamiltonian is that of the spin-boson model, as defined in Equations (1.3) and (1.4).

Here, as we see, increasing the number of bath modes from $M = 50$ to $M = 100$ does not change the fidelity much (in the order of 10^{-3}). In this sense, we regard the result as converged. For $\omega_c = 2.5$, the maximum fidelity in H is higher than that of H_{rw} within the time regime $\Delta t = 5$. With the rotating wave Hamiltonian H_{rw}, the fidelity of the case of $\omega_c = 1$ is slightly higher than $\omega_c = 2.5$, within $\Delta t \leq 3.5$ (see Appendix C).

4.4 Entanglement generation

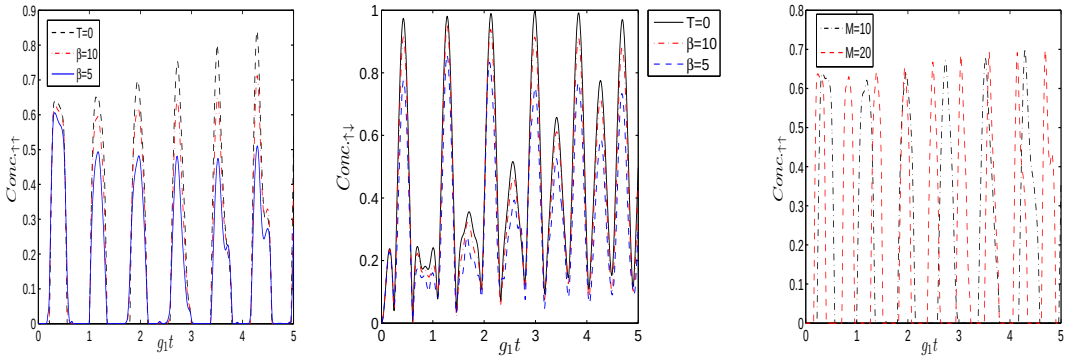

(a) $|\uparrow\uparrow\rangle$, $\epsilon = 0$, $\Delta = 0$ (b) $|\uparrow\downarrow\rangle$, $\epsilon = 0$, $\Delta = 0$ (c) $|\uparrow\uparrow\rangle$, $\epsilon = 1$, $\Delta = 1$

Figure 4.9: MCE results for the concurrence versus rescaled time at different temperatures for $\hat{H}_{rw}$ with $g_1 = 1$ and $g_2 = 2.1$. In (a), $\varepsilon = \Delta = 0$, $M = 10$ (with $\omega_m = 0.1m$ for $1 \leq m \leq 10$) and the initial state is $|4\rangle = |\uparrow\uparrow\rangle$; in (b), $\varepsilon = \Delta = 0$, $M = 10$ (with $\omega_m = 0.1m$ for $1 \leq m \leq 10$) and the initial state is $|2\rangle = |\uparrow\downarrow\rangle$; in (c), $\varepsilon = \Delta = 1$, the initial state is $|2\rangle = |\uparrow\uparrow\rangle$ and, respectively, $M = 10$ (with $\omega_m = 0.1m$ for $1 \leq m \leq 10$) for the dash dotted line and $M = 20$ (with $\omega_m = 0.1m$ for $1 \leq m \leq 10$ and $\omega_m = 0.1(m-10)$ for $11 \leq m \leq 20$) for the dashed line.

Typically, a large Choi fidelity for the (entangling) CZ gate corresponds to the generation of large entanglement between the two qubits. To support this statement, we report here a brief study on the entanglement generated between two qubits. As an entanglement quantifier, we adopt the concurrence, an entanglement monotone that can be easily calculated for a system of two qubits [Woo98]. Figs. 4.9a, 4.9b and 4.9c show the concurrence versus rescaled time for the rotating wave Hamiltonian $\hat{H}_{rw}$ with different initial states, temperatures, dynamical parameters and number of modes. The degradation of quantum entanglement due to temperature is evident (Figs. 4.9a and 4.9b), along with the speed up in the entanglement generation induced by a doubling of the modes (Fig. 4.9c).

It is also worth noting that we did not find any region of parameters where

entanglement between the two qubits is generated for the full Hamiltonian $\hat{H}$ and $M = 10$, which matches our failure in detecting CZ fidelities larger than 0.25 in such dynamics in the regimes considered here.

4.5 Summary

In this chapter, we have shown how the MCE method can be applied to the detailed study of coherent quantum evolutions, with a direct interest for quantum information processing. We considered two qubits interacting with a common set of bosonic field modes, and obtained converged results for the Choi fidelity of an entangling CZ gate between the qubits for a rather wide range of Hamiltonian parameters and field temperatures, which cannot be covered by perturbation theory or other approximate approaches.

We were able to take into account the effect of finite bath's temperatures on the reduced dynamics of the qubits, we could optimize our figure of merit within certain ranges parameters. and we also highlighted some interesting features related to the scaling of coherent signatures with the number of field modes (which we varied over the range $1 - 100$), showing that at times more mediating modes can actually be advantageous for the distribution of quantum coherence.

The main limitations of our approach lie in the difficulty of handling counter-rotating qubit-field coupling terms in the strong coupling regime (*i.e.*, when the coupling strengths are comparable to the bare dynamical frequencies of the qubits). Even in such instances, we could however reach convergence by somewhat limiting the range of the coupling strengths.

Within such limitations, the MCE approach has hence been established as a powerful tool for the detailed study of complex quantum dynamics even with relatively limited resources (desktop computers), typically for systems where discrete sets of up to 100 field modes are involved.

Understanding the limitations and advantages of the method for such applications

is very important because, on the way towards operating quantum technologies, it will be crucial to possess advanced tools, such as Ehrenfest guided trajectories, for the study and modelling of quantum systems.

Chapter 5

Comparative study of super-Ohmic spin boson dynamics

In this chapter, we apply the MCE method to the study of a set of spin boson dynamics with super-Ohmic bath spectral density. This is a difficult case to treat, because the bath becomes very coherent and thus capable of drawing and releasing quantum information from and to the system. These complex memory effects are difficult to follow, and one needs a well adapted numerical method.

At this stage, we mainly intend to benchmark our method against other established numerical techniques, and to check its internal consistency. We will also try to determine the region of dynamical parameters where the MCE method is reliable. Our ultimate aim is to establish MCE not only as a method for applied studies in well understood dynamical settings (as in the previous Chapter), but also as a viable method for the fundamental study of complex spin-boson like quantum dynamics.

As references, we will compare our results to two alternate methods: multi-configurational time-dependent Hartree (MCTDH), based on a full variational

approach [BJWM00, Wan00, WT08] and quasi-adiabatic path integrals (QUAPI), based on a path integral treatment of the bath [NPTG07].

MCE proves to agree very well with MCTDH, under an initial bath state at thermal equilibrium. This is especially comforting, because it means that the Ehrenfest dynamics for the coherent states of our basis grid captures well the important dynamical region even in the super-Ohmic case.

It will also be shown that MCE produces results close to QUAPI, as well as the systematic weak-coupling approximation (WCA) approach [GSW89]. However we suspect, by cross-comparison with MCTDH results and by assessing the internal consistence of our numerics, that our approach might be more reliable at (relatively) long times than the QUAPI results reported in [NPTG07], possibly due to the fact that we could account for a wider range of frequencies upon discretisation.

Regardless of such comparisons, after having shown its use in more applied cases in the previous chapter, we will demonstrate here the use of the MCE method for the fundamental analysis of quantum dynamics.

5.1 Super-Ohmic spin-boson Model

Let us remind the reader that the Hamiltonian of the spin-boson model consists of three terms (the notation used in the following is the same as in the section 1.2.1 of chapter 1):

$$\hat{H}_{spin} = \frac{\epsilon\hat{\sigma}_z - \Delta\hat{\sigma}_x}{2} \tag{5.1}$$

for the spin,

$$\hat{H}_B = \sum_{j=1}^{M} \frac{1}{2}\left[\frac{\hat{p}_j^2}{m_j} + m_j\omega_j^2\hat{x}_j^2\right] \tag{5.2}$$

for the bath, and

$$\hat{H}_{int} = \sum_{j=1}^{M} -C_j\hat{\sigma}_z\hat{x}_j \tag{5.3}$$

for the interaction between them. By use of the following transformation

$$\hat{p}_j = i\sqrt{\frac{m_j\omega_j}{2}}(b_j^\dagger - b_j)$$
$$\hat{x}_j = \sqrt{\frac{1}{2m_j\omega_j}}(b_j^\dagger + b_j)$$

the $\hat{H}_B$ and $\hat{H}_{int}$ can be rewritten as

$$\hat{H}_B = \sum_j^M \omega_j \left(b_j^\dagger b_j + \frac{1}{2} \right) \tag{5.4}$$

and

$$\hat{H}_{int} = -\sum_{j=1}^M C_j \hat{\sigma}_z \left[\frac{1}{\sqrt{2m_j\omega_j}} (b_j^\dagger + b_j) \right] \tag{5.5}$$

respectively. To avoid unnecessary complications, we assume a real coupling strength g_j and define it as

$$g_j = \frac{C_j}{\sqrt{2m_j\omega_j}} \, . \tag{5.6}$$

The spectral density, which provides one with all the information on the effects of the bath upon the spin, is given by:

$$G(\omega) = \frac{\pi}{2} \sum_{j=1}^M \frac{C_j^2}{m_j\omega_j} \delta(\omega - \omega_j) \, , \tag{5.7}$$

and, in the 'power-law formalism':

$$G(\omega) = 2\delta_s \omega_{ph}^{1-s} \omega^s e^{-\omega/\omega_c} \, , \tag{5.8}$$

where $s = 3$ for the super-Ohmic case.

We shall set the following values for the dynamical parameters: $\Delta = 1$, $\epsilon = 1$, $\delta_s = 0.01$, $\omega_c = 1$ and $\beta = 1/T = 10$. In such a set-up, with the cutoff frequency ω_c on the same order as the tunneling frequency Δ of the spin, the bath experiences a slow dynamics (oscillations) and its memory effect becomes important in the spin-bath interaction, thus calling for an accurate numerical approximation. The same set of parameters is investigated in Fig.(14) of [NPTG07], which can thus serve as a reference.

5.2 Discretization recipes for super-Ohmic baths

Finding the right discretization of the bath's frequencies that approximates effectively the continuous spectral density is clearly very important to treat with the spin-boson dynamics with limited computational resources.

Three different discretization recipes are introduced in this section, in order to check which one is suitable for the present model. Let us first remind that, from the density of frequency $\rho(\omega)$ as defined in appendix B, one arrives at

$$C_j^2 = \frac{2}{\pi}\omega_j m_j \frac{G(\omega_j)}{\rho(\omega_j)} \tag{5.9}$$

where $\rho(\omega_j)$ can be arbitrary but does affect the convergence efficiency, and should satisfy equation B.9 of appendix B. In the following, three choices of the density of frequency $\rho(\omega_j)$ are laid out (depending on re-normalization factors $\mathbf{a}_1$, $\mathbf{a}_2$ and $\mathbf{a}_3$, which will be determined in the following):

- w1: coupling strengths proportional to $\sqrt{\omega}$: $g_j = \sqrt{\frac{\omega_j}{\pi \mathbf{a}_1}}$, with

$$\rho(\omega_j) = \frac{\mathbf{a}_1 G(\omega_j)}{\omega_j} \ . \tag{5.10}$$

- w2: coupling strengths proportional to $\omega^{3/2}$: $g_j = \sqrt{\frac{\omega_j^3}{\pi \mathbf{a}_2}}$, with

$$\rho(\omega_j) = \frac{\mathbf{a}_2 G(\omega_j)}{\omega_j^3} \ . \tag{5.11}$$

- w3: coupling strengths independent of frequency: $g_j = \sqrt{\frac{1}{\pi \mathbf{a}_3}}$, with

$$\rho(\omega_j) = \mathbf{a}_3 G(\omega_j) \ . \tag{5.12}$$

Once the maximum frequency ω_{max} and the total number of modes M are decided, by replacing ω_j with ω_{max}, and j with M in Eq. (B.9) in Appendix B, the re-normalisation factors $\mathbf{a}_1$, $\mathbf{a}_2$ and $\mathbf{a}_3$ can be retrieved. Then the corresponding frequency ω_j can be determined. As one will see, the choice w1 seems to be the best among the three.

5.3 Comparative results

Apart from comparing our results with QUAPI and MCTDH treatments, we can also check the accuracy of the numerical approach by considering the quantities conserved by the exact dynamics. We will thus consider the quantity $\Delta E(t) = \frac{E(t)-E(0)}{E(0)}$, where $E(t)$ and $E(0)$ are, respectively, the expectation of the total Hamiltonian at spin-bath interaction time t and at the initial time. In all the figures below three parameters, the number of bath's modes M, the number of basis coherent states N and the compression parameter *comp* (defined as the inverse of standard deviation of the Gaussian distribution from which the initial coherent states are sampled, as defined in equation. A.10 in appendix A), are adjusted in order to obtain converged results.

In all our studies we will consider the population difference, essentially corresponding to $\langle\sigma_z\rangle$, which is a quantity both accessible to measurements in practical instances and very popular in the spin-boson literature.

5.3.1 Comparison with MCTDH

In Fig. 5.1, initially, the bath is in the thermal equilibrium state and the spin is in $|\uparrow\rangle$. The Hamiltonian parameters are $\Delta = 1$, $\epsilon = 1$, $\delta_s = 0.01$, $\omega_c = 1$ and $\beta = 1/\kappa T = 10$. MCE produces results very close to MCTDH[1], by setting the maximal frequency of the bath either to $\omega_{max} \to \infty$ or to $\omega_{max} = 5$. Within the time scale $\Delta t \leq 3.5$, one sees essentially complete agreement of the case of $\omega_{max} \to \infty$ with analogous MCTDH results. During the period $4 \leq \Delta t \leq 6$, the case $\omega_{max} \to \infty$ is slightly shifted upwards with respect to MCTDH, whereas, for $\omega_{max} = 5$, the population difference is subtly changed in the opposite direction. After $\Delta t \leqq 10$, the former still remains slightly higher up until $\Delta t \cong 25$, while

[1] Results kindly received from Hao-Bing Wang, as a private communication. Unfortunately, we were not informed about what primary and secondary bases were utilised for these MCTDH numerics.

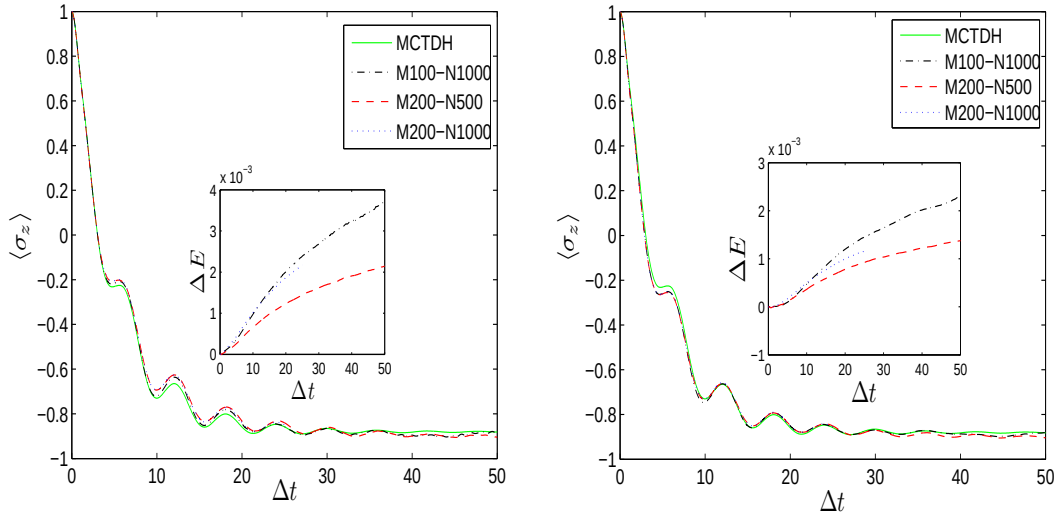

(a) $\omega_{max} \to \infty$ (b) $\omega_{max} = 5$

Figure 5.1: The expectation value of $\langle\hat{\sigma}_z\rangle$ versus rescaled time by MCTDH (green-solid) and MCE with $\Delta = 1$, $\epsilon = 1$, $\delta_s = 0.01$, $\omega_c = 1$ and $\beta = 10$, in which the bath is initially in thermal equilibrium state. The MCE results are provided with different M, N ($comp = 500$ for $N = 1000$; $comp = 1000$ for $N = 500$), under two different ω_{max}: in (a), $\omega_{max} \to \infty$; in (b), $\omega_{max} = 5$. The insert figures are the corresponding energy deviation $\Delta E(t)$ versus the rescaled time.

the latter matches MCTDH very well (the maximum discrepancy is around 6%). In the figures' inserts, we report the corresponding energy deviation $\Delta E(t)$ versus Δt. For both $\omega_{max} \to \infty$ and $\omega_{max} = 5$, $\Delta E(t)$ is of the order 10^{-3}. For $N = 1000$ (a basis grid of 1000 states), though the $\Delta E(t)$ is roughly similar, the case of $M = 100$ approaches the MCTDH closer than $M = 200$ in the two different ω_{max} considered here. This seems to indicate that, as the number of modes increases, one needs a larger and larger number of basis states to reproduce the full variational dynamics perfectly with Ehrenfest dynamics. For $M = 200$, $\Delta E(t)$ changes less in the case of $N = 500$ with $comp = 1000$ (red dash line), with respect to $N = 1000$ with $comp = 500$ (blue dot line). These internal checks strongly suggest that big compression numbers are helpful in reducing the size of

the necessary number of coherent states N.

More generally, our capability to reproduce MCTDH results by an Ehrenfest dynamics based approach is a convincing way of demonstrating that the MCE method we adopt is very well suited to the study of spin-boson dynamics, even in challenging super-Ohmic settings.

5.3.2 Comparison with QUAPI

We now intend to contrast our findings with the analysis of the super-Ohmic spin-boson which can be found in [NPTG07], where the initial system's state is different from the one mentioned above. We will hence consider a bath that was set in canonical equilibrium at $t \to -\infty$ and then let free to evolve and interact with the spin, while the spin is however constrained in the state $|\uparrow\rangle$. By the time $t = 0$, when the state of the spin is released and the spin-boson dynamics takes off, each mode k of the the bath thermalizes to a state which is obtained by acting with a displacement operator $\hat{D}(g_k/\omega_k)$ on the canonical thermal state. In our language, this simply corresponds to shifting the centers of the bath's initial state in phase space by the amount g_k/ω_k (for mode k). In the following, results for the three different discretization recipes previously introduced are included.

w1 Discretization

For the discretization w1 (with coupling strengths proportional to the square root of the frequencies), Fig. 5.2 shows that a choice $\omega_{max} \to \infty$, whilst sharing similar dynamical features with $\omega_{max} = 5$, gives results closer to QUAPI within the relatively short time scale $\Delta t \leq 20$. However, the insert in Fig. 5.2b, with lower compression number *comp*, agrees with QUAPI better than corresponding cases with large *comp*. If QUAPI results are accurate, this would suggest that the appropriate compression number should be adapted to the relevant Hamiltonian. Large *comp* means small width of the distribution of the coherent basis states.

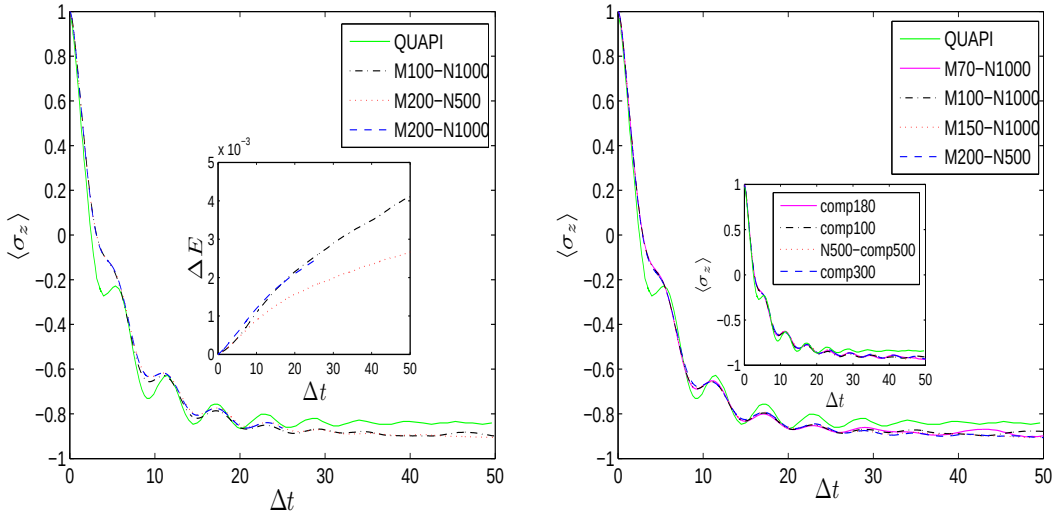

(a) $\omega_{max} \to \infty$ (b) $\omega_{max} = 5$

Figure 5.2: The expectation value of $\langle\sigma_z\rangle$ versus rescaled time by QUAPI (green-solid) and MCE (w1 discretization) with $\Delta = 1$, $\epsilon = 1$, $\delta_s = 0.01$, $\omega_c = 1$ and $\beta = 10$, for initially displaced thermal bath. The MCE results are provided with different M, N ($comp = 500$ for $N = 1000$, except $comp = 300$ for $M70 - N1000$; $comp = 1000$ for $N = 500$), under two different ω_{max}: in (a), $\omega_{max} \to \infty$; in (b), $\omega_{max} = 5$. The insert figure in (a) displays the corresponding enery deviation with respect to rescaled time, while the insert figure in (b) is still the $\langle\sigma_z\rangle$ versusing rescaled time, but under either smaller N or $comp$ (comp180, comp100, N500-comp500, comp300 represent 'M70-N200-comp180', 'M100-N1000-comp100', 'M150-N500-comp500', 'M200-N500-comp300', respectively.) .

Clearly, if *comp* is too big, thus enforcing the initial coherent states of the grid to lie very close to each other, too strong restrictions may be imposed on the initial grid and the basis grid may then degrade relatively quickly.

Fig. 5.2 shows that sensitivity to oscillatory behaviours diminishes with respect to QUAPI: this could be disadvantageous when employing the method to detect quantum coherence in composite systems.

It should be noted that, although MCE and QUAPI show relaxation at about the same time $\Delta t = 30$, the value $\langle \sigma_z \rangle$ of MCE is lower than that of QUAPI by around 6%. It is, however, very close to the WCA results showed in [NPTG07]. This discrepancy between QUAPI and variational methods in the predicted relaxation energy is probably the most striking feature of this comparison and probably deserves a deeper analysis.[2]

w2 and w3 Discretization

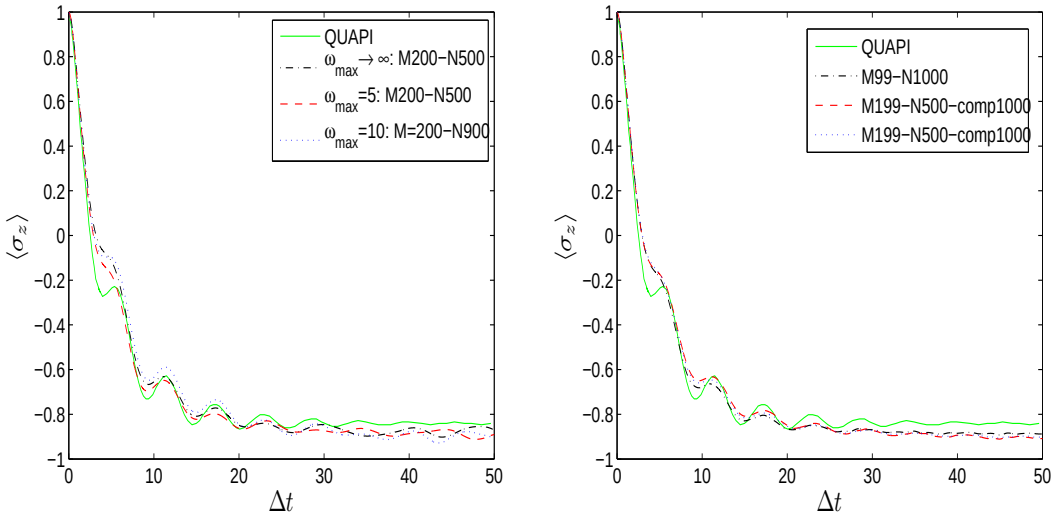

(a) w2 descretization

(b) w3 descretization

Figure 5.3: The expectation value of $\langle \sigma_z \rangle$ versus rescaled time by QUAPI (green-solid) and MCE (w2 and w3 discretization) with $\Delta = 1$, $\epsilon = 1$, $\delta_s = 0.01$, $\omega_c = 1$ and $\beta = 10$, for initially displaced thermal bath. In (a), w2 discretization under different ω_{max} and with different M and N ($comp = 500$ for $N = 1000$; $comp = 250$ for $N = 900$); In (b), w3 discretization under same $\omega_{max} \to \infty$, but with different M and N ($comp = 500$ for $N = 1000$).

In Fig. 5.3a for w2 discretization, results between $\omega_{max} \to \infty$ and $\omega_{max} = 5$ are close to each other. The feature is similar to that of w1 discretization. Moreover,

[2] We would need to scan QUAPI results for wider ranges of parameters to investigate this further.

the general behavior of the case $\omega_{max} = 10$ is not far away from that of $\omega_{max} \to \infty$ as well. This similarity arises from the fact that the spectral density $G(\omega)$ is almost 0 when ω approaches 10. Here, different N and *comp* are accounting for the discrepancies between them. This point will be further confirmed in the following section.

In Fig. 5.3b for w3 discretization under the same $\omega_{max} \to \infty$, the results of different M and N are close to each other, which shares similar characteristic as in Fig. 5.2a.

However, it is obvious that both w2 and w3 discretizations behave less smoothly and, more importantly, converge more slowly in the long time regime $\Delta t \geq 30$, compared to the w1 descretization. This indicates the w1 descretization is more suitable for the present model. That is the very reason why w1 discretization is utilized when comparing with MCTDH in Fig. 5.1.

5.3.3 Flipping the interaction Hamiltonian Phase

In this section, we want to test our numerics in terms of the effect induced by a change of the phase of the interaction between the spin and bath, by replacing g with $-g$, under the same numerical parameters ($M = 100$, $N = 500$, $comp = 150$),

As seen in Fig. 5.4a, filpping the phase of spin-bath interaction Hamiltonian, does not change the evolution at all if the initial bath is in thermal equilibrium state. This is as expected, since the initial state is then totally phase-symmetric in phase space.

However, for an initially shifted bath (to which a fixed displacement operator has been applied), the initial state of the spin-bath system is clearly not phase-invariant anymore, and the change of phase has a relevant effect. In fact, it turns out to slow the spin dynamics down. Our numerics are thus consistent as far as phase-flips in the interaction couplings are concerned.

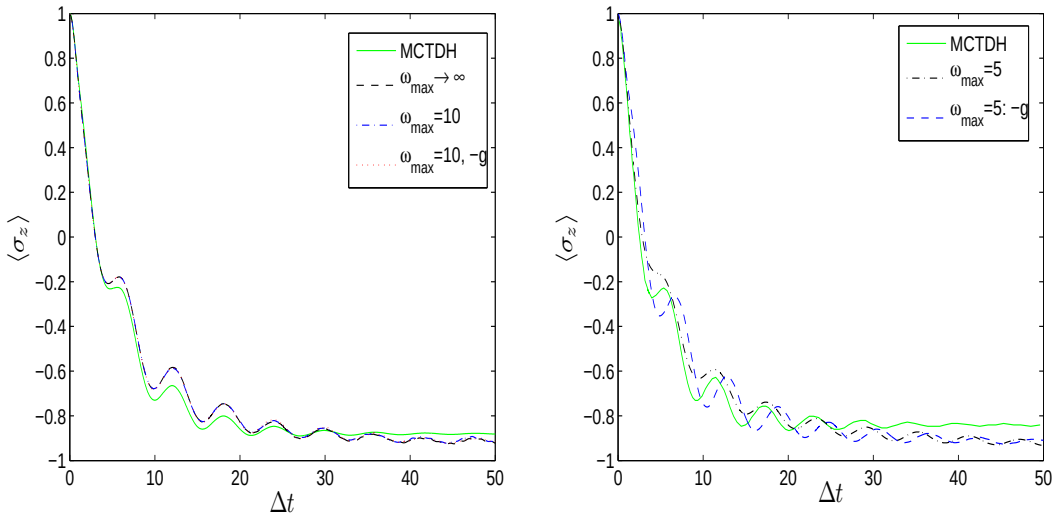

(a) Not-shifted bath

(b) Shifted-bath

Figure 5.4: The expectation value of $\langle\sigma_z\rangle$ versus rescaled time by MCE (w1 discretization) with $\Delta = 1$, $\epsilon = 1$, $\delta_s = 0.01$, $\omega_c = 1$ and $\beta = 10$, under different spin-bath interaction Hamiltonian phase and for different initial thermal bath: In (a) for initially canonical equilibrium thermal bath, MCE results are provided for $\omega_{max} \to \infty$ with g and phase flipping $-g$, and $\omega_{max} = 10$ with $-g$, by comparing with previous MCTDH result (green-solid); In (b) for initially displaced thermal bath, MCE results are provided for $\omega_{max} = 5$ with g and $-g$, by comparing with previous QUAPI result (green-solid).

5.3.4 Adjusting the coupling strength by a factor of 2

We now intend to test how sensitive the MCE approach is with respect to the *magnitude* of the coupling strengths, without ever shifting the initial bath state in phase space.

Reducing the coupling strength by a factor of 2

In Fig. 5.5a, it is clear that the results of $\omega_{max} \to \infty$ agree very well with those of $\omega_{max} = 5$ under different bath modes M and basis size N, despite of small

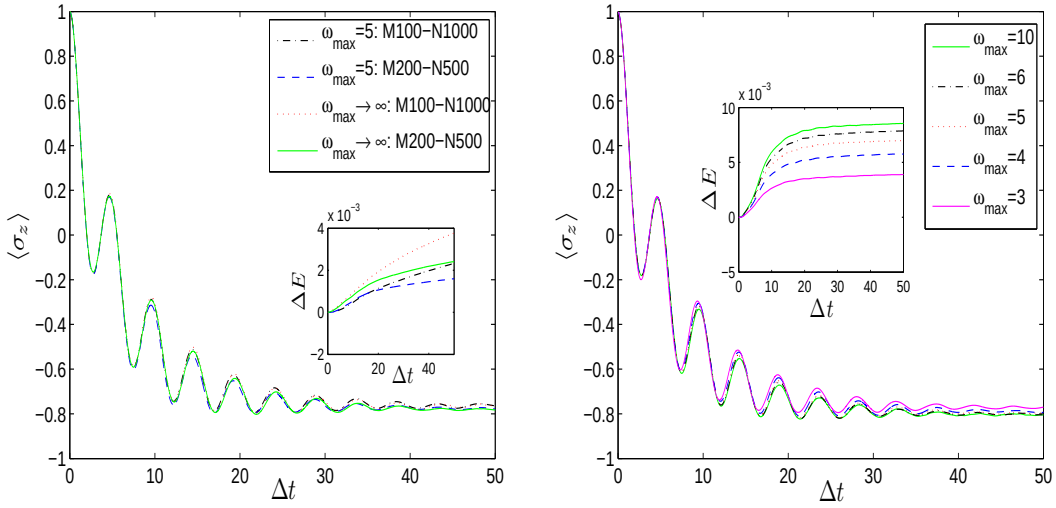

(a) $\omega_{max} \to \infty$ and $\omega_{max} = 5$ (b) Different ω_{max}

Figure 5.5: The expectation value of $\langle \sigma_z \rangle$ versus rescaled time by MCE (w1 discretization) with $\Delta = 1$, $\epsilon = 1$, $\delta_s = 0.01$, $\omega_c = 1$ and $\beta = 10$ for initially canonical equilibrium bath, but with reduced coupling strength $g/2$ (instead of g). In (a), different ω_{max} with different M, N and $comp$ ($comp = 500$ for $N = 1000$, $comp = 1000$ for $N = 500$); In (b), different ω_{max}, but with same $M = 100$, $N = 500$ and $comp = 150$. The insert figures are the corrsponding energy deviation $\Delta E(t)$ versus the rescaled time.

discrepancies. The insert figure display that, in both two different ω_{max} cases, energy deviation ΔE of $M = 200$ with $N = 500$ ($comp = 1000$) is more stable than that of $M = 100$ with $N = 1000$ ($comp = 500$).

In Fig. 5.5b, it is striking that, by fixing $M = 100$, $N = 500$, $comp = 150$, the results for different ω_{max}, ranging from 10 to 3, are very similar to each other and reach around the same $\langle \sigma_z \rangle$ at $\Delta t = 50$. The energy deviation ΔE holds almost flat after $\Delta t = 20$.

The reason to highlight the choice of ω_{max} is because it is very relevant for the whole system dynamics. If high frequencies do not play an important role, like here in the relatively small coupling strength $g/2$ case (Recall that the difference

in the case of g between $\omega_{max} \to \infty$ and $\omega_{max} = 5$ is already less pronounced in Fig. 5.1, Fig. 5.2 and Fig. 5.3.), one can set it to be fairly small. This will enable one to save computational cost, in the sense that much less bath modes will be required to fully display the whole system dynamics. We will address this issue further in the following section by increasing the coupling strength by a factor of 2.

Obviously, reduced coupling strengths allows one to obtain quickly converged results. Also, it can be clearly inferred that the Ehrenfest approximation adopted for MCE works very well with relatively small coupling strengths between spin and bath. This happens because the derivative of the basis coherent states are then relatively small even in full variational treatments, and hence the approximations introduced in their dynamics by using the Ehrenfest equations are definitely negligible.

Increasing the coupling strength by a factor of 2

If the coupling strengths are increased by a mere factor 2, the internal consistency of our method is lost, and we were not capable of obtaining converged results.

In Fig. 5.6a it is shown that, although the population difference $\langle\sigma_z\rangle$ always degrades with a similar pattern, the discrepancy of $\langle\sigma_z\rangle$ between $\omega_{max} \to \infty$ and $\omega_{max} = 5$ is dramatic. In both cases, results for $M = 100$ with $N = 1000$ decrease much more quickly than those for $M = 200$ with $N = 500$. For the same M and N, the case of $\omega_{max} \to \infty$ displays a higher population difference than $\omega_{max} = 5$. Under the same adjustable parameters $M = 100$, $N = 500$, $comp = 150$, Fig. 5.6b also shows very clearly that a large ω_{max} makes for unduly larger $\langle\sigma_z\rangle$.

This demonstrates that the MCE approach faces increasing difficulties to get converged results in the large coupling strength case: we have probably hit the region of parameters where the method stops being reliable, due to limitations inherent in our approach.

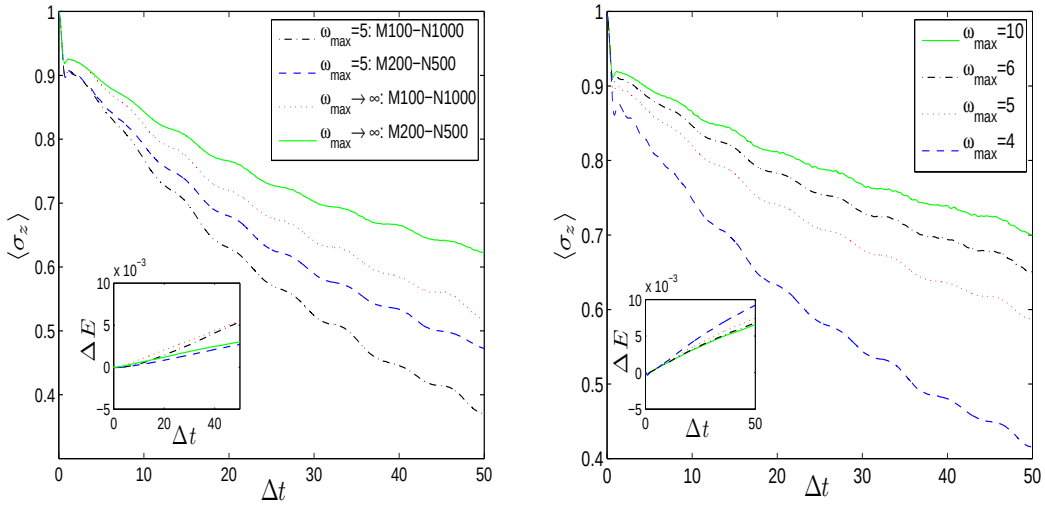

(a) $\omega_{max} \to \infty$ and $\omega_{max} = 5$ (b) Different ω_{max}

Figure 5.6: The expectation value of $\langle \sigma_z \rangle$ versus rescaled time by MCE (w1 discretization) with $\Delta = 1$, $\epsilon = 1$, $\delta_s = 0.01$, $\omega_c = 1$ and $\beta = 10$ for initially canonical equilibrium bath, but with increased coupling strength $2g$ (instead of g). In (a), different ω_{max} with different M, N and *comp* (*comp* $= 500$ for $N = 1000$, *comp* $= 1000$ for $N = 500$); In (b), different ω_{max}, but with same $M = 100$, $N = 500$ and *comp* $= 150$. The insert figures are the corrsponding energy deviation $\Delta E(t)$ versus the rescaled time.

We now attempt at identifying the possible reasons for this shortfall:

- *Bath discretization.*

  The key to a good bath discretization is to capture all the most important dynamical bath frequencies with a good coupling profile. Such frequencies are typically those close to the spin's resonance frequency (the energy gap between excited and ground state in the bare spin dynamics, $\sqrt{2}$ in our case). Increasing the coupling strengths typically increases the frequencies of the discretized bath and concentrates more frequencies away from the important region, such that the numerics are more sensitive to the total number of modes M. The maximum frequency ω_{max} is also very difficult

to set in order to get converged results for higher coupling strengths.

As one sees from Fig. 5.6, the MCE approach faces difficulty to get converged results for relatively strong coupling strengths. However, as evidenced in the other figures in this chapter, the results for $\omega_{max} = 5$ is close to $\omega_{max} \to \infty$. The reason is because the energy gap in the bare spin dynamics is only $\sqrt{2}$, and thus frequencies highly off it do not contribute as much as the low frequencies (close to $\sqrt{2}$). Hence, one important information revealed is that, if one is capable to distinguish the important frequencies, which plays the most important role in the whole dynamics, from a broad range of frequency distribution, much less coherent basis states are then required to display the whole quantum dynamics and thus will essentially save the computational resources. For instance, even in the case of $2g$ considered here, if there is a benchmark to compare or enough knowledge about the true system evolution, it will help one to determine a relatively small but reasonable ω_{max}, in order to reduce the total number of the discretized bath modes and therefore to minimize the coherent basis states to interpret the whole dynamics faithfully.

- *Size of the grid of coherent states.*

  To study stronger spin-bath interactions, a larger size of the coherent states grid N may be needed. First of all, clearly, a larger number of bath modes M (which may be necessary as per the previous point) demands a larger size of the coherent grid N. Further, even fixing ω_{max} and M, increasing coupling strength might require larger N. Setting $\omega_{max} = 5$ and $M = 100$, the difference between $N = 500$ and $N = 1000$ is still considerable. This is probably due to the fact that a larger portion of Hilbert space is spanned at equal times if the interaction strength is increased.

- *Time step.*

  The continuous dynamics is reproduced by a standard fourth-order Runge-Kutta method, where the accumulated error should be of fourth order in

the discrete time step. Even if such a method is rather reliable and allows for converged results, the time step dt for the numerical simulation should be sensisitive to the highest dynamical frequencies, which are pushed higher by increasing the coupling strengths. However, in our case, even reducing dt by a factor of 2 did not help us to achieve more easily converged results.

- *Ehrenfest approximation.*

  As detailed in Chapter 2, in obtaining the simplified working Eq. (3.40) for the coherent basis states, some components in the full variational Eq. (A.8) for the coherent basis states have been neglected, under the assumption that the overlap between two different coherent basis states becomes smaller as the evolution time goes by. This is likely to affect the accuracy of the MCE method to a certain extent, depending on the model. Typically, we find that this approximation is reliable unless the dynamics of the coherent states in phase space is too fast. Increasing the speed of such a dynamics is precisely what increased coupling strengths do, thus probably incurring in larger errors.

- *Smooth actions.*

  The classical action $S_{l,j}$ is introduced in Eq. 3.34, in order to obtain pre-exponential smooth amplitudes in Eq. (3.35). Such actions do greatly depend on the coupling strengths g_j, in that higher dynamical frequencies would imply quicker oscillations. The smoothening of the effective coherent amplitudes by the classical actions may become less effective when interaction strengths are increased.

5.4 Discussion

We have reported on a vast amount of simulation on the spin-boson model with super-Ohmic spectral density, which was carried out by systematically adjusting all the involved numerical parameters: the maximal frequency ω_{max} in the bath,

number of bath modes M, the size of coherent states' grid N, and the compression number *comp*, under three different discretization recipes. The results showed here are highly sensitive to such parameters in that, compared for instance to the Ohmic spin-boson case, super-Ohmic spin-boson numerics are much more difficult to converge in terms, typically, of the number of basis states.

Nevertheless, our MCE results are in very good agreement with MCTDH, indicating that the Ehrenfest approximation is rather reliable in the region of parameters considered, and apt to study bath's memory effects.

Our results are also relatively close with QUAPI numerics, although with some discrepancies. Without a systematic comparative analysis for a wider range of parameters, it is difficult to pin down these differences to specific reasons. It would be worth to get in touch with the authors of [NPTG07] to discuss specific advantages and limitations of the QUAPI approach, and compare them with our study.

In a near future, it would also be worth to compare MCE with another promising approach to spin boson dynamics based on density matrix renormalisation group techniques [PCHP10].

Comparative arguments aside, let us here summarise the regimes within which we could establish the Ehrenfest dynamics to follow the quantum dynamics reliably, and hence the range of applicability and scope of the method.

5.4.1 Working conditions

Firstly, let us mention that super-Ohmic baths turned out to be considerably more challenging than Ohmic ones. For instance, the Ohmic case of Fig.(8) of [NPTG07], with a cutoff frequency $\omega_c = 50$, can be reproduced with a relative precision of 10^{-3} with modest resources (around 200 basis states). We argue this to be due to the smoother form of the spectral density, which is easier to capture with our discretization.

Essentially, the super-Ohmic case becomes unstable, and unreliable, for high bath frequencies and strong spin-boson couplings: these are currently the main limitations to the method we employed.

For instance, if the cutoff frequency ω_c is too large, like $\omega_c = 200$ in Fig.(13) of [NPTG07], the MCE approach fails to produce the oscillations for $\langle\sigma_z\rangle$ within our current computational resources. The reason is that the coupling strengths of such broadband spectra stay strong when using a limited number of discretized modes to simulate the continuous bath.

Even for discrete sets of bosonic modes, as illustrated by Fig. 4.6 of chapter 4 (see also Figs. C.6 and C.7 in Appendix C), the coupling strength has to be reduced in order to get converged results. In the super-Ohmic case, a good rule of thumb is that covered results may be obtained for coupling strengths up to $1/\sqrt{2}$, in units of the bare resonance frequency of the spin.

Temperature is clearly another concern. Our treatment, based on Monte Carlo averaging, could be pushed up to temperatures of about 1, in units of bare resonance frequency of the spin. We could not have obtained a converged average for higher order of magnitude of the temperature.

5.4.2 The scope of the MCE method

As demonstrated in the last two chapters, the MCE method could be utilized as a useful tool to study systems where few two-level qubits (or low dimensional subsystems) interact with a relatively large number of bosonic degrees of freedoms. The methodology is that low dimensional subsystems are treated in a complete and static Hilbert vector space, while bosonic modes are described in an incomplete and dynamical Hilbert space, constructed from a set of propagating coupled coherent states guided by Ehrenfest dynamics. Therefore, the MCE approach, in principle, can be applied to very diverse physical systems sharing similar descriptions involving bosonic modes, either spin-bosonic or purely bosonic. This

versatility is probably the main strength of the method, which hence begs to be applied in wider contexts than what done so far.

The work presented here will be the basis on which further investigation will be built. A first obvious direction we intend to pursue is a rigorous study of the memory effects of the bath (as quantified by the fluctuations of the bath's, or system's, entropy) in the super-Ohmic regime. Then, we should also proceed to a full, systematic study of the spin-boson model, ranging from sub-Ohmic to super-Ohmic regimes and looking for various relevant dynamical features (*e.g.*, localization), based on a single consistent numerical technique.

We have however already contributed to establish MCE as a numerical method to study complex spin-boson dynamics, with performance comparable to competing approaches, and which could be valuable for the investigation of quantum dynamics of interest in quantum optics, chemical physics and solid state physics.

Chapter 6

General error bound for approximated unitary quantum dynamics

6.1 Motivation

As we pointed out several times before in this dissertation, the study of generic quantum dynamics is doomed to approximation since, even when the evolution of the system can reasonably be considered as unitary, and the corresponding Hamiltonian as known, the dimension of the Hilbert space where the evolution takes place is generally intractable on computing machines. One has then to use approximated methods, like MCE in our case, which come in many flavours and are adapted to many different tasks. With all this variety and diversity, it would be extremely desirable to have systematic ways to estimate the errors made while trying to calculate the evolving quantum state and, perhaps even more importantly, to quantitatively compare different approaches to the same problem. While error analyses have been carried out in specific contexts (see, for instance [Lub08]), no established general framework has been developed for the analysis of numerical errors, at least to our knowledge.

Now, quite simply, most of the numerical approaches currently available rely on the state of the system at any given time to be represented in a restricted Hilbert space, such that it can be stored on a computer's hard disk. Inspired by this obvious remark, we shall proceed to determine how the upper bound on the geometric ('Euclidean') distance between the 'true' vector state of the system, $|\psi\rangle$, and the approximated vector space stored on the computer's hard disk, $|\psi'\rangle$, also referred to as the 'hard disk state' in what follows, can be updated at every time-step of unitary evolution under a Hamiltonian $\hat{H}$.

6.2 Derivation of the bound

Suppose that, at time t, one has

$$\| |\psi(t)\rangle - |\psi'(t)\rangle \|_2 \leq \delta(t) \ , \tag{6.1}$$

where $\| |v\rangle \|_2 = \sqrt{\langle v \, | v \rangle}$ is the 2-norm of the vector, and that the system's true state $|\psi(t)\rangle$ evolves under the known time-independent Hamiltonian $\hat{H}$:

$$\partial_t |\psi(t)\rangle = -i\hat{H}|\psi(t)\rangle \ . \tag{6.2}$$

Our first aim is determining the distance $\| |\psi(t + \mathrm{d}t)\rangle - |\psi'(t + \mathrm{d}t)\rangle \|_2$, at first order in $\mathrm{d}t$.

To this purpose, let us introduce the operator P_t, representing the orthogonal projector on the restricted Hilbert space of the hard disk (the label t is included to stress that such a projector might depend on time, as is the case in most sophisticated numerical techniques, where the adopted 'basis' does depend on time). One has, clearly, $P_t^2 = P_t$, and $P_t|\psi'(t)\rangle = |\psi'(t)\rangle$. We will also use the expression $\hat{H}' = P_t \hat{H} P_t$: the operator $\hat{H}'$ is nothing but the Hamiltonian stored (or computable) in the hard disk as a matrix of complex numbers.

Schrödinger's equation for the hard disk state reads

$$P_t \partial_t |\psi'(t)\rangle = -iP_t\hat{H}|\psi'(t)\rangle = -i\hat{H}'|\psi'(t)\rangle \ . \tag{6.3}$$

It is crucial here to note that, in general, $P_t\partial_t|\psi'(t)\rangle \neq \partial_t|\psi'(t)\rangle$: the time-derivative operator as well, and not only the Hamiltonian, might not be exactly representable on the hard disk Hilbert space. We will see in the following an instance where this is the case, and show explicitly how the contribution of the time-derivative to the error bar can be taken into account.

It should also be remarked that, in the following, we will assume that the approximated dynamics will be wholly governed by the projected Schrödinger Eq. (6.3) alone, without any step by step normalisation of the state vector. Several numerical methods, among which MCE, work on this assumption (and actually rely on evaluating the norm as an indicator of the quality of the simulation). The framework we are introducing can be adapted to include forced normalisation, at the price of some added complexity.

At first order one has

$$\||\psi(t+\mathrm{d}t)\rangle - |\psi'(t+\mathrm{d}t)\rangle\|_2 \leq \||\psi(t)\rangle - |\psi'(t)\rangle\|_2 + \|\partial_t|\psi(t)\rangle - \partial_t|\psi'(t)\rangle\|_2\mathrm{d}t + \mathrm{o}(\mathrm{d}t), \tag{6.4}$$

which can be further decomposed by repeated application of the triangular inequality and of the Schrödinger equations reported above, to obtain:

$$\begin{aligned}\||\psi(t+\mathrm{d}t)\rangle - |\psi'(t+\mathrm{d}t)\rangle\|_2 \leq \delta(t) &+ \|\partial_t|\psi'(t)\rangle - P_t\partial_t|\psi'(t)\rangle\|_2\mathrm{d}t \\ &+ \|\hat{H}|\psi(t)\rangle - P_t\hat{H}|\psi'(t)\rangle\|_2\mathrm{d}t + \mathrm{o}(\mathrm{d}t).\end{aligned} \tag{6.5}$$

The notation $\mathrm{o}(\mathrm{d}t)$ stands for Landau little-o symbol: $\lim_{\mathrm{d}t\to 0}\mathrm{o}(\mathrm{d}t)/\mathrm{d}t = 0$.

The two coefficients for the updated error at first order in $\mathrm{d}t$ can be re-expressed in terms of overlaps. The first coefficient, which we will call $\kappa(t)$, quantifies the error due to the impossibility of representing the time-derivative exactly in the whole Hilbert space, and is given by:

$$\kappa(t) = \|\partial_t|\psi'(t)\rangle - P_t\partial_t|\psi'(t)\rangle\|_2 = \sqrt{\langle\psi'(t)\,|\partial_t(P_t - \mathbb{1})\partial_t|\psi'(t)\rangle}\,, \tag{6.6}$$

where $\mathbb{1}$ stands for the identity operator on the whole Hilbert space. Notice that ∂_t can be understood to always act on the right and that $\kappa(t) \geq 0$. The evaluation of $\kappa(t)$ for the MCE method on a phase-space grid may be found in Appendix E.

The second coefficient accounts for the imperfect representation of the Hamiltonian $\hat{H}$ in the hard disk Hilbert space and can be recast as

$$\begin{aligned} &\|\hat{H}|\psi(t)\rangle - P_t\hat{H}|\psi'(t)\rangle\|_2 \\ &= \sqrt{\langle\psi(t)\,|\hat{H}^2|\psi(t)\rangle + \langle\psi'(t)\,|\hat{H'}^2|\psi'(t)\rangle - (\langle\psi(t)\,|\hat{H}P_t\hat{H}|\psi'(t)\rangle + \text{c.c.})}\,. \end{aligned} \tag{6.7}$$

In the last expression, the first term is just the expectation value of the squared Hamiltonian $\langle\hat{H}^2\rangle$, which is conserved, and can be very often exactly computed from the initial conditions of the system. The second term, $\langle\psi'(t)\,|\hat{H'}^2|\psi'(t)\rangle$ only depends on the hard disk state and Hamiltonian, and can hence also be exactly computed at any given time (it won't necessarily be a constant, since $\hat{H}' = P_t\hat{H}P_t$ generally depends on time). The last term can also be evaluated, as follows. First, notice that Eq. (6.1) implies

$$|\psi(t)\rangle = |\psi'(t)\rangle + \varepsilon|v\rangle\,, \quad \text{where} \quad \||v\rangle\|_2 = 1 \quad \text{and} \quad \varepsilon \leq \delta(t)\,, \tag{6.8}$$

which can be substituted for $|\psi(t)\rangle$ in $(\langle\psi(t)\,|\hat{H}P_t\hat{H}|\psi'(t)\rangle + \text{c.c.})$ to get

$$\begin{aligned} -(\langle\psi(t)\,|\hat{H}P_t\hat{H}|\psi'(t)\rangle + \text{c.c.}) &= -(\langle\psi'(t)\,|\hat{H}'^2|\psi'(t)\rangle + \varepsilon\langle v\,|\hat{H}P_t\hat{H}|\psi'(t)\rangle + \text{c.c.}) \\ &\leq -2\langle\psi'(t)\,|\hat{H}'^2|\psi'(t)\rangle + 2\delta(t)\|\hat{H}\hat{H}'|\psi'(t)\rangle\|_2\,. \end{aligned} \tag{6.9}$$

This inequality can be combined with Eq. (6.7), obtaining

$$\|\hat{H}|\psi(t)\rangle - P_t\hat{H}|\psi'(t)\rangle\|_2 \leq \sqrt{\langle\hat{H}^2\rangle - \langle\psi'(t)\,|\hat{H}'^2|\psi'(t)\rangle + 2\delta(t)\|\hat{H}\hat{H}'|\psi'(t)\rangle\|_2}\,. \tag{6.10}$$

The definitions:

$$\eta(t) = \langle\hat{H}^2\rangle - \langle\psi'(t)\,|\hat{H}'^2|\psi'(t)\rangle\,, \tag{6.11}$$

$$\xi(t) = 2\|\hat{H}\hat{H}'|\psi'(t)\rangle\|_2 = 2\sqrt{\langle\psi'(t)\,|\hat{H}'\hat{H}^2\hat{H}'|\psi'(t)\rangle} \tag{6.12}$$

lead to

$$\|\hat{H}|\psi(t)\rangle - P_t\hat{H}|\psi'(t)\rangle\|_2 \leq \sqrt{\eta(t) + \delta(t)\xi(t)}\,. \tag{6.13}$$

Note that the expression $\langle\psi'(t)\,|\hat{H}'\hat{H}^2\hat{H}'|\psi'(t)\rangle$ can be rewritten as $\langle\psi'(t)\,|\hat{H}'\hat{H}^{2\prime}\hat{H}'|\psi'(t)\rangle$, where we have defined $\hat{H}^{2\prime} = P_t\hat{H}^2P_t$. The coefficient $\xi(t)$

is hence computable as long as the matrix elements of both $\hat{H}'$ and $\hat{H}^{2\prime}$ can be evaluated in the 'hard-disk basis'. This is a very weak requirement, satisfied by most numerical techniques, including MCE.

As apparent, $\eta(t)$ represents the contribution to the error at first order in time due to the discrepancy between the exact invariant $\langle \hat{H}^2 \rangle$ and the quantity $\langle \psi'(t) | \hat{H}'^2 | \psi'(t) \rangle$ stored in the hard disk. While $\eta(t)$ can generally be negative, the term within square root on the RHS of Inequality (6.10) is always positive. Note also that, in natural units, $\kappa(t)$ has the dimension of an inverse time whereas $\eta(t)$ and $\xi(t)$ have the dimension of an inverse time squared.

The term $\delta(t)\xi(t)$ is instead due to the imperfect knowledge of the quantum state at time t. It should be stressed that, since no knowledge whatsoever about the vector $|v\rangle$ of Eq. (6.8) can be assumed, this is the best possible geometric bound achievable within our framework.

Before proceeding, let us summarise and re-organise our findings in a handier form, by inserting (6.6), (6.10) and (6.13) into Inequality (6.5):

$$\| |\psi(t+\mathrm{d}t)\rangle - |\psi'(t+\mathrm{d}t)\rangle \|_2 \leq \delta(t) + \kappa(t)dt + \sqrt{\eta(t) + \xi(t)\delta(t)}\mathrm{d}t + \mathrm{o}(\mathrm{d}t) = \delta(t+\mathrm{d}t) \tag{6.14}$$

(According to Ineq. (6.1), we have equated the error bound determined at time $t + \mathrm{d}t$ with $\delta(t + \mathrm{d}t)$). By taking the limit $\mathrm{d}t \to 0$ in the last equality, we obtain a differential equation for the geometric error bound $\delta(t)$:

$$\frac{\mathrm{d}\delta}{\mathrm{d}t} = \kappa(t) + \sqrt{\eta(t) + \xi(t)\delta(t)} \; . \tag{6.15}$$

This is the central finding of our analysis: since the quantities $\kappa(t)$, $\eta(t)$ and $\xi(t)$ can all be evaluated as the numerics progress, the first-order differential equation (6.15) can be always be numerically integrated, and its solution provides a rigorous upper bound to the geometric distance between the true state $|\psi\rangle$ and the hard disk state $|\psi'\rangle$.

Notice that our result, in the form of Eq. (6.15) is completely independent on the technicalities involved in the numerical solution of the dynamical equations (as

long as they provide a solution of Schrödinger equation with no error at first order in dt, like the fourth order Runge-Kutta method we employ does), and on the discretisation of time adopted. The reliability of a numerically determined $\delta(t)$ would just be heralded by convergence with respect to a decrease in the numerics' time-step.

6.2.1 Optimization with respect to ground energy

It is important to remark that, while the dynamical equations and the the numerics are all obviously invariant under the transformation $\hat{H} \to \hat{H} + E_0$, where E_0 is a real additive constant, the quantities $\eta(t)$ and $\xi(t)$ are not. This fact is not logically inconsistent, as it follows from the geometric nature of our bound, and can actually be exploited to properly reduce the value of the time derivative of $\delta(t)$, thus keeping the error as low as possible, at least at short times. Let the functions $\eta(t, E_0)$ and $\xi(t, E_0)$ denote the counterparts of $\eta(t)$ and $\xi(t)$ if an additive constant E_0 is added to $\hat{H}$. Such functions read

$$\eta(t, E_0) = \langle \hat{H}^2 \rangle - \langle \psi'(t) | \hat{H'}^2 | \psi'(t) \rangle - 2E_0(\langle \hat{H} \rangle + \langle \psi'(t) | \hat{H'} | \psi'(t) \rangle), \tag{6.16}$$

$$\begin{aligned} \frac{\xi^2(t, E_0)}{2} =& E_0^4 - 4\langle \psi'(t) | \hat{H'} | \psi'(t) \rangle E_0^3 \langle \psi'(t) | \hat{H'} \hat{H}^{2'} \hat{H'} | \psi'(t) \rangle \\ &+ (5\langle \psi'(t) | \hat{H'}^2 | \psi'(t) \rangle + \langle \psi'(t) | \hat{H}^{2'} | \psi'(t) \rangle) E_0^2 \\ &- (2\langle \psi'(t) | \hat{H'}^3 | \psi'(t) \rangle + \langle \psi'(t) | \hat{H}^{2'} \hat{H'} + \hat{H'} \hat{H}^{2'} | \psi'(t) \rangle) E_0. \end{aligned} \tag{6.17}$$

Each pairs of functions $\eta(t, E_0)$, $\xi(t, E_0)$ for given E_0 provides one with a different error bound. The optimal value E_0, minimising the quantity $\delta(t)$ at relevant times, clearly depends on the specific properties of Hamiltonian and numerical method. Still, it would seem natural to take advantage of the freedom on the choice of E_0 to minimise the quantity $\xi(0, E_0)$, at time $t = 0$.

6.3 Error bound estimates

In the previous section, we obtained a differential equation for a certifiable error bound δ, of the form:

$$\dot{\delta} = \kappa(t) + \sqrt{\eta(t, E_0) + \xi(t, E_0)\delta}\,, \tag{6.18}$$

where we have kept the zero point of the energy E_0 as a free variable.

An analytic solution for $\delta(t)$ is not easy to obtain, and would anyway depend on the functions $\kappa(t)$, $\eta(t, E_0)$ and $\xi(t, E_0)$, which generally depends on the techniques and system under examination. Still, it is very instructive to consider the solution for $\delta(t)$ by replacing such functions with constant values, which shall be denoted by κ, η and ξ. In fact, although $\kappa(t)$, $\eta(t, E_0)$ and $\xi(t, E_0)$ will of course fluctuate and vary in time in very complicated fashions, in practical cases their typical values will not deviate too noticeably from their initial values, at least on the relatively short time-scale we are interested in (once the error bound grows too large, the present analysis cannot lend any substance to the numerics' validity anyway). Hence, the solutions for $\delta(t)$ at constant coefficients will provide one with an insightful guideline on the error bound's behaviour.

We will also assume, for simplicity, the initial condition $\delta(0) = 0$ (very reasonable, as the initial state can often be represented exactly). The solution to Eq. (6.18) can then be given in terms of the solution of the following transcendent equation:

$$\sqrt{\frac{\eta}{\xi} + \delta(t)} - \frac{\kappa}{\sqrt{\xi}} \ln\left(1 + \frac{\sqrt{\xi}}{\kappa}\sqrt{\frac{\eta}{\xi} + \delta(t)}\right) = \frac{\sqrt{\xi}}{2}t + \sqrt{\frac{\eta}{\xi}} - \frac{\kappa}{\sqrt{\xi}} \ln\left(1 + \frac{\sqrt{\eta}}{\kappa}\right) \tag{6.19}$$

Preliminary studies show that, in practical cases, the solution $\delta(t)$, always a convex increasing function, where $\kappa(t)$, $\eta(t)$ and $\xi(t)$ are replaced with their initial values typically yields a very reliable estimate for the numerically computed bounds.

We can now push this heuristic arguments a bit further and inquire about the different roles played of the coefficients κ, η and ξ. If ξ dominates the equation

(*i.e.* for $\kappa^2 \ll \xi$ and $\eta \ll \xi$), then one has:

$$\delta(t) \simeq \frac{\xi}{4} t^2 \ . \tag{6.20}$$

Hence, in this case the time-scale on which the numerics are provably reliable is simply given by $1/\sqrt{\xi}$: after a time $t \simeq 1/\sqrt{\xi}$, the error bounds reaches the value 0.25 which, in the great majority of interesting (large and complex) systems, implies that very little can be rigorously inferred from the numerics about the true value of measurable quantities.

An increasing quadratic behaviour, due to the dominance of the term $\sqrt{\xi\delta(t)}$ in the differential equation, is always bound to kick in at long enough times. this is however not always relevant to our study in that one should remember that the Euclidean distance between two vector of unit norm is bound from above by 2. Values of δ above 2 are hence nonsensical.

At short times, on the other hand, and more precisely for $\sqrt{\xi}t \ll 1$, the term $\xi\delta(t)$ can be neglected, and the error accrues linearly in time:

$$\delta(t) \simeq (\kappa + \sqrt{\eta})\, t \quad \text{for} \quad \sqrt{\xi}t \ll 1 \ . \tag{6.21}$$

In practice, our approximated analysis shows that it is desirable to keep $\sqrt{\xi}$ as low as possible, so as to hold off the onset of the quadratic regime, where our error bound rapidly blows up.

6.4 A brief comment on applications

We could not yet extensively test the bound on our numerics, because these results were derived very recently. However, by a first inspection of standard Ohmic spin-boson models by MCE (see Appendix E for an evaluation of the coefficient $\kappa(t)$ specific to the MCE on coupled coherent states case), it is clear that the term $\delta(t)\xi(t)$ plays the dominant role in the error bound and, as anticipated, one has error bounds comparable to the solution $\delta(t)$ of Eq. (6.19). Such error bounds, unfortunately, become very large at very short times, well before our numerics

become unreliable (as known, for instance, from analytical solutions of simple dynamics).

This is not all that surprising: it is clear that the coefficient $\xi(t)$ is the real Achille's heel of our analytical treatment. In fact, $\kappa(t)$ and $\eta(t)$ depend on differences between expectation values of 'true' Hilbert space operators and 'hard-disk estimates' and do strongly depend on the quality of the numerical technique and, for given technique, decrease with increasing resources (for instance, trivially, if more basis states are used). Instead, $\xi(t)$ is fixed number depending on some expectation value of a hard-disk operator ($H'H^{2\prime}H'$), whose magnitude does not depend on the quality of the simulation.

However, this problem also inspires us to conjecture the existence of a 'heuristic', stricter error bound. The quantity ξ was introduced in Eq. (6.9), where the overlap between a certain known vector of finite norm ($\hat{H}\hat{H}'|\psi'\rangle$) and the *completely unknown* vector of unit norm $|v\rangle$ has been bound from above by the norm of the known vector. But, in Hilbert space of large dimension, this is an extremely pessimistic bound! Statistically (in the sense, for instance, of the Haar measure, see Chapter 2), the average overlap between any two generic vectors of finite norm goes to zero with increasing dimension of the Hilbert space. Since Hilbert spaces of infinite dimension are what we are interested in, one could neglect the $\xi(t)$ term altogether, replace $\eta(t)$ with $|\eta(t)|$, and end up with an easily computable error bound $\delta(t)$ which would just linearly increase in time as:

$$\delta(t) = \int_0^t \left(\kappa(t) + \sqrt{|\eta(t)|}\right) \mathrm{d}t + \delta(0) \; . \tag{6.22}$$

As a first step, we intend to test this heuristic bound on our MCE numerics, starting from well known situations.

We hope this might in time prove useful to establish a common set of guidelines to compare different numerical techniques.

Chapter 7

Conclusions and Outlook

Coherence is the fundamental aspect of quantum theory producing both its intriguing features and its potential for applications [MAN00, LJL+10, GRTZ02, ECR+07, LCF07]. The coherence of quantum subsystems is however very sensitive to interactions, both within well identified systems and with surrounding environments. This thesis is an attempt at developing and testing methods to disclose the emergence of quantum coherence in complex quantum systems.

In chapter 2, high fidelity Controlled-Z gates between two remote qubits, linked by dispersive bosonic modes, were shown to be achievable by employing a specific way to encode quantum information to confine the whole system in one excitation only Hilbert space. This feature saves the computation cost and also reduces the disspation inducing by excitation states. The study reveals that relatively large number of mediating modes may work co-operatively to perserve the quantum coherence.

In chapter 3, the 'Multi-Configurational Ehrenfest' (MCE) is introduced to truncate the infinite continuum bath modes, by utilizing time-dependent and Gaussian-distributed coherent states as a basis followed by Ehrenfest guided dynamics. In chapter 4 and chapter 5, the self-consistent convergence and agreement with another two numerical approaches 'multi-configurational time-dependent Hartree' (MCTDH) and 'Quasi-adiabatic path integrals' (QUAPI) evidence the

capability of MCE as a numerical tool to study complex and large quantum systems. However, The discrepancies between different numerical scenario (either relatively small or distinct), evokes the idea in chapter 6 to determine an error bound to qualify the reliablity of computed state of system in computer hard disk. Rigorous formulisam has been layed out as a starting point to carry out the upper gemometic error bound, though no supported evidence is given to track down the efficiency of this approach.

For the last three years, my co-workers[1] and I have faced, and for the most part sorted, a number of minor and major technical problems related to the application of Ehrenfest guided trajectories to the study of quantum dynamics. The solution of such technicalities, and the insight into the related physics such an exercise has given us, have left us with a powerful, and relatively well understood, tool to deal with quantum dynamics involving bosonic degrees of freedom. I am confident these methods can be the foundation of substantial future work.

The MCE method can in fact be applied to study coherent effects in the most diverse systems where qubits interact with a boson bath: in trapped ions, the internal levels may embody discrete spins, while the vibrational normal modes constitute a finite phonon bath which, by adjusting laser beams onto a single ion and the ion crystal's dimensions, can mimic spectral densities ranging from sub-Ohmic to super-Ohmic [PMvDC08]; in semiconductors, excitons and phonons admit a natural spin-boson descrtiption within a solid state environment [RGG$^+$10, RGB$^+$10]; in light-harvesting antennae, where localised dimers interact with the light field, spin-boson modelling plays a major role. In the latter setting, non-Markovian and non-perturbative effects become significant and thus challenging to solve by semi-analytic methods, mainly due to the following specific reasons: (i) the time scale of the protein-solvent bath (typically relevant to the cutoff frequency) is comparable to (or even slower than) that of exciton

[1] Primarily my supervisor, Dr. Alessio Serafini, and Dr. Dmitrii Shalashilin, who pioneered the MCE method, and without whose help most of this research would not have been possible.

dynamics [TER+09]; (ii) the coupling strength between the system and bath is strong when compared with the intra-system coherent coupling rates [HP11]. In all these physical systems, the MCE approach may be utilized to study the interplay between system and bath and thus possibly identify regimes where the system's coherence is preserved for longer times, where non-Markovian effects are dominant, or where localisation and de-localization occur under various physics conditions, including finite temperatures and different bath spectral densities. The main limitations to this programme we can foresee are related to the difficulties in treating broad spectral densities and very strong spin-boson couplings, illustrated in chapter 5. We can still be very confident our techniques will provide one with results which are well beyond the reach of conventional, semi-analytic approaches and, as previously remarked, which are applicable over a wide set of parameters and systems.

Very importantly, MCE could also be convenient employed for purely bosonic systems – like optomechanical or all-optical systems – with anharmonic Hamiltonians (higher than quadratic in order, and thus not analytically solvable). In particular, for instance, our method, where the wave-function is represented on a grid of coherent states, would be especially well suited to simulate the generation of Schrödinger cats of coherent states [SMW07], or entangled coherent states [San92] in non-linear crystals.

Finally, in the general context of the numerical approximation of quantum dynamics, it would be worth to carry out more stringent comparative analysis not only with path integral techniques but also with spin-boson adapted t-DMRG methods [CHP11], as discussed in Chapter 5. It would also be worth investigating whether the analytical transformation (1D chain mapping) of arbitrary and possibly highly structured baths used in such an approach, could be borrowed to overcome the sensitivity of the MCE method with respect to the various discretization recipes for the bath. Furthermore, the comparison with t-DMRG is particularly interesting, because the error analysis presented in Chapter 6 would

apply quite directly to such numerics as well (where error bounds can be quantified in terms of 'truncation errors'), and could serve as a quantitative guideline to compare the two techniques.

In this dissertation, we demonstrated not only the advantages, but also the limitations of the MCE method. As shown in Chapters 4 and 5 and noted above, MCE faces difficulties to get convergence as the spin-boson coupling strength increases. We believe that part of the reason behind this shortfall is very likely the Ehrenfest approximation itself. Hence, it could be worth to program a full variational method, adopting full Euler-Lagrange equations not only for the expansion coefficients, but also for the coherent states of the basis grid (and possibly to compare it with MCE by our quantitative error analysis).

Appendices

Appendix A

Further notes on the MCE method

In this appendix, the detailed derivation of the working equations of the Multi-configurational coupled coherent states technique will be laid out, and other related technical details will be discussed. To pave the way to the understanding of the method, we take a model of spins interacting with a bath of bosonic modes as an example.

A.1 Wavefunction

A.1.1 Single-configuration

For clarity, let us first consider the single-configurational wavefunction. The wavefunction of the whole system is:

$$|\Psi(t)\rangle = \sum_{l=1}^{d} a_l(t)|\phi_l\rangle|\mathbf{Z}(t)\rangle \tag{A.1}$$

where the spin is expanded in the complete basis $|\phi_l\rangle$ with the total dimension d (for example, $d = 4$ for two spin), and the bath is represented as a tensor product

of M coherent states:

$$|\mathbf{Z}(t)\rangle = \bigotimes_{m=1}^{M} |z^m(t)\rangle \tag{A.2}$$

Here, m and M donates the m^{th} bath mode and total number of bath modes, respectively.

The quantum Lagrangian of Eq. (3.13) can be explicitly expressed as

$$\mathcal{L} = -\sum_{l,n=1}^{d} a_l^* a_n \langle \phi_l | H | \phi_n \rangle + i \sum_{l=1}^{d} a_l^* a_l + i \sum_{l=1}^{d} |a_l|^2 \left(\frac{\mathbf{Z}^* \dot{\mathbf{Z}} - \mathbf{Z}\dot{\mathbf{Z}}^*}{2}\right). \tag{A.3}$$

The variation of $\mathbf{Z}^*$ acting on the quantum Lagrangian yields

$$\frac{\partial \mathcal{L}}{\partial \mathbf{Z}^*} = -\sum_{l,n=1}^{d} a_l^* a_n \frac{\partial \langle \phi_l | H | \phi_n \rangle}{\partial \mathbf{Z}^*} + i \sum_{l=1}^{d} |a_l|^2 \frac{\dot{\mathbf{Z}}}{2}, \tag{A.4}$$

and

$$\frac{d}{dt}\left(\frac{\partial \mathcal{L}}{\partial \dot{\mathbf{Z}}^*}\right) = -i\frac{\mathbf{Z}}{2} \frac{d(\sum_{l=1}^{d} |a_l|^2)}{dt} - i \sum_{l=1}^{d} |a_l|^2 \frac{\dot{\mathbf{Z}}}{2}. \tag{A.5}$$

Then, assuming $\frac{d}{dt}(\sum_{l=1}^{d} |a_l|^2) = 0$ and defining an Eherenfest mean-field Hamiltonian as in [Bil83, MM79, KHS03]

$$\begin{aligned} H_{Ehr} &= \frac{\langle \Psi(t) | \hat{H} | \Psi(t) \rangle}{\langle \Psi(t) | \Psi(t) \rangle} \\ &= \frac{\sum_{l,n=1}^{d} a_l^* a_n \langle \mathbf{Z}, \phi_l | H | \phi_n, \mathbf{Z} \rangle}{\sum_{l=1}^{d} |a_l|^2}, \end{aligned} \tag{A.6}$$

one obtains the working equation for the coherent basis states

$$i\dot{\mathbf{Z}} = \frac{\partial H_{Ehr}}{\partial \mathbf{Z}^*}. \tag{A.7}$$

The original Eherenfest mean-field approximation is a semi-classical approach, based on the assumption that: (i) the whole system is divided into quantum subsystem with Hamiltonian operator $\hat{H}_{quant}$, a classical subsystem with classical Hamiltonan H_{class}, and with interaction Hamiltonian $\hat{H}_{int}$ between them; (ii) the motion of the classical trajectories (usually referring to the evolution of momenta and coordinates) is derived from the averaging of the Hamiltonian over the quantum subsytem. However, for the MCE approach, we will first treat all of the

variables at the quantum level and then make an approximation (which is similar to Ehrenfest mean-field thorem) to simplify the computational efforts.

Similarly to the cases of single-configuration and multi-configuration time-dependent self-consistent field (TDSCF), or Single- and Multi-configurational time dependent Hartree (MCTDH), as discussed in [MM87, MMC92], the single-configuration wavefunction is expected to reflect the dynamics poorly in most cases.

A.1.2 Multi-configurational equations

The Multi-configurational wavefunction has been introduced in Eq. (3.30) in Chapter 3. The corresponding working equations for the expansion coefficients $a_{l,j}$ has been derived as well. Here below, we apply the full variational principle on Eq. (3.31) in order to get the full variational working equations for the coherent basis states $\mathbf{Z}_j$. One shall then see why it is reasonable to make the Ehrenfest approximation for these trajectories.

Working equations for the trajectories

Applying the varational principle $\delta \int \mathcal{L} dt = 0$ to Eq. (3.31), leads to the Euler-Lagrange equations of motion for the coherent basis states. The variation of $\mathbf{Z}_i^*$

yields

$$\begin{aligned}
&\frac{\partial \mathcal{L}}{\partial \mathbf{Z}_i^*} - \frac{d}{dt}\frac{\partial \mathcal{L}}{\partial \dot{\mathbf{Z}}_i^*} \\
&= \sum_{l=1}^{d}\sum_{j=1}^{N}\{i a_{l,i}^* \dot{a}_{l,j}\Omega_{ij}(\mathbf{Z}_j - \frac{\mathbf{Z}_i}{2}) + i a_{l,i}^* a_{l,j}\Omega_{ij}\dot{\mathbf{Z}}_j \\
&+ i a_{l,i}^* a_{l,j}(\mathbf{Z}_i^*\dot{\mathbf{Z}}_j - \frac{\mathbf{Z}_j^*\dot{\mathbf{Z}}_j + \mathbf{Z}_j\dot{\mathbf{Z}}_j^*}{2})(\mathbf{Z}_j - \frac{\mathbf{Z}_i}{2})\Omega_{ij} \\
&- \sum_{n=1}^{d}[a_{l,i}^* a_{n,j}\frac{\partial\langle \mathbf{Z}_i, \phi_l|\hat{H}|\phi_n, \mathbf{Z}_j\rangle}{\partial \mathbf{Z}_i^*} \\
&+ a_{l,i}^* a_{n,j}\langle \mathbf{Z}_i, \phi_l|\hat{H}|\phi_n, \mathbf{Z}_j\rangle(\mathbf{Z}_j - \frac{\mathbf{Z}_i}{2})]\} \\
&- i\frac{\mathbf{Z}_i}{2}\frac{d}{dt}\sum_{l=1}^{d}|a_{l,i}|^2,
\end{aligned} \tag{A.8}$$

where the last term arises from the second component in Eq. (3.31) in the case of $j = i$. Aiming for a simplified working equation for the coherent basis states, we neglect the last term by setting $\frac{d}{dt}(\sum_{l=1}^{d}|a_{l,i}|^2) = 0$. Then all the terms involving $(\mathbf{Z}_j - \frac{\mathbf{Z}_i}{2})$ can be split into the two parts $(\mathbf{Z}_j - \mathbf{Z}_i)$ and $+\mathbf{Z}_i$. After employing Eq. (3.33) to cancel out all the terms containing $+\mathbf{Z}_i$, one arrives at

$$\begin{aligned}
&\sum_{l=1}^{d}\sum_{j=1}^{N}[a_{l,i}^* a_{l,j}\Omega_{ij}\dot{\mathbf{Z}}_j - \sum_{n=1}^{d}a_{l,i}^* a_{n,j}\frac{\partial\langle \mathbf{Z}_i, \phi_l|\hat{H}|\phi_n, \mathbf{Z}_j\rangle}{\partial \mathbf{Z}_i^*}] \\
&+ \sum_{l=1}^{d}a_{l,i}^*\sum_{j=1}^{N}\{(\mathbf{Z}_j - \mathbf{Z}_i)[i\dot{a}_{l,j}\Omega_{ij} + i a_{l,j}(\mathbf{Z}_i^*\dot{\mathbf{Z}}_j - \frac{\mathbf{Z}_j^*\dot{\mathbf{Z}}_j + \mathbf{Z}_j\dot{\mathbf{Z}}_j^*}{2})\Omega_{ij} \\
&- \sum_{n=1}^{d}a_{n,j}\langle \mathbf{Z}_i, \phi_l|\hat{H}|\phi_n, \mathbf{Z}_j\rangle]\} \\
&= 0\ .
\end{aligned} \tag{A.9}$$

If one solves Eqs. (3.33) and (A.9) simultaneously, then the only approximation left in the numerics with respect to a full variational study is just assuming only a finite number N of coherent basis states to describe the bath's modes, as evidenced in Eq. (3.30). The smart thing about the MCE approach is that another approximation is made here in Eq. (A.9). As we see, especially if the number of modes is large enough, as is the case in typically interesting situations, the overlaps $\langle \mathbf{Z}_i|\mathbf{Z}_j\rangle$ will customarily be very small, and thus one safely neglect them

in the evolution equation for the $\mathbf{Z}_j$ parameters (but, quite critically, keep them for the evolution of the coherent coefficients a_{lj}!). Therefore, instead of solving $N \times M$ complex equations for $N \times M$ complex parameters, the above equation can be greatly simplified by replacing it with Eq. (3.40), which is actually the same as the Eq. (A.7).

It is important to stress, here, that the overlaps Ω_{ij} are *not* disregarded for the whole dynamical equations, but only in the equations for the evolution of the time-dependent coherent states' grid. In fact, the coupling between different coherent states is actually essential to capture the full, "multi-configurational", quantum dynamics of the bath. In typical quantum evolutions, what happens is that, after some evolution time, the coherent states $|\mathbf{Z}_j\rangle$ drift away from each other, the overlaps Ω_{ij} become smaller and smaller, and one is left with an essentially semi-classical description, where the bath is described by orthogonal separated trajectories, and the coherent features of the quantum dynamics are lost.

Once the working equations for the expansion coefficients and moving trajectories (coupled coherent basis states) have been established, the essential problem reduces to how to choose an adequate initial set of coherent states in order to cover the important dynamical region and reflect the actual evolution accurately throughout the interesting time range. Moreover, since obviously only a finite size of the coherent basis set is utilized, a good initial sampling of the coherent basis states is crucial to achieve numerically converged result efficiently.

A.2 Sampling for the initial basis set

A.2.1 Gaussian wave packets, some history

Hellen [Hel75] was arguably the first to explore a semiclassical approach in which the wavefunction is represented as a superposition of time-dependent Gaussian wave functions. This approach was however quite restrictive, in that it was based

on the fact that Gaussian wave packets will remain Gaussian under certain conditions (for instance, under quadratic potentials). If such conditions are met, however, the problem of solving the time-dependence of the basis is reduced to finding the time evolution of few variables of the Gaussian wave packet.

In order to extend this approach to more general situations and longer times, Sawada and coworkers [SHJM85, SM86] turned to a method with multiple Gaussian wave-functions, but where each wave-function is isolated and independent from the others. By introducing a minimum error (MEM) method in [SHJM85], guided by the standard time-dependent Frenkel variational principle [Fre34], this method achieved better accuracy for longer times. The approach preserves some quantum effects and is not a purely classical method, but is still rather sensitive to the choice of preselected basis set, which must not only be good enough to represent the initial wavefunction, but also to describe the wave function adequately during the propagation time.

In the early eighties, Heller pioneered the idea of employing frozen Gaussian wave packets [Hel81], based on the heuristic intuition that such wave packets would establish 'collective correlations' since they share the same mean position and momentum.

A.2.2 The initial phase space grid

The time-dependent basis states we are using [Sha09] combines, in some sense, the advantages of the above Gaussian wave packets: (i) the wave-function is represented as a linear combination of 'frozen' Gaussian coherent basis states; (ii) all frozen Gaussian coherent basis states overlap with each other; (iii) the quantum coherence between different degrees of freedoms can be represented by superposing the frozen Gaussian states.

It is, however, still left to determine how to pick the initial grid of coherent states. Fortunately, in the case of thermal (or zero-temperature) baths consid-

ered throughout this dissertation, such a choice is clearly dictated by the physical conditions: to reproduce the distributions given by Eq. (3.45), at any temperature, we will in fact always start with the bath in a product of coherent states $|\mathbf{Z}_{ini}\rangle$. Hence, for each j, it is convenient to choose a Gaussian probability distribution p of the initial $\mathbf{Z}_j$ centered around $\mathbf{Z}_{ini}$:

$$p(\mathbf{Z}_j) = \frac{1}{\sqrt{2\pi\alpha_{comp}^2}} e^{\frac{-|\mathbf{Z}-\mathbf{Z}_{ini}|^2}{2\alpha_{comp}^2}}, \tag{A.10}$$

where α_{comp} is the standard deviation of the Gaussian distribution.

The parameter α_{comp} can be changed as suited and allows one to optimize the choice of the initial basis grid. A very good heuristic criterion to select a reliable frozen Gaussian basis set, is to check that the normalisation [SC08]

$$\langle \mathbf{Z}_{ini}|\hat{\mathbb{I}}|\mathbf{Z}_{ini}\rangle = \sum_{j,k}^{N} \langle \mathbf{Z}_{ini}|\mathbf{Z}_j\rangle \Omega_{j,k}^{-1} \langle \mathbf{Z}_k|\mathbf{Z}_{ini}\rangle \tag{A.11}$$

is close to 1. Of course, 'good' values of α_{comp} depend on N, and the issue here is to find a good combination of N and α_{comp}. It should be noted that, even if the frozen Gaussian basis states represent the initial wave-function very well, there's no guarantee that the basis states will be good enough for the evolution time considered. The only sure way to choose a good pair of N and α_{comp}, is to systematically converge the results with respect to these two parameters.

An analysis of the effect of different choices of basis grids may be found in [SC08]. During our investigations, we have tried at times different choices of the initial grids, but none seemed to give significant advantages over the simple Gaussian distribution, at least in the cases dealt with. For instance, when studying the convergence of our results for the Choi fidelity (Chapter 4), we have also adopted "conjugated" initial states (that is, distributions of pairs of complex conjugated numbers): results for these choice are displayed in Appendix B.

Note that, in the whole thesis, the 'compression parameter' *comp* is defined as

$$comp = \frac{1}{\alpha_{comp}}. \tag{A.12}$$

A.3 A note on the programming language

Our MCE code was first written in Matlab. However, the limitations of such an approach were immediately manifest: quite simply, the Matlab code proved to run painfully slowly on any desktop computer even for moderately low numbers of modes.

Therefore, I rewrote the code in Fortran90, in order to reduce computing time. More importantly, the Fortan code can be easily adjusted to run in parallel on UCL "Legion" cluster, which is very desirable for some of the cases we studied in this thesis (for instance, to obtain converged results at finite temperature in reasonable times).

Appendix B

Bath discretizations

In this appendix, we will first discuss how to approximate the continuous spectral density of a bath with a discrete set of modes and then specialise the argument to the Ohmic spin-boson case.

B.1 Generic spectral density

Given a set of M frequencies $\{\omega_j\}$ and spin-boson couplings $\{C_j\}$, one has that, at thermal equilibrium, the spectral density of the spin-bath system can be written as [LCD+87]

$$\frac{\pi}{2}\sum_{j=1}^{M}\frac{C_j^2}{m_j\omega_j}\delta(\omega-\omega_j)\ , \tag{B.1}$$

where C_j is the coupling strength between the spin and the jth bath's mode; (if two or more spins are present, we assume that the two spins have the same coupling strength with mode j) and m_j is the mass of the jth bath mode. It should be noted that the definition of C_j is different from the g_j as defined in chapter 4: assuming $\hbar = 1$, from the standard redefinition

$$\hat{x} = \sqrt{\frac{1}{2m_j\omega_j}}(b_j^+ + b_j) \tag{B.2}$$

one has that $C_j\hat{x}_j$ can be written as $g_j(b_j^+ + b_j)$, where

$$g_j = \frac{C_j}{\sqrt{2m_j\omega_j}} \, . \tag{B.3}$$

Now, given a generic continuous spectral density $J(\omega)$, we want to determine sets of frequencies and couplings capable of reproducing it. In other words, we want that

$$J(\omega) \simeq \frac{\pi}{2} \sum_{j=1}^{M} \frac{C_j^2}{m_j\omega_j} \delta(\omega - \omega_j) \, . \tag{B.4}$$

Considering the role of the delta functions as distributions, this equation can be recast as

$$\int_{-\infty}^{+\infty} J(\omega)T(\omega)d\omega \simeq \frac{\pi}{2} \sum_{j=1}^{M} \frac{C_j^2}{m_j\omega_j} T(\omega_j) \, ,$$

for any test function $T(\omega)$. We will now make the crucial assumptions that $T(\omega)$ varies very little over the typical interval between two frequencies $\Delta\omega_j = \omega_j - \omega_{j-1}$, and that $J(\omega)$ decays fast enough, such that

$$\frac{\pi}{2} \sum_{j=1}^{M} \frac{C_j^2}{m_j\omega_j} T(\omega_j) \simeq \int_{-\infty}^{+\infty} J(\omega)T(\omega)d\omega \simeq \sum_{j=1}^{M} J(\omega_j)T(\omega_j)\Delta\omega_j \, , \tag{B.5}$$

which must hold for all independent, smooth $T(\omega)$. Hence:

$$\frac{\pi}{2} \frac{C_j^2}{m_j\omega_j} = J(\omega_j)\Delta\omega_j \, . \tag{B.6}$$

It is convenient to re-parametrize the interval $\Delta\omega_j$ in terms of a continuous density of frequencies $\rho(\omega)$. First, define:

$$\frac{1}{\Delta\omega_j} = \rho(\omega_j) \, , \tag{B.7}$$

for a continuous and positive function $\rho(\omega)$. This condition does not entirely determine $\rho(\omega)$. For a slowly varying ρ, it can however be rewritten as

$$1 = \Delta\omega_j\rho(\omega_j) \simeq \int_{\omega_{j-1}}^{\omega_j} \rho(\omega)d\omega \, , \tag{B.8}$$

which finally gives:

$$\int_0^{\omega_j} \rho(\omega)d\omega = j \, , \qquad 1 \leq j \leq M \, . \tag{B.9}$$

Inserting Eq. (B.7) into Eq. (B.6) also determines the coupling strengths:

$$C_j^2 = \frac{2}{\pi} m_j \omega_j \frac{J(\omega_j)}{\rho(\omega_j)} \ . \tag{B.10}$$

Hence, given *any* set of M frequencies ω_j and any slowly varying positive function $\rho(\omega)$ satisfying (B.9), the choosing the coupling strengths according to (B.10) allows one to approximate the bath with continuous spectral density $J(\omega)$.

In principle, any density of frequencies $\rho(\omega)$ allows one to reproduce any bath's spectral density, in the sense that in the limit of M going to infinity all such choices reproduce the same spectral density. However, in practice, the rate of convergence to the desired spectral density does depend on the choice of $\rho(\omega)$ very much. A comparison between different discretizations for the super-Ohmic spin-boson case is included in chapter 5.

B.2 Ohmic bath

In chapter 4, we use a Ohmic form of the spectral density:

$$J(\omega) = \eta \omega e^{-\frac{\omega}{\omega_c}} \ , \tag{B.11}$$

where $\eta = \frac{\pi}{2}\alpha$, and α is the Kondo parameter.

Here, we adopt the same discretization method as in [WTM00]:

$$\rho(\omega_j) = \mathsf{a} \frac{J(\omega_j)}{\omega_j} \ , \tag{B.12}$$

where a is a re-normalization factor.

This choice of $\rho(\omega_j)$ proves to converge fairly quickly (as clear from the closeness of the $M = 50$ and $M = 100$ cases in Fig. 4.8) and has been demonstrated to work efficiently for the spin-boson model on several occasions [WTM00, MFP07, Sha09].

By substituting Eqs. B.11 and B.12 into equation B.9 one gets

$$\int_0^{\omega_{max}} \mathsf{a}\eta e^{-\omega/\omega_c} d\omega = M \tag{B.13}$$

where ω_{max} and ω_c are, respectively, the maximum frequency of the discrete set of frequencies and the cutoff frequency of the bath. Therefore, we have

$$\mathsf{a} = \frac{M}{\eta\omega_c[1 - e^{(-\omega_M/\omega_c)}]} \,. \tag{B.14}$$

Substituting the re-normalisation factor a into the Eq. (B.9) for the jth bath mode gives

$$\int_0^{\omega_j} d\omega(\mathsf{a}\frac{\eta\omega e^{-\frac{\omega}{\omega_c}}}{\omega}) = j. \tag{B.15}$$

Thus, we have a recipe for discretizing the bath frequencies:

$$\omega_j = -\omega_c \ln[1 - \frac{j(1 - e^{-\omega_M/\omega_c})}{M}] \tag{B.16}$$

which is the same as Eq. (4.17) in Chapter 3. Once the ω_j has been determined, then according to Eq. (B.10), we have

$$C_j = \omega_j\sqrt{\frac{2\eta\omega_c(1 - e^{-\omega_M/\omega_c})}{\pi M}} \,. \tag{B.17}$$

Hence, from Eq. (B.3), the recipe for the coupling strengths between bath and spins in Eq. (4.18) of chapter 4 is obtained.

Appendix C

Convergence of Choi Fidelity numerics

To give an idea of the quality and range of reliability of our results, we give here some evidence of the convergence of our numerics.

As clarified in Appendix A, the centres of the initial set of coherent states are distributed in phase space with a Gaussian distribution with standard deviation $1/comp$ [see Eq. (A.12)]. The parameter *comp* is a free parameter of the numerics, which is tuned to optimise convergence. As indicators of the quality of the numerics we will observe the convergence of specific entries of the density matrix of the two qubits $\widetilde{\rho}$, as well as the 'norm' $\mathrm{Tr}(\widetilde{\rho})$ and the expectation value of the energy $\mathrm{Tr}(\hat{H}\widetilde{\rho})$, which are obviously conserved in the exact dynamics. Notice that our method does not have any in-built routine enforcing the conservation of the state vector's norm, so that $\mathrm{Tr}(\widetilde{\rho})$ is a relevant figure of merit to assess its reliability.

We will see how MCE is more sensitive to the coupling strengths g_1 and g_2 in the full $\hat{H}$ model than for the rotating wave coupling of $\hat{H}_{rw}$, generally converges faster if the excitation number is conserved, and is however still capable to achieve converged results in quite general regimes very well.

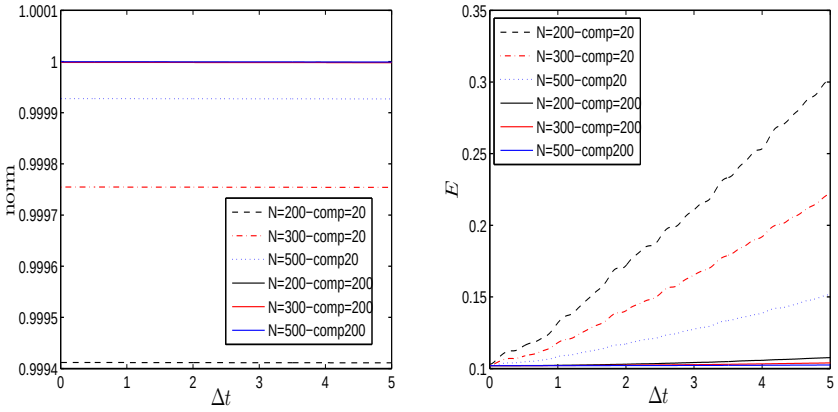

(a) Norm versus rescaled time (b) Energy versus rescaled time

Figure C.1: Norm and expectation value of the energy for MCE results at $\beta = 10$, for $\hat{H}_{rw}$ with $\varepsilon = \Delta = 0$, $g_1 = 1$, $g_2 = 2.1$, $M = 10$ (with $\omega_m = 0.1m$ for $1 \leq m \leq 10$) and different values of N and *comp*.

C.1 Rotating-wave number of excitations conserving Hamiltonian

C.1.1 Zero temperature

As one sees from Figs. C.1 and C.2, MCE converges in a clear and nice way in the case of conserved total excitation number, for initial spin state $|\uparrow\rangle\uparrow\rangle$, $g_1 = 1$, $g_2 = 2.1$ and $\beta = 10$. Fig. C.1 further confirms that a larger size of coherent basis set N and compression parameter *comp* make the total energy E and *norm* (close to 1) more stable. The density matrix's entries $\widetilde{\rho}_{11}$ and $\widetilde{\rho}_{1,3}$ also converge faster in terms of N and *comp*, if compared to the non-number conserving case of Fig. C.5.

C.1.2 Temperature convergence

To see how effectively MCE reproduces thermal distributions, we show three examples of our results at finite temperature (here, $\beta = 0.5$) with respect to

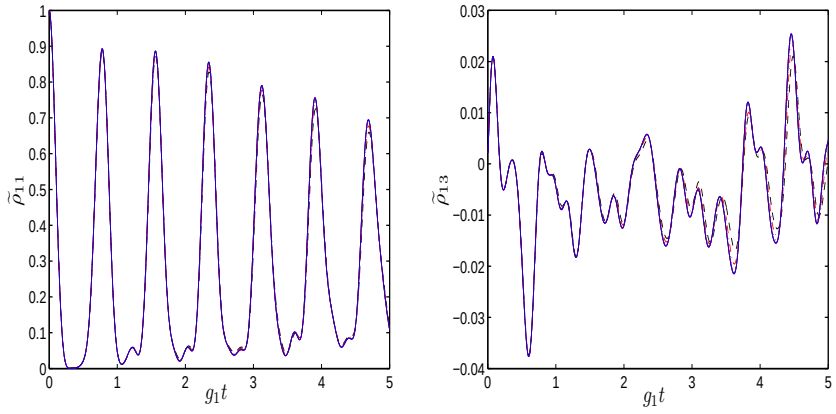

(a) $\widetilde{\rho}_{11}$ versus rescaled time (b) $\widetilde{\rho}_{13}$ versus rescaled time

Figure C.2: Entries of the qubits' density matrix $\widetilde{\rho}_{11}$ and $\widetilde{\rho}_{13}$ for MCE results at $\beta = 10$, for $\hat{H}_{rw}$ with $\varepsilon = \Delta = 0$, $g_1 = 1$, $g_2 = 2.1$, $M = 10$ (with $\omega_m = 0.1m$ for $1 \leq m \leq 10$) and different values of N and *comp*.

the increase in the number of states N_T over which the thermal distribution of Eq. (3.45) is sampled (Figs. C.3a ,C.3b and C.3c). Here, a total $N_T = 300$ initial states of the bath are sampled in batches of 50 to test the convergence. (For example, $N_T 1 - 50$ means $N_T = 50$ initial coherent states of the baths are sampled, while $N_T 51 - 100$ means that another different 50 states are sampled ($N_T = 50$).

C.2 Rotating wave Hamiltonian with tunnelling

Figs. C.4a and C.4b display the norm and expectation value of the energy for a case of non-number conserving rotating wave Hamiltonian (initial spin state $|\uparrow\uparrow\rangle$) with coupling strengths $g_1 = 1$ and $g_2 = 2.7$, while in Figs. C.5a and C.5b the entries $\widetilde{\rho}_{11}$ and $\widetilde{\rho}_{13}$ are plotted. The reliability of the numerics over the whole timeframe considered is apparent (for large enough compression parameter *comp*), in terms of both convergence with increasing number N of coherent states and of conservation of invariant quantities. For instance, though the total energy

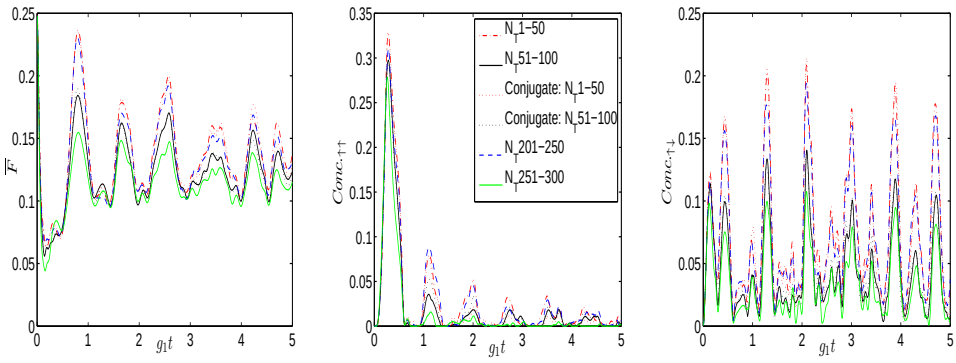

(a) Choi fidelity (b) Concurrence for initial state $\uparrow\uparrow\rangle$ (c) Concurrence for initial state $\uparrow\downarrow\rangle$

Figure C.3: Choi fidelity and concurrence for two different separable initial states versus rescaled time, for $\hat{H}_{rw}$ with $\varepsilon = \Delta = 0$, $g_1 = 1$, $g_2 = 2.1$, $\beta = 0.5$ and different values of N_T. In all plots $M = 10$ with $\omega_m = 0.1m$ for $1 \leq m \leq 10$. "Conjugate" refers to the fact that for those curves the initial centres of the coherent states to sample thermal distribution bath are in complex conjugate pairs.

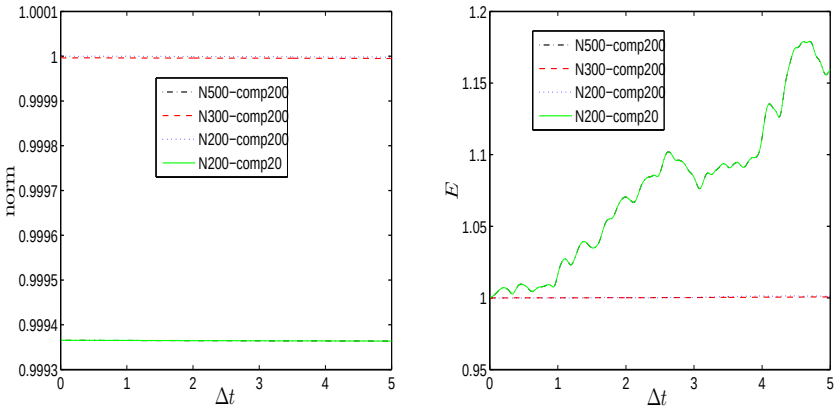

(a) Norm versus rescaled time (b) Energy versus rescaled time

Figure C.4: Norm and expectation value of the energy for MCE results at zero temperature, for $\hat{H}_{rw}$ with $\varepsilon = \Delta = g_1 = 1$, $g_2 = 2.7$, $M = 10$ (with $\omega_m = 0.1m$ for $1 \leq m \leq 10$) and different values of N and *comp*.

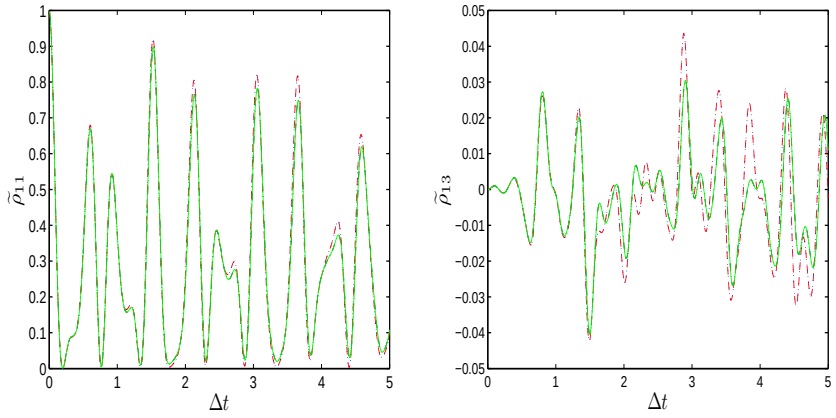

(a) $\widetilde{\rho}_{11}$ versus rescaled time (b) $\widetilde{\rho}_{13}$ versus rescaled time

Figure C.5: Entries of the qubits' density matrix $\widetilde{\rho}_{11}$ and $\widetilde{\rho}_{13}$ for MCE results at zero temperature, for $\hat{H}_{rw}$ with $\varepsilon = \Delta = g_1 = 1$, $g_2 = 2.7$, $M = 10$ (with $\omega_m = 0.1m$ for $1 \leq m \leq 10$) and different values of N and *comp*.

increases robust in the case of the compression parameter $comp = 20$, it maintains still in those cases of $comp = 200$. With regard to norm, energy, $\widetilde{\rho}_{11}$, and $\widetilde{\rho}_{13}$, under the same $comp = 200$, it is hard to distinguish the differences for sizes of coherent basis set ranging from $N = 200$ to $N = 500$.

C.3 Non rotating-wave Hamiltonian

As anticipated, the situation is much more dire for the full Hamiltonian $\hat{H}$ (initial spin state $|\uparrow\uparrow\rangle$). In this case, Figs. C.6 and C.7 show that our numerics are only reliable up to rescaled times around 2.5, after which both convergence, and norm and energy conservation are lost, even at smaller coupling strengths (in that $g_2 = 1$ rather than $g_2 = 2.7$ as before). For example, in Fig. C.7b, it is very clear that $\widetilde{\rho}_{13}$ can only be tracked for relatively short time, since the discrepancies between different size of coherent basis states N become quickly larger as time increases. The compression paramter $comp = 200$, seems better than $comp = 20$, as the total energy E is more stable as evidenced in Fig. C.6b. This feature is

similar to the case of $\hat{H}_{rw}$ in Fig. C.4b.

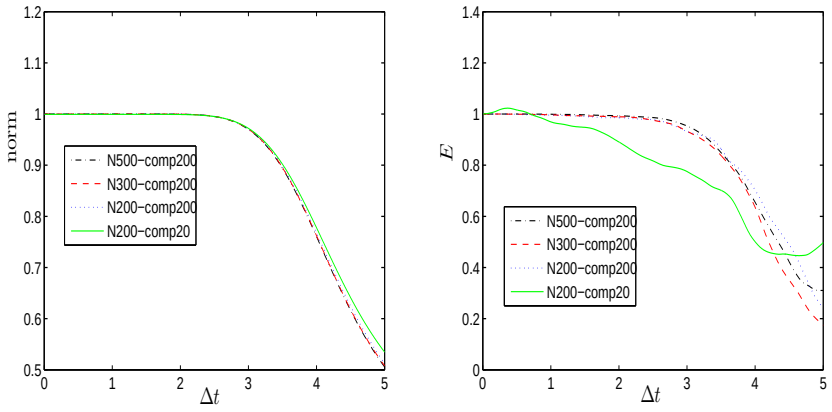

(a) Norm versus rescaled time (b) Energy versus rescaled time

Figure C.6: Norm and expectation value of the energy for MCE results at zero temperature, for $\hat{H}$ with $\varepsilon = \Delta = g_1 = g_2 = 1$, $M = 10$ (with $\omega_m = 0.1m$ for $1 \leq m \leq 10$) and different values of N and *comp*.

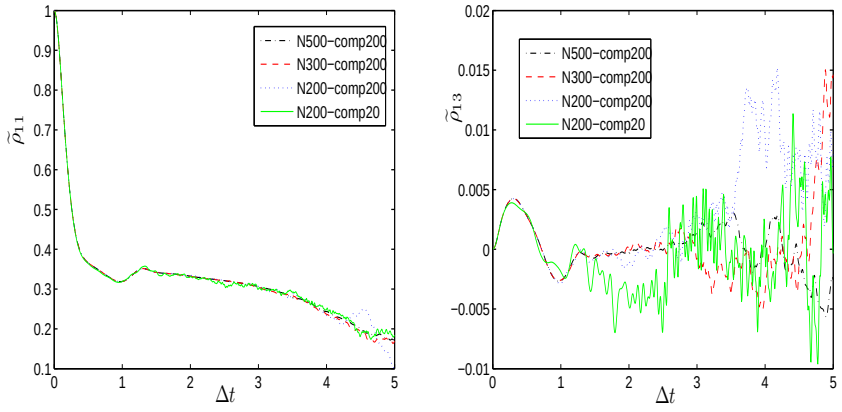

(a) $\widetilde{\rho}_{11}$ versus rescaled time (b) $\widetilde{\rho}_{13}$ versus rescaled time

Figure C.7: Entries of the qubits' density matrix $\widetilde{\rho}_{11}$ and $\widetilde{\rho}_{13}$ for MCE results at zero temperature, for $\hat{H}$ with $\varepsilon = \Delta = g_1 = g_2 = 1$, $M = 10$ (with $\omega_m = 0.1m$ for $1 \leq m \leq 10$) and different values of N and *comp*.

Appendix D

Convergence of super-Ohmic spin-boson numerics

In this appendix, we assess the convergence of our results for the population difference in a super-Ohmic bath (Chapter 5), with respect to three parameters: the number of bath modes M, the size of the coherent states' basis grid N and the compression parameter *comp*. Like in Chapter 5, two different initial bath states are considered: one where the bath is initially in a thermal equilibrium state (used to compare with MCTDH); one where each bath mode is displaced by the operator $\hat{D}(g_k/\omega_k)$ from the canonical thermal state (used to compare with QUAPI).

Not-shifted bath Fig. D.1a, for $M = 100$, shows a number of typical features. For the same size N of the phase space grid, a larger compression parameter *comp* keeps the energy more stable. Conversely, setting a fixed compression parameter *comp*, one can increase N to stabilise the expectation value of the energy. Fig. D.1b shows that increasing number of bath modes ($M = 200$) does not change the roles of N and *comp* significantly (with respect to Fig. D.1a).

Furthermore, and very interestingly, the results for $N = 500$ and $comp = 1000$ are almost the same as those for $N = 1000$ and $comp = 500$, which reveals that

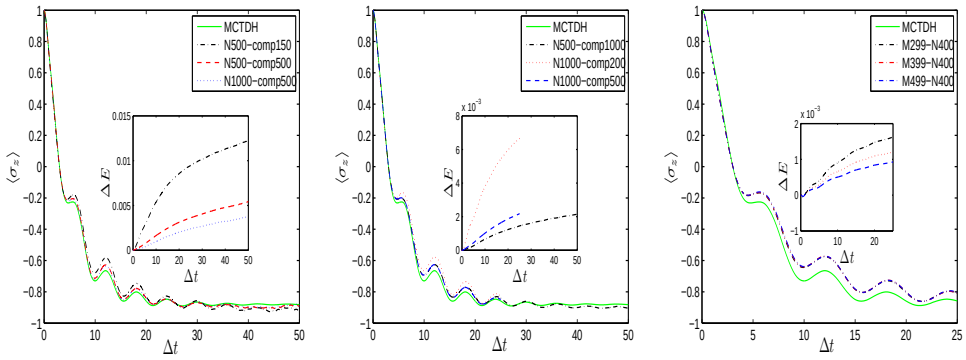

(a) $M = 100$ (b) $M = 200$ (c) $M = 299, 399, 499$

Figure D.1: The expectation value of $\langle\hat{\sigma}_z\rangle$ versus rescaled time by MCTDH (green-solid) and MCE with $\Delta = 1$, $\epsilon = 1$, $\delta_s = 0.01$, $\omega_c = 1$ and $\beta = 10$, in which the bath is initially in thermal equilibrium state. The MCE results are provided under same $\omega_{max} \to \infty$, but with different M, N and *comp*: In (a) $M = 100$; In (b) $M = 200$; In (c) $M = 299$ ($comp = 600$), $M = 399$ ($comp = 800$) and $M = 499$ ($comp = 1000$) with same $N = 400$. The insert figures are the corresponding energy deviation $\Delta E(t)$ versus the rescaled time.

a reasonably large *comp* can be adopted to reduce N and save computational cost. From Fig. D.1c it is clear that, for fixed $N = 400$, increasing M induces larger energy fluctuations. In this model, $N = 400$ seems not large enough to fully describe the dynamics for number of bath modes $M = 299$, $M = 399$ and $M = 499$. Obtaining converged results with respect to M is thus a somewhat more worrying concern than convergence with respect to N and *comp*, hence the need for an effective discretization of the bath. These are the maximum values of M and N we could reach so far, due to the limited computing resources and time.

Shifted bath Plots demonstrating convergence for shifted initial baths are depicted in Fig. D.2. Qualitatively, these data are analogous to those in Fig. D.1a, commented above.

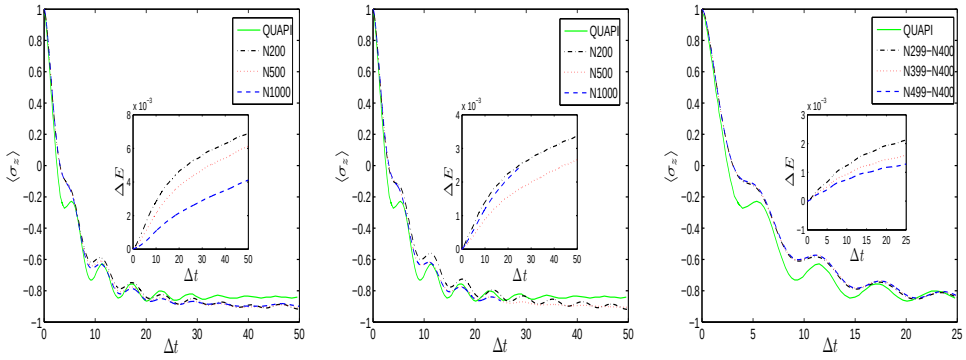

(a) $M = 100$ (b) $M = 200$ (c) $M = 299$, 399, 499

Figure D.2: The expectation value of $\langle\hat{\sigma_z}\rangle$ versus rescaled time by QUAPI (green-solid) and MCE (w1 discretization) with $\Delta = 1$, $\epsilon = 1$, $\delta_s = 0.01$, $\omega_c = 1$ and $\beta = 10$, for initially displaced thermal bath. The MCE results are provided under same $\omega_{max} \to \infty$, but with different M: In (a) $M = 100$: $comp = 500$ for $N = 200$, $N = 500$, $N = 1000$; In (b) $M = 200$: $comp = 500$ for $N = 200$ and $N = 1000$, $comp = 1000$ for $N = 500$; In (c) $M = 299$ ($comp = 600$), $M = 399$ ($comp = 800$) and $M = 499$ ($comp = 1000$) with same $N = 400$. The insert figures are the corresponding energy deviation $\Delta E(t)$ versus the rescaled time.

Appendix E

Time-derivative error for coupled coherent states

In this appendix, the formalism for evaluating the term $\kappa(t)$ for the error bound $\delta(t)$ introduced in Chapter 6 is provided for a basis of coupled coherent states. The state of the system stored in the computer, $|\psi'(t)\rangle$, is written as

$$|\psi'(t)\rangle = \sum_{l=1}^{d} \sum_{j=1}^{N} a_{lj} |l, \mathbf{Z}_j\rangle \ , \tag{E.1}$$

where d is the dimension of the finite dimensional ('spin') Hilbert space, while the bosonic modes are expanded in a set of N M-modes coherent states $|\mathbf{Z}_j\rangle = \bigotimes_{m=1}^{M} |Z_j^{(m)}\rangle$. Therefore, the projector operator can be expressed as

$$P_t = \sum_{l=1}^{d} \sum_{q=1,r=1}^{q=N,r=N} |l, \mathbf{Z}_q\rangle\langle l, \mathbf{Z}_r| \Omega_{qr}^{-1}, \tag{E.2}$$

where $\Omega_{qr} = \langle \mathbf{Z}_q | \mathbf{Z}_r \rangle$. Recalling that

$$|Z_j^{(m)}\rangle = \mathrm{e}^{-\frac{Z_j^{(m)} Z_j^{(m)*}}{2}} \sum_{n=0}^{\infty} \frac{Z_j^{(m)n}}{\sqrt{n!}} |n\rangle_m, \tag{E.3}$$

one has

$$\partial_{Z_j^{(m)}} |Z_j^{(m)}\rangle = (b_m^\dagger - \frac{Z_j^{(m)*}}{2}) |Z_j^{(m)}\rangle, \tag{E.4}$$

and

$$\partial_{Z_j^{(m)*}}|Z_j^{(m)}\rangle = -\frac{Z_j^{(m)}}{2}|Z_j^{(m)}\rangle. \tag{E.5}$$

These lead to

$$\begin{aligned}\partial_t|\psi'(t)\rangle = &\sum_{l=1}^{d}\sum_{j=1}^{N}\sum_{m=1}^{M}\left(\dot{a}_{lj} - a_{lj}\frac{Z_j^{(m)*}\dot{Z}_j^{(m)}}{2} - a_{lj}\frac{Z_j^{(m)}\dot{Z}_j^{(m)*}}{2}\right)|l,\mathbf{Z}_j\rangle \\ &+\sum_{l=1}^{d}\sum_{j=1}^{N}\sum_{m=1}^{M} a_{lj}\dot{Z}_j^{(m)}b_m^\dagger|l,\mathbf{Z}_j\rangle,\end{aligned} \tag{E.6}$$

and

$$\begin{aligned}P_t\partial_t|\psi'(t)\rangle = &\sum_{l=1}^{d}\sum_{j=1}^{N}\sum_{m=1}^{M}\left(\dot{a}_{lj} - a_{lj}\frac{Z_j^{(m)*}\dot{a}_j^{(m)}}{2} - a_{lj}\frac{Z_j^{(m)}\dot{Z}_j^{(m)*}}{2}\right)|l,\mathbf{Z}_j\rangle \\ &+\sum_{l=0}^{1}\sum_{j,q,r=1}^{N}\sum_{m=1}^{M}\Omega_{qr}^{-1}a_{lj}\dot{Z}_j^{(m)}Z_r^{(m)*}\Omega_{rj}|l,\mathbf{Z}_q\rangle.\end{aligned} \tag{E.7}$$

As one sees from the above two equations, the last terms in $\partial_t|\psi'(t)\rangle$ and $P_t\partial_t|\psi'(t)\rangle$ are different, giving rise to a non-zero $\kappa(t)$, as defined in Eq. (6.6) of Chapter 6. Although the vector $b_m^\dagger|Z_j^{(m)}\rangle$ is not accessible on the hard disk, one can calculate the overlap between the two vectors by applying the operator $b_m^\dagger$ on the bra side: $\langle Z_j^{(m)}|b_m^\dagger = \langle Z_j^{(m)}|Z_j^{(m)*}$, and thus evaluate $\kappa(t)$ exactly.

Publications

Publications prepared during the course of this work:

- **Modelling of quantum information processing with Ehrenfest guided trajectories: a case study**
  S.-Y. Ye, D. Shalashilin, and A. Serafini
  arXiv:1201.6171v1 Submitted to *Phys. Rev. A*

- **Coherent quantum effects through dispersive bosonic media**
  S.-Y. Ye, Z.-B. Yang, S.-B. Zheng and A.Serafini
  Phys. Rev. A **82**, 012307 (2010)

- **Distributed coherent manipulation of qutrits by virtual excitation processes**
  Z.-B. Yang, S.-Y. Ye, A. Serafini and S.-B. Zheng
  J. Phys. B: At. Mol. Opt. Phys. **43**, 085506 (2010)

Bibliography

[ABV07] F. B. Anders, R. Bulla, and M. Vojta. Equilibrium and nonequilibrium dynamics of the sub-ohmic spin-boson model. *Phys. Rev. Lett.*, 98:210402, May 2007.

[Ali02] R. Alicki. Decoherence in quantum open systems revisited. *arXiv:quant-ph/0205173v1*, 2002.

[BCP08] R. Bulla, T. A. Costi, and T. Pruschke. Numerical renormalization group method for quantum impurity systems. *Rev. Mod. Phys.*, 80:395–450, Apr 2008.

[BDD+02] M. J. Bremner, C. M. Dawson, J. L. Dodd, A. Gilchrist, A. W. Harrow, D. Mortimer, M. A. Nielsen, and T. J. Osborne. Practical scheme for quantum computation with any two-qubit entangling gate. *Phys. Rev. Lett.*, 89:247902, Nov 2002.

[BFM09] F. Benatti, R. Floreanini, and U. Marzolino. Environment-induced entanglement in a refined weak-coupling limit. *EPL (Europhysics Letters)*, 88(2):20011, 2009.

[BFP03] F. Benatti, R. Floreanini, and M. Piani. Environment induced entanglement in markovian dissipative dynamics. *Phys. Rev. Lett.*, 91:070402, Aug 2003.

[BGW08] I. Burghardt, K. Giri, and G. A. Worth. Multimode quantum dynamics using gaussian wavepackets: The gaussian-based multicon-

figuration time-dependent hartree (g-mctdh) method applied to the absorption spectrum of pyrazine. *J. Chem. Phys.*, 129(17):174104, 2008.

[Bil83] G. D. Billing. On the use of ehrenfest's theorem in molecular scattering. *Chem. Phys. Lett.*, 100(6):535 – 539, 1983.

[BJWM00] M. H. Beck, A. Jäckle, G. A. Worth, and H.-D. Meyer. The multiconfiguration time-dependent hartree (mctdh) method: a highly efficient algorithm for propagating wavepackets. *Phys. Rep.*, 324(1):1 – 105, 2000.

[BLTV05] R. Bulla, H.-J. Lee, N.-H. Tong, and M. Vojta. Numerical renormalization group for quantum impurities in a bosonic bath. *Phys. Rev. B*, 71:045122, Jan 2005.

[BM82] A. J. Bray and M. A. Moore. Influence of dissipation on quantum coherence. *Phys. Rev. Lett.*, 49:1545–1549, Nov 1982.

[BMC99] I. Burghardt, H.-D. Meyer, and L. S. Cederbaum. Approaches to the approximate treatment of complex molecular systems by the multiconfiguration time-dependent hartree method. *J. Chem. Phys.*, 111(7):2927–2939, 1999.

[BP06] B. Barbiellini and P. M. Platzman. The healing mechanism for excited molecules near metallic surfaces. *New J. Phys.*, 8(2):20, 2006.

[CCD+09] F. Caruso, A. W. Chin, A. Datta, S. F. Huelga, and M. B. Plenio. Highly efficient energy excitation transfer in light-harvesting complexes: The fundamental role of noise-assisted transport. *J. Chem. Phys.*, 131(10):105106, 2009.

[CDC+10] A. W. Chin, A. Datta, F. Caruso, S. F. Huelga, and M. B. Plenio. Noise-assisted energy transfer in quantum networks and light-harvesting complexes. *New J. Phys.*, 12(6):065002, 2010.

[CEHM99] J. I. Cirac, A. K. Ekert, S. F. Huelga, and C. Macchiavello. Distributed quantum computation over noisy channels. *Phys. Rev. A*, 59:4249–4254, Jun 1999.

[CHP11] A. W. Chin, S. F. Huelga, and M. B. Plenio. Chapter 4 - chain representations of open quantum systems and their numerical simulation with time-adaptive density matrix renormalisation group methods. In M. Thorwart U. Wüerfel and E. R. Weber, editors, *Quantum Efficiency in Complex Systems, Part II From Molecular Aggregates to Organic Solar Cells*, volume 85 of *Semiconductors and Semimetals*, pages 115 – 143. Elsevier, 2011.

[CL81] A. O. Caldeira and A. J. Leggett. Influence of dissipation on quantum tunneling in macroscopic systems. *Phys. Rev. Lett.*, 46:211–214, Jan 1981.

[CL83] A. O. Caldeira and A. J. Leggett. Quantum tunnelling in a dissipative system. *Ann. Phys.*, 149(2):374 – 456, 1983.

[CL84] S. Chakravarty and A. J. Leggett. Dynamics of the two-state system with ohmic dissipation. *Phys. Rev. Lett.*, 52:5–8, Jan 1984.

[CPA08] L. D. Contreras-Pulido and R. Aguado. Entanglement between charge qubits induced by a common dissipative environment. *Phys. Rev. B*, 77:155420, Apr 2008.

[CPGP03] S. Clark, A. Peng, M. Gu, and S. Parkins. Unconditional preparation of entanglement between atoms in cascaded optical cavities. *Phys. Rev. Lett.*, 91:177901, Oct 2003.

[CPHP11] A. W. Chin, J. Prior, S. F. Huelga, and M. B. Plenio. Generalized polaron ansatz for the ground state of the sub-ohmic spin-boson model: An analytic theory of the localization transition. *Phys. Rev. Lett.*, 107:160601, Oct 2011.

[CS06] B. Collins and P. Śniady. Integration with respect to the haar measure on unitary, orthogonal and symplectic group. *Commun. Math. Phys.*, 264:773–795, 2006. 10.1007/s00220-006-1554-3.

[CVDC03] T. S. Cubitt, F. Verstraete, W. Dür, and J. I. Cirac. Separable states can be used to distribute entanglement. *Phys. Rev. Lett.*, 91:037902, Jul 2003.

[CWW+10] E. Collini, C. Y. Wong, K. E. Wilk, P. M. G. Curmi, P. Brumer, and G. D. Scholes. Coherently wired light-harvesting in photosynthetic marine algae at ambient temperature. *Nature*, 463:644–647, 2010.

[CZ95] J. I. Cirac and P. Zoller. Quantum computations with cold trapped ions. *Phys. Rev. Lett.*, 74:4091–4094, May 1995.

[CZKM97] J. I. Cirac, P. Zoller, H. J. Kimble, and H. Mabuchi. Quantum state transfer and entanglement distribution among distant nodes in a quantum network. *Phys. Rev. Lett.*, 78:3221–3224, Apr 1997.

[DKSV04] A. J. Daley, C. Kollath, U. Schollwöck, and G. Vidal. Time-dependent density-matrix renormalization-group using adaptive effective hilbert spaces. *J. Stat. Mech.*, 2004(04):P04005, 2004.

[DP12] F. Schmidt-Kaler D. Porras, P. A. Ivanov. Quantum simulation of cooperative jahn-teller systems with linear ion crystals. *arXiv:quant-ph/0205173v1*, 2012.

[Eck09] J. Eckel. *Non-Markovian effects in open quantum systems.* PhD thesis, Heinrich-Heine-Universität Düsseldorf, 2009.

[ECR+07] G. S. Engel, T. R. Calhoun, E. L. Read, T.-K. Ahn, T. Mančal, Y.-C. Cheng, R. E. Blankenship, and G. R. Fleming. Evidence for wavelike energy transfer through quantum coherence in photosynthetic systems. *Nature*, 446:782–786, 2007.

[Ehr27] P. Ehrenfest. Bemerkung über die angenäherte gültigkeit der klassischen mechanik innerhalb der quantenmechanik. *Z. Phys. A*, 45:455–457, 1927. 10.1007/BF01329203.

[EM94] R. Egger and C. H. Mak. Low-temperature dynamical simulation of spin-boson systems. *Phys. Rev. B*, 50:15210–15220, Nov 1994.

[EW92] R. Egger and U. Weiss. Quantum monte carlo simulation of the dynamics of the spin-boson model. *Z. Phys. B*, 89:97–107, 1992. 10.1007/BF01320834.

[FI07] L. Faoro and L. B. Ioffe. Microscopic origin of critical current fluctuations in large, small, and ultra-small area josephson junctions. *Phys. Rev. B*, 75:132505, Apr 2007.

[FN07] F. F. Fanchini and R. d. J. Napolitano. Continuous dynamical protection of two-qubit entanglement from uncorrelated dephasing, bit flipping, and dissipation. *Phys. Rev. A*, 76:062306, Dec 2007.

[FNOC10] F. Fassioli, A. Nazir, and A. Olaya-Castro. Quantum state tuning of energy transfer in a correlated environment. *J. Phys. Chem.Lett.*, 1(14):2139–2143, 2010.

[Fre34] J. Frenkel. *Wave Mechanics*. Clarendon Press, Oxford, 1934.

[GBR82] R. B. Gerber, V. Buch, and M. A. Ratner. Time-dependent self-consistent field approximation for intramolecular energy transfer. i. formulation and application to dissociation of van der waals molecules. *J. Chem. Phys.*, 77(6):3022–3030, 1982.

[GK06] G. Gordon and G. Kurizki. Preventing multipartite disentanglement by local modulations. *Phys. Rev. Lett.*, 97:110503, Sep 2006.

[GOA85] A. Garg, J. N. Onuchic, and V. Ambegaokar. Effect of friction on electron transfer in biomolecules. *J. Chem. Phys.*, 83(9):4491–4503, 1985.

[GRB82] R. B. Gerber, M. A. Ratner, and V. Buch. Simplified time-dependent self-consistent field approximation for intramolecular dynamics. *Chem. Phys. Lett.*, 91(3):173 – 177, 1982.

[GRTZ02] N. Gisin, G. Ribordy, W. Tittel, and H. Zbinden. Quantum cryptography. *Rev. Mod. Phys.*, 74:145–195, Mar 2002.

[GSW89] R. Görlich, M. Sassetti, and U. Weiss. Low-temperature properties of biased two-level systems: Effects of frequency-dependent damping. *EPL (Europhysics Letters)*, 10(6):507, 1989.

[HC10] P. Huo and D. F. Coker. Iterative linearized density matrix propagation for modeling coherent excitation energy transfer in photosynthetic light harvesting. *J. Chem. Phys.*, 133(18):184108, 2010.

[Hel75] E. J. Heller. Time-dependent approach to semiclassical dynamics. *J. Chem. Phys.*, 62(4):1544–1555, 1975.

[Hel81] E. J. Heller. Frozen gaussians: A very simple semiclassical approximation. *J. Chem. Phys.*, 75(6):2923–2931, 1981.

[HMK05] D. J. Heijs, V. A. Malyshev, and J. Knoester. Decoherence of excitons in multichromophore systems: Thermal line broadening and destruction of superradiant emission. *Phys. Rev. Lett.*, 95:177402, Oct 2005.

[Hor09] K. Hornberger. Introduction to decoherence theory. In Andreas Buchleitner, Carlos Viviescas, and Markus Tiersch, editors, *Entan-*

glement and Decoherence, volume 768 of *Lecture Notes in Physics*, pages 221–276. Springer Berlin / Heidelberg, 2009.

[HP11] S. F. Huelga and M. B. Plenio. Quantum dynamics of bio-molecular systems in noisy environments. *Procedia Chemistry*, 3(1):248 – 257, 2011. ¡ce:title¿22nd Solvay Conference on Chemistry¡/ce:title¿.

[HPB02] F. Petruccione H.-P. Breuer. *The theory of open quantum systems.* Oxford University Press, 2002.

[Hu10] Q. Hu. *Mode Synthesis in Photonic Bandgap Fibers: Enabling superpositions and transmissions of modes in cylindrically-symmetric multimode photonic bandgap fibers.* LAP Lambert Academic Publishing, 2010.

[IF09a] A. Ishizaki and G. R. Fleming. Theoretical examination of quantum coherence in a photosynthetic system at physiological temperature. *PNAS*, 106(41):17255–17260, 2009.

[IF09b] A. Ishizaki and G. R. Fleming. Unified treatment of quantum coherent and incoherent hopping dynamics in electronic energy transfer: Reduced hierarchy equation approach. *J. Chem. Phys.*, 130(23):234111, 2009.

[Jan09] S. Jang. Theory of coherent resonance energy transfer for coherent initial condition. *J. Chem. Phys.*, 131(16):164101, 2009.

[JCRE08] S. Jang, Y.-C. Cheng, D. R. Reichman, and J. D. Eaves. Theory of coherent resonance energy transfer. *J. Chem. Phys.*, 129(10):101104, 2008.

[JJWM08] J. D. Joannopoulos, S. G. Johnson, J. N. Winn, and R. D. Meade. *Photonic Crystals: Molding the Flow of Light (Second Edition).* Princeton University Press, 2008.

[JNS04] S. Jang, M. D. Newton, and R. J. Silbey. Multichromophoric förster resonance energy transfer. *Phys. Rev. Lett.*, 92:218301, May 2004.

[JNS07] S. Jang, M. D. Newton, and R. J. Silbey. Multichromophoric förster resonance energy transfer from b800 to b850 in the light harvesting complex 2: evidence for subtle energetic optimization by purple bacteria. *J. Phys. Chem. B*, 111(24):6807–6814, 2007. PMID: 17439170.

[KHS03] S. Y. Kim and S. Hammes-Schiffer. Molecular dynamics with quantum transitions for proton transfer: Quantum treatment of hydrogen and donor–acceptor motions. *J. Chem. Phys.*, 119(8):4389–4398, 2003.

[Kim08] H. J. Kimble. The quantum internet. *Nature*, 453:1023–31030, 2008.

[Kni05] E. Knill. Quantum computing with realistically noisy devices. *Nature*, 434:39–44, 2005.

[Kos88] R. Kosloff. Time-dependent quantum-mechanical methods for molecular dynamics. *J. Phys. Chem.*, 92(8):2087–2100, 1988.

[KS01] M. Keil and H. Schoeller. Real-time renormalization-group analysis of the dynamics of the spin-boson model. *Phys. Rev. B*, 63:180302, Apr 2001.

[KSP+11] M. Kohnen, M. Succo, P. G. Petrov, M. Trupke, P. G. Petrov, R. A. Nyman, and Hinds E. A. An array of integrated atom-photon junction. *Nat. Photonics*, 5:35–38, 2011.

[LCD+87] A. J. Leggett, S. Chakravarty, A. T. Dorsey, Matthew P. A. Fisher, A. Garg, and W. Zwerger. Dynamics of the dissipative two-state system. *Rev. Mod. Phys.*, 59:1–85, Jan 1987.

[LCD+95] A. J. Leggett, S. Chakravarty, A. T. Dorsey, Matthew P. A. Fisher, A. Garg, and W. Zwerger. Erratum: Dynamics of the dissipative two-state system. *Rev. Mod. Phys.*, 67:725–726, Jul 1995.

[LCF07] H. Lee, Y.-C. Cheng, and G. R. Fleming. Coherence dynamics in photosynthesis: Protein protection of excitonic coherence. *Science*, 316(5830):1462–1465, 2007.

[LCW98] D. A. Lidar, I. L. Chuang, and K. B. Whaley. Decoherence-free subspaces for quantum computation. *Phys. Rev. Lett.*, 81:2594–2597, Sep 1998.

[LDM+02] D. Leibfried, B. DeMarco, V. Meyer, M. Rowe, A. Ben-Kish, J. Britton, W. M. Itano, B. Jelenković, C. Langer, T. Rosenband, and D. J. Wineland. Trapped-ion quantum simulator: Experimental application to nonlinear interferometers. *Phys. Rev. Lett.*, 89:247901, Nov 2002.

[LDM+03] D. Leibfried, B. DeMarco, V. Meyer, D. Lucas, M. Barrett, J. Britton, W. M. Itano, B. Jelenković, C. Langer, T. Rosenband, and D. J. Wineland. Experimental demonstration of a robust, high-fidelity geometric two ion-qubit phase gate. *Nature*, 422:412–415, 2003.

[LFvDN+04] P. Lodahl, A. Floris van Driel, I. S. Nikolaev, A. Irman, K. Overgaag, D. Vanmaekelbergh, and W. L. Vos. Controlling the dynamics of spontaneous emission from quantum dots by photonic crystals. *Nature*, 430:654–657, 2004.

[LHDBH07] K. Le Hur, P. Doucet-Beaupré, and W. Hofstetter. Entanglement and criticality in quantum impurity systems. *Phys. Rev. Lett.*, 99:126801, Sep 2007.

[LJL+10] T. D. Ladd, F. Jelezko, R. Laflamme, Y. Nakamura, C. Monroe, and J. L. O'Brien. Quantum computers. *Nature*, 464:45–53, 2010.

[Lub08] C. Lubich. *From Quantum to Classical Molecular Dynamics: Reduced Models and Numerical Analysis (Zurich Lectures in Advanced Mathematics)*. European Mathematical Society, 2008.

[MAN00] I. L. Chuang M. A. Nielsen. *Quantum Information and Quantum Computation*. Cambridge University Press, 2000.

[ME03] L. Muhlbacher and R. Egger. Crossover from nonadiabatic to adiabatic electron transfer reactions: Multilevel blocking monte carlo simulations. *J. Chem. Phys.*, 118(1):179–191, 2003.

[ME04] L. Mühlbacher and R. Egger. Electron transfer rates for asymmetric reactions. *Chem. Phys.*, 296(2-3):193 – 199, 2004.

[MFP07] E. Martin-Fierro and E. Pollak. Semiclassical initial value series solution of the spin boson problem. *J. Chem. Phys.*, 126(16):164108, 2007.

[MFZ+08] S. Maniscalco, F. Francica, R. L. Zaffino, L. G. Nicola, and F. Plastina. Protecting entanglement via the quantum zeno effect. *Phys. Rev. Lett.*, 100:090503, Mar 2008.

[MM79] H.-D. Meyera and W. H. Miller. A classical analog for electronic degrees of freedom in nonadiabatic collision processes. *J. Chem. Phys.*, 70(7):3214–3223, 1979.

[MM87] N. Makri and W. H. Miller. Time-dependent self-consistent field (tdscf) approximation for a reaction coordinate coupled to a harmonic bath: Single and multiple configuration treatments. *J. Chem. Phys.*, 87(10):5781–5787, 1987.

[MM95a] N. Makri and D. E. Makarov. Tensor propagator for iterative quantum time evolution of reduced density matrices. i. theory. *J. Chem. Phys.*, 102(11):4600–4610, 1995.

[MM95b] N. Makri and D. E. Makarov. Tensor propagator for iterative quantum time evolution of reduced density matrices. ii. numerical methodology. *J. Chem. Phys.*, 102(11):4611–4618, 1995.

[MMC90] H.-D. Meyer, U. Manthe, and L.S. Cederbaum. The multi-configurational time-dependent hartree approach. *Chem. Phys. Lett.*, 165(1):73 – 78, 1990.

[MMC92] U. Manthe, H.-D. Meyer, and L. S. Cederbaum. Wave-packet dynamics within the multiconfiguration hartree framework: General aspects and application to nocl. *J. Chem. Phys.*, 97(5):3199–3213, 1992.

[MN10] D. P. S. McCutcheon and A. Nazir. Quantum dot rabi rotations beyond the weak exciton–phonon coupling regime. *New Journal of Physics*, 12(11):113042, 2010.

[MN11] D. P. S. McCutcheon and A. Nazir. Coherent and incoherent dynamics in excitonic energy transfer: Correlated fluctuations and off-resonance effects. *Phys. Rev. B*, 83:165101, Apr 2011.

[MNBF09] D. P. S. McCutcheon, A. Nazir, S. Bose, and A. J. Fisher. Long-lived spin entanglement induced by a spatially correlated thermal bath. *Phys. Rev. A*, 80:022337, Aug 2009.

[MRLAG08] M. Mohseni, P. Rebentrost, S. Lloyd, and A. Aspuru-Guzik. Environment-assisted quantum walks in photosynthetic energy transfer. *J. Chem. Phys.*, 129(17):174106, 2008.

[MW03] H.-D. Meyer and G. A. Worth. Quantum molecular dynamics: propagating wavepackets and density operators using the multiconfigu-

ration time-dependent hartree method. *Theoretical Chemistry Accounts: Theory, Computation, and Modeling (Theoretica Chimica Acta)*, 109:251–267, 2003.

[Naz09] A. Nazir. Correlation-dependent coherent to incoherent transitions in resonant energy transfer dynamics. *Phys. Rev. Lett.*, 103:146404, Oct 2009.

[NET10] P. Nalbach, J. Eckel, and M. Thorwart. Quantum coherent biomolecular energy transfer with spatially correlated fluctuations. *New J. Phys.*, 12(6):065043, 2010.

[NPTG07] F. Nesi, E. Paladino, M. Thorwart, and M. Grifoni. Spin-boson dynamics beyond conventional perturbation theories. *Phys. Rev. B*, 76:155323, Oct 2007.

[OCLOJ08] A. Olaya-Castro, C. F. Lee, F. F Olsen, and N. F. Johnson. Efficiency of energy transfer in a light-harvesting system under quantum coherence. *Phys. Rev. B*, 78:085115, Aug 2008.

[OSLH08] P. P. Orth, I. Stanic, and K. Le Hur. Dissipative quantum ising model in a cold-atom spin-boson mixture. *Phys. Rev. A*, 77:051601, May 2008.

[PCHP10] J. Prior, A. W. Chin, S. F. Huelga, and M. B. Plenio. Efficient simulation of strong system-environment interactions. *Phys. Rev. Lett.*, 105:050404, Jul 2010.

[Pel97] T. Pellizzari. Quantum networking with optical fibres. *Phys. Rev. Lett.*, 79:5242–5245, Dec 1997.

[PH02] M. B. Plenio and S. F. Huelga. Entangled light from white noise. *Phys. Rev. Lett.*, 88:197901, Apr 2002.

[PH08] M. B. Plenio and S. F. Huelga. Dephasing-assisted transport: quantum networks and biomolecules. *New J. Phys.*, 10(11):113019, 2008.

[PHBK99] M. B. Plenio, S. F. Huelga, A. Beige, and P. L. Knight. Cavity-loss-induced generation of entangled atoms. *Phys. Rev. A*, 59:2468–2475, Mar 1999.

[PMvDC08] D. Porras, F. Marquardt, J. von Delft, and J. I. Cirac. Mesoscopic spin-boson models of trapped ions. *Phys. Rev. A*, 78:010101, Jul 2008.

[RB01] R. Raussendorf and H. J. Briegel. A one-way quantum computer. *Phys. Rev. Lett.*, 86:5188–5191, May 2001.

[Rei09] B. Reichardt. Error-detection-based quantum fault-tolerance threshold. *Algorithmica*, 55:517–556, 2009. 10.1007/s00453-007-9069-7.

[RFZ+05] A. Recati, P. O. Fedichev, W. Zwerger, J. von Delft, and P. Zoller. Atomic quantum dots coupled to a reservoir of a superfluid bose-einstein condensate. *Phys. Rev. Lett.*, 94:040404, Feb 2005.

[RGB+10] A. J. Ramsay, T. M. Godden, S. J. Boyle, E. M. Gauger, A. Nazir, B. W. Lovett, A. M. Fox, and M. S. Skolnick. Phonon-induced rabi-frequency renormalization of optically driven single InGaAs/GaAs quantum dots. *Phys. Rev. Lett.*, 105:177402, Oct 2010.

[RGG+10] A. J. Ramsay, A. V. Gopal, E. M. Gauger, A. Nazir, B. W. Lovett, A. M. Fox, and M. S. Skolnick. Damping of exciton rabi rotations by acoustic phonons in optically excited InGaAs/GaAs quantum dots. *Phys. Rev. Lett.*, 104:017402, Jan 2010.

[RH07] R. Raussendorf and J. Harrington. Fault-tolerant quantum computation with high threshold in two dimensions. *Phys. Rev. Lett.*, 98:190504, May 2007.

[RNO+99] A. Rauschenbeutel, G. Nogues, S. Osnaghi, P. Bertet, M. Brune, J. M. Raimond, and S. Haroche. Coherent operation of a tunable

quantum phase gate in cavity qed. *Phys. Rev. Lett.*, 83:5166–5169, Dec 1999.

[San92] B. C. Sanders. Entangled coherent states. *Phys. Rev. A*, 45:6811–6815, May 1992.

[SC00] D. V. Shalashilin and M. S. Child. Time dependent quantum propagation in phase space. *J. Chem. Phys.*, 113(22):10028–10036, 2000.

[SC01a] D. V. Shalashilin and M. S. Child. Description of tunneling with the help of coupled frozen gaussians. *J. Chem. Phys.*, 114(21):9296–9304, 2001.

[SC01b] D. V. Shalashilin and M. S. Child. Multidimensional quantum propagation with the help of coupled coherent states. *J. Chem. Phys.*, 115(12):5367–5375, 2001.

[SC04] D. V. Shalashilin and M. S. Child. Real time quantum propagation on a monte carlo trajectory guided grids of coupled coherent states: 26d simulation of pyrazine absorption spectrum. *J. Chem. Phys.*, 121(8):3563–3568, 2004.

[SC08] D. V. Shalashilin and M. S. Child. Basis set sampling in the method of coupled coherent states: Coherent state swarms, trains, and pancakes. *J. Chem. Phys.*, 128(5):054102, 2008.

[Sha09] D. V. Shalashilin. Quantum mechanics with the basis set guided by ehrenfest trajectories: Theory and application to spin-boson model. *J. Chem. Phys.*, 130(24):244101, 2009.

[SHJM85] S.-I. Sawada, R. Heather, B. Jackson, and H. Metiu. A strategy for time dependent quantum mechanical calculations using a gaussian wave packet representation of the wave function. *J. Chem. Phys.*, 83(6):3009–3027, 1985.

[SKS06] M. Schr´oder, U. Kleinekathofer, and M. Schreiber. Calculation of absorption spectra for light-harvesting systems using non-markovian approaches as well as modified redfield theory. *J. Chem. Phys.*, 124(8):084903, 2006.

[SM86] S. Sawada and H. Metiu. A multiple trajectory theory for curve crossing problems obtained by using a gaussian wave packet representation of the nuclear motion. *J. Chem. Phys.*, 84(1):227–238, 1986.

[SMB97] P. M. Radmore S. M. Barnett. *Methods in theoretical quantum optics*. Clarendon Press, 1997.

[SMB06] A. Serafini, S. Mancini, and S. Bose. Distributed quantum computation via optical fibers. *Phys. Rev. Lett.*, 96:010503, Jan 2006.

[SMSS06] J. Schriefl, Y. Makhlin, A. Shnirman, and G. Schön. Decoherence from ensembles of two-level fluctuators. *New J. Phys.*, 8(1):1, 2006.

[SMW07] M. Stobińska, G. Milburn, and K. Wódkiewicz. Effective generation of cat and kitten states. *Open Systems and Information Dynamics*, 14:81–90, 2007. 10.1007/s11080-007-9031-9.

[SSC06] P. A. J. Sherratt, D. V. Shalashillin, and M. S. Child. Description of multidimensional tunnelling with the help of coupled coherent states guided by classical hamiltonians with quantum corrections. *Chem. Phys.*, 322(1-2):127 – 134, 2006.

[Ste03] A. M. Steane. Overhead and noise threshold of fault-tolerant quantum error correction. *Phys. Rev. A*, 68:042322, Oct 2003.

[STP06] D. Solenov, D. Tolkunov, and V. Privman. Coherent interaction of spins induced by thermal bosonic environment. *Physics Letters A*, 359(2):81 – 85, 2006.

[TBAN08] S. Tornow, R. Bulla, F. B. Anders, and A. Nitzan. Dissipative two-electron transfer: A numerical renormalization group study. *Phys. Rev. B*, 78:035434, Jul 2008.

[TER+09] M. Thorwart, J. Eckel, J.H. Reina, P. Nalbach, and S. Weiss. Enhanced quantum entanglement in the non-markovian dynamics of biomolecular excitons. *Chem. Phys. Lett.*, 478(4-6):234 – 237, 2009.

[TGD+07] M. Trupke, J. Goldwin, B. Darquié, G. Dutier, S. Eriksson, J. Ashmore, and E. A. Hinds. Atom detection and photon production in a scalable, open, optical microcavity. *Phys. Rev. Lett.*, 99:063601, Aug 2007.

[TGH01] M. Thorwart, M. Grifoni, and P. Hänggi. Strong coupling theory for tunneling and vibrational relaxation in driven bistable systems. *Ann. Phys.*, 293(1):15 – 66, 2001.

[Toa09] O. Toader. *Photonic Bandgap Materials: Architectures for Microfabrication and their Optical Properties.* LAP Lambert Academic Publishing, 2009.

[TT10] M. Tanaka and Y. Tanimura. Multistate electron transfer dynamics in the condensed phase: Exact calculations from the reduced hierarchy equations of motion approach. *J. Chem. Phys.*, 132(21):214502, 2010.

[TV06] N.-H. Tong and M. Vojta. Signatures of a noise-induced quantum phase transition in a mesoscopic metal ring. *Phys. Rev. Lett.*, 97:016802, Jul 2006.

[V̈98] K. Völker. Dynamical behavior of the dissipative two-state system. *Phys. Rev. B*, 58:1862–1871, Jul 1998.

[VB03] T. Vorrath and T. Brandes. Dicke effect in the tunnel current

through two double quantum dots. *Phys. Rev. B*, 68:035309, Jul 2003.

[vEKCZ99] S. J. van Enk, H. J. Kimble, J. I. Cirac, and P. Zoller. Quantum communication with dark photons. *Phys. Rev. A*, 59:2659–2664, Apr 1999.

[Ẅ98] A. Würger. Strong-coupling theory for the spin-phonon model. *Phys. Rev. B*, 57:347–361, Jan 1998.

[Wan00] H. Wang. Basis set approach to the quantum dissipative dynamics: Application of the multiconfiguration time-dependent hartree method to the spin-boson problem. *J. Chem. Phys.*, 113(22):9948–9956, 2000.

[WDS06] W. M. Witzel and S. Das Sarma. Quantum theory for electron spin decoherence induced by nuclear spin dynamics in semiconductor quantum computer architectures: Spectral diffusion of localized electron spins in the nuclear solid-state environment. *Phys. Rev. B*, 74:035322, Jul 2006.

[Wei08] U. Weiss. *Quantum dissipative systems.* (3rd ed.), World Scientific, Singapore, 2008.

[WKvD04] F.K. Wilhelm, S. Kleff, and J. von Delft. The spin-boson model with a structured environment: a comparison of approaches. *Chem. Phys.*, 296(2-3):345 – 353, 2004.

[Woo98] W. K. Wootters. Entanglement of formation of an arbitrary state of two qubits. *Phys. Rev. Lett.*, 80:2245–2248, Mar 1998.

[WT03] H. Wang and M. Thoss. Multilayer formulation of the multiconfiguration time-dependent hartree theory. *J. Chem. Phys.*, 119(3):1289–1299, 2003.

[WT08] H. Wang and M. Thoss. From coherent motion to localization: dynamics of the spin-boson model at zero temperature. *New J. Phys.*, 10(11):115005, 2008.

[WTM00] H. Wang, M. Thoss, and W. H. Miller. Forward–backward initial value representation for the calculation of thermal rate constants for reactions in complex molecular systems. *J. Chem. Phys.*, 112(1):47–55, 2000.

[YDS05] X. Yang, T. E. Dykstra, and G. D. Scholes. Photon-echo studies of collective absorption and dynamic localization of excitation in conjugated polymers and oligomers. *Phys. Rev. B*, 71:045203, Jan 2005.

[YL07] Z.-Q. Yin and F-L. Li. Multiatom and resonant interaction scheme for quantum state transfer and logical gates between two remote cavities via an optical fiber. *Phys. Rev. A*, 75:012324, Jan 2007.

[YWSZ09] Z.-B. Yang, H.-Z. Wu, W.-J. Su, and S.-B. Zheng. Quantum phase gates for two atoms trapped in separate cavities within the null- and single-excitation subspaces. *Phys. Rev. A*, 80:012305, Jul 2009.

[YYSZ10] Z.-B. Yang, S.-Y. Ye, A. Serafini, and S.-B. Zheng. Distributed coherent manipulation of qutrits by virtual excitation processes. *J. Phys. B: At. Mol. Opt. Phys.*, 43(8):085506, 2010.

[YYX+11] W. L. Yang, Z. Q. Yin, Z. Y. Xu, M. Feng, and C. H. Oh. Quantum dynamics and quantum state transfer between separated nitrogen-vacancy centers embedded in photonic crystal cavities. *Phys. Rev. A*, 84:043849, Oct 2011.

[YYZS10] S.-Y. Ye, Z.-B. Yang, S.-B. Zheng, and A. Serafini. Coherent quantum effects through dispersive bosonic media. *Phys. Rev. A*, 82:012307, Jul 2010.

[YZ08] S.-Y. Ye and S.-B. Zheng. Scheme for reliable realization of quantum logic gates for two atoms separately trapped in two distant cavities via optical fibers. *Opt.Commun.*, 281(5):1306 – 1311, 2008.

[YZZ08] S.-Y. Ye, Z.-R. Zhong, and S.-B. Zheng. Deterministic generation of three-dimensional entanglement for two atoms separately trapped in two optical cavities. *Phys. Rev. A*, 77:014303, Jan 2008.

[ZG00] S.-B. Zheng and G.-C. Guo. Efficient scheme for two-atom entanglement and quantum information processing in cavity qed. *Phys. Rev. Lett.*, 85:2392–2395, Sep 2000.

[Zhe04] S.-B. Zheng. Unconventional geometric quantum phase gates with a cavity qed system. *Phys. Rev. A*, 70:052320, Nov 2004.

[ZKAHD07] W. Zhang, N. Konstantinidis, K. A. Al-Hassanieh, and V. V. Dobrovitski. Modelling decoherence in quantum spin systems. *J. Phys.: Condens. Matter*, 19(8):083202, 2007.

[ZR97] P. Zanardi and M. Rasetti. Noiseless quantum codes. *Phys. Rev. Lett.*, 79:3306–3309, Oct 1997.

[Zur91] W. H. Zurek. Decoherence and the transition from quantum to classical. *Phys. Today*, 44(10):36–44, 1991.

[ZZG05] X.-F. Zhou, Y.-S. Zhang, and G.-C. Guo. Nonlocal gate of quantum network via cavity quantum electrodynamics. *Phys. Rev. A*, 71:064302, Jun 2005.